UNIVERSITY OF PUERTO RICO RIO PIEDRAS CAMPUS
NATURAL SCIENCES FACULTY
DOCTORAL PROGRAM IN CHEMICAL PHYSICS

APPLICATIONS OF TWO-DIMENSIONAL TUNGSTEN DISULFIDE AND BORON NITRIDE NANOSHEETS IN SELF-POWERED PHOTODETECTORS AND MEMORY DEVICES

By

Wilber Ortiz Lago

A thesis submitted in partial fulfillment of the requirements for the Degree of

Doctor of Philosophy

San Juan, Puerto Rico

August 22, 2023

APPLICATIONS OF TWO-DIMENSIONAL TUNGSTEN DISULFIDE AND BORON NITRIDE NANOSHEETS IN SELF-POWERED PHOTODETECTORS AND MEMORY DEVICES

Accepted by the Faculty of the Doctoral Program in Chemical Physics of the University of Puerto Rico in partial fulfillment of the requirements for the degree of

Doctor of Philosophy

_____

Dr. Peter X. Feng
Professor of the Department of Physics
Thesis Adviser

_____

Dr. Antonio Martínez Collazo
Professor of the Department of Physics
Thesis Committee Member

_____

Dr. Dalice M. Piñero Cruz
Professor of the Department of Chemistry
Thesis Committee Member

August 22, 2023

Dedication

This thesis is dedicated to my mother Epifanía Lago de Ortiz, my siblings, and above all to God. They have been a source of inspiration for the successful completion of this work. My mother's good advice helped me overcome all adversities, both bad and less bad, she instilled in me my values, my principles, my faith, perseverance, and commitment, all this without asking for anything in return. I can never be thankful enough for her big dose of love. Also, I dedicate it to my father, Pascual Ortiz Cárdenas (deceased) for everything he has given me in life.

Table of Contents

List of Figures

List of Tables

Abstract

Since single-layer graphene was isolated from highly-oriented pyrolytic graphite in 2004, it led to the beginning of a new revolution in materials science due to its many applications in nano-electronic device technology. Two-dimensional (2D) materials have attracted the most attention for capacitive energy storage applications. Amongst these most interesting studies, the most predominant has been on their atomic structures, mechanical, optical, electronic, thermal, and intrinsic and extrinsic defects, which serve as the basis for a variety of promising technologies.

The recent progress in 2D materials is tungsten disulfide (WS_2) nanosheets, which are considered the most prominent member of the transition metal dichalcogenides (TMDs) family due to their outstanding optical and electronic properties in creating ultraviolet- and visible-light-sensitive photodetectors. This material exhibits a unique electronic band structure that is characterized by its broadband spectral response, excellent light absorption, sensitivity to interlayer interactions, ultra-fast bleach recovery time, and tunable bandgaps ranging from 1.3 to 2.05 eV according to the layer structure. Additionally, they also present particularly interesting properties owing to their high charge carrier mobility and high switching speed. The bulk composition of WS_2 characterized by energy-dispersive X-ray analysis showed an S/W ratio of 1.70. After mechanical exfoliation and fabrication of WS_2 thin film on SiO_2/Si substrates using the spin-coating technique, the S/W ratio was from about 1.2 to 1.34, which indicated certain deficiencies in the S atoms. This structure of the nanosheets seems to be highly

efficient in photoelectric conversion, given that they reached responsivity of 0.12 and 12.74 mA/W at 670 nm under bias voltages of 0 and 2 V, with intensities of 5.2 and 4.1 mW/cm^2, respectively. The highest detectivity was 1.17 × 10^{10} cm Hz$^{1/2}$, which is an acceptable value for low-bias photodetectors. In our study, we demonstrated that 2D WS_2 nanosheets exhibit high photon absorption in a wide range of spectra from the near-infrared (IR) to near-UV spectrum.

Instead, Two-dimensional hexagonal boron nitride nanosheets (BNNSs), one of the most widely studied 2D layered materials, have an electronic structure similar to that of graphene and are used to boost the mechanical, electrical, thermal, and optical properties of nanomaterials. The potential application of BNNSs in 2D electronics is limited because their insulating nature does not participate in charge carrier transport. In our research, carbon-doped 2D BNNS was obtained through a CO_2—pulsed laser deposition (CO_2—PLD) technique on silicon dioxide (SiO_2) and molybdenum (Mo) substrates to minimize the band gap and form a thin film with semiconductor electrical properties, thus enhancement of O_2 adsorption. The results also showed hysteresis stable over a wide range of temperatures, which makes them a promising candidate for materials based on non-volatile memory devices. Due to its functional properties and its relation to the resistive switching phenomenon, this innovative material with n-type electronic properties could improve device performance and data retention. In this sense constitutes a good alternative to design two series of Schottky barrier models with Au/BNNS/Au lateral and Au/BNNS/Mo vertical structures. Thus, the addition of carbon to BNNSs creates boron vacancies, which exhibit partially ionic character

because of the electron pairs in sp^2 hybridized B–N and weak van der Waals forces, which also helps to enhance its electrical properties at the metal- BNNS-metal interface.

Acknowledgments

First, I would like to thank my thesis adviser, Dr. Peter X. Feng, with whom I had the opportunity to share my work on many topics related to my research. He offered me an opportunity to start studies in the field of 2D materials, and with his support, I was able to successfully complete my Chemical Physics Ph.D program. I also thank Dr. Perla Enid Cruz for giving me her support during my research in mechanical exfoliation techniques. Her brilliant comments and suggestions were very useful for me to improve the synthesis methods. In the same way, I would like to express my special appreciation to my friend, Luis Bermudez, that as a PhD student in chemistry, helped me with some research equipment for a specific analysis in Dr. Nicolai's lab. His experience was crucial in improving my skills in experimental methods.

I would also like to express my deepest appreciation to Dr. Dalice M. Piñero Cruz and Dr. Antonio Martínez Collazo for being members of my committee for the thesis. I am extremely grateful for all the time and effort they have dedicated to reading this material. I hope this work helps the scientific community to pose new challenges in the future. I would also like to thank Dr. José Nieves for his recommendations on my research project and academic affairs. To Professor Lutful Bari Bhuiyan for their kind instructions in the selection process of graduate courses during the entire PhD study. To Mrs. Ileana Desiderio for always keeping me informed about course registrations and payment of assistantships.

Thanks to lab fellows, friends, and staff at the Molecular Sciences Research Center of the SEM, XRD, and AFM facilities. Thanks to the technical personnel of the Department of Physics, especially Mr. William Pérez for his innumerable services in Raman measurements.

Chapter 1

Introduction

Since single-layer graphene was isolated from highly oriented pyrolytic graphite in 2004, it led to the beginning of a new revolution in materials science due to its many applications in nano-electronic device technology [1-3]. This fact generated interest in atomically thin layered two-dimensional (2D) materials with unique physical and chemical properties [4,5]; such as molybdenum disulfide (MoS_2), tungsten disulfide (WS_2), molybdenum diselenide ($MoSe_2$), tungsten diselenide (WSe_2), molybdenum ditelluride ($MoTe_2$), silicon carbide (SiC), hexagonal boron nitride nanosheets (h-BNNSs), etc. Among these most interesting studies, the most predominant has been on their atomic structures, mechanical, electronic, thermal properties, and intrinsic and extrinsic defects [6], which serve as the basis for a variety of promising technologies. The recent progress in 2D materials beyond graphene is 2D WS_2 nanosheets, which are considered the most prominent member of the 2D transition metal dichalcogenides (TMDs) family [7] due to their excellent optical and electronic properties in creating sensitive photodetectors in the ultraviolet, visible, and infrared regions. Instead, BNNSs are one of the most widely studied 2D layered materials with an electronic structure similar to graphene, excellent thermal conductivity, and prominent UV absorption characteristics [8]. These materials are being extensively studied due to their excellent applications in next-generation electronics and optoelectronics devices. According to their chemical compositions and structural configurations, 2D materials are categorized as semiconducting, insulating, metallic, semi-

metallic, and superconducting. However, many 2D are natural semiconductors that possess huge potential than silicon-based devices.

For another hand, van der Waals gaps between neighboring layers and large specific surface areas in the form of sheets of 2Ds have attracted the most attention for capacitive energy storage applications [9,10], which can respond to energy and environmental concerns soon. In addition, these materials have exceptional importance to enhance the electrochemical properties and become a promising candidates for electrode material in supercapacitor devices [11]. Some studies also show that 2D materials often exhibit hysteresis in their electrical measurements when the measured current is in a voltage sweep direction with the form of a loop or hysteresis curve due to charge trapping [12], which makes them a promising candidate for materials based on non-volatile memory devices.

This chapter will briefly introduce the perspectives on photodetectors, their recent advances, and some fundamental limitations which constrain their use in certain applications that require better photodiode response. Then, the electrical and optical properties of 2D materials will be discussed given their potential application in self-powered photodetectors, especially in transition metal dichalcogenides (TMDs) as an attractive option of materials that reveal a wide range of bandgap covering all visible spectrum than standard photodetectors. On the other hand, crystal lattice structures, components, and interlayer bonding properties of 2D hexagonal boron nitride nanosheets (BNNSs) will be described. Similarly, Carbon-doped BNNSs will be studied to investigate the electrical and optical properties of stacked layers. These changes will also provide high thermal

conductivity, stability over a wide temperature range, and excellent photoelectric performance in the high penetration rate ultraviolet (UV) spectral range. In addition, various semiconductor systems will be explored as photosensitive materials in photodetectors capability, each with certain advantages and disadvantages to enhance photodetection, stability, and performance. Finally, a general study of the energy band diagrams of Schottky diodes will be made.

1.1 State-of-the-art photodetectors for electrical and optoelectronic devices

Silicon photodetectors, with their indirect bandgap of 1.1 eV are utilized in such diverse applications as optical position sensors, beam alignment, medical imaging, optical communication, etc. There are two broad technologies based on silicon diodes, one on charge-coupled devices (CCD) and the other on complementary metal-oxide-semiconductor (CMOS) [13-15], which have dominated the market for decades. If applications in high-quality imaging are involved in which both high frame rates and high resolution are required, CMOS sensors are the first option due to that their millions of pixels achieve high image quality and provide very satisfactory results over CCDs in terms of speed and less power consumption [16,17]. Although CMS sensors have certain advantages over CCD sensors, there are some special applications for which CCDs continue to be highly valued in the technology industry, such as fluorescence microscopy, high-resolution microscopy, and medical applications due to their low fixed pattern noise. However, CMOS and CCD devices require an elevated design complexity, higher cost of production, and multi-tap technologies to achieve higher performance sensors.

On the one hand, silicon photodiodes have some fundamental limitations which constrain their use in certain applications that require better device response to light. For instance, CMOS sensors are subject to certain deficiencies by the time-varying circuit models and temporal noise sets that affect device performance, which become increasingly pronounced as CMOS technology scales [18]. Silicon photodiodes also exhibit a limited response time and require a constant temperature to maintain their performance. Similarly, photomultiplier tubes are incompatible with polymers and metals [19], further limiting their applications in medical equipment, analytical instruments, and industrial measurement technologies.

Technological advances are on the threshold of a fascinating new era, the era of flexible and wearable electronic devices [20-22]. Optoelectronics systems that can be bent, wrapped, and stretched have attracted interest in flexible smart system applications like mobile, smartwatches, light-emitting diodes, sensors, field-effect transistors, energy storage, etc. Despite the high technological level of silicon, its applications in flexible and transparent optoelectronics are limited due to its indirect bandgap, which results in mediocre optical absorption and rather poor optical emission. Silicon photodetector active region has a large thickness in the order of microns to detect light efficiently, allowing some carriers to be absorbed deep and there are slowly diffused due to the low intensity of the electric field, making silicon detectors opaque and incompatible with flexible substrates. However, 2D materials can be deposited onto solid and flexible substrates to

achieve high-quality thin films, as the performance of samples largely depends on their stacked layer numbers, grain size, orientation, and morphology, respectively.

1.2 Electrical and optical properties in 2D

2D materials beyond graphene have triggered a new field of research as an attractive option of materials due to their excellent electrical and optical properties, namely transition metal dichalcogenides (TMDs) and BNNSs hold a special place for applications in optoelectronic devices. These van der Waals heterostructures have been developing extremely fast in the development of novel devices, such as tunneling transistors, resonant tunneling diodes, photodetectors, memory devices, etc.

1.2.1 2D TMD-based devices

TMDs are a family of two-dimensional layered materials(2DLMs) that forms compounds of the types MX_2, where M is a transition metal (Mo, W, Re) and X is a chalcogen (S, Se, Te). TMDs are promising for electronic and optoelectronic devices because of their semiconductor properties as opposed to semi-metallic graphene and better thermal stability than two-dimensional allotrope materials such as black phosphorus and silicene [23-25]. Due to their unique physical properties, TMDs can open the doors to a large number of devices and applications, unlike conventional semiconductors such as silicon (Si), germanium (Ge), or III-V [26, 27]. Moreover, flexible and transparent electronics are two such examples, which can also allow the integration of entirely new types of electronic components that can be compatible with all existing electronic chips, and with the

limitations of silicon chips. While the field is still in its infant, it has already shown very promising results in broader aspects such as integration techniques, compatibility, and high performance on large-area flexible substrates [28]. TMD-based devices are promising candidates for next-generation photodetectors, as they are at the heart of the multitude of technologies that affect our daily lives. Its photodetection mechanisms, sensitivity, and performance allow us to understand the advantages of these devices in the face of the growing application demands across various branches of science.

TMDs have sizeable bandgaps ranging from 1 to 2.5 eV, corresponding to ultraviolet (UV), visible, and infrared spectra (IR) ranges, which are optimal for optoelectronic and light-emitting devices, respectively. The band gap value decreases with the increasing size of the chalcogen atom and is less sensitive to the size of the transition metal [29]. For example, the band structure of bulk WS_2 has an indirect bandgap in the range 1.3 eV < ΔEg < 1.4 eV, and it increases as the number of stacked layers decreases until reaching a value of 2.05 eV, corresponding to the total density of states for the WS_2 monolayer [30,31]. Similarly, typical values of the optical band gaps of some TMDs are 1.9 eV for MoS_2, 1.65 eV for $MoSe_2$, and 1.7 eV for WSe_2, indicating that WS_2 is among the most attractive 2D layered materials due to its higher broadband. The origin of these transitions is attributed predominantly to the interlayer coupling effect or quantum confinement, where the photoluminescence energy of excitons shows the evolution of the electronic structure as a function of the number of layers. In addition, the difference of energy between the valence band maximum (VBM) and

conduction band minimum (CBM) is located at the K point of the hexagonal Brillouin zone (BZ) and is mostly due to the localized d-orbitals of the transition metal atom [32-34]. Another significant feature of these band structures is optical transitions between the density of states (DOS) peaks and is treated as the transition from an indirect-to-direct bandgap in the UV, visible, and IR spectra.

1.2.2 2D tungsten disulfide (WS_2) nanosheets

Tungsten disulfide is an inorganic chemical compound with a layer structure of tungsten and sulfur atoms with the chemical formula WS_2, which occurs naturally as the rare mineral called tungstenite. This compound is part of the family of materials called the transition metal dichalcogenides. WS_2 has a two-dimensional structure with tungsten atoms positioned between two layers of sulfur atoms appearing in trigonal prismatic coordination sphere-forming hexagonal crystals, where atoms within each layer are connected through an ionic bond with a contribution of covalent interaction, that provide stability in the three-layer stack, as shown in Figure 1.1 (a). Similarly, the single-layer or sheet projection of WS_2 (monolayer) onto the plane exhibits hexagonal structures (Figure 1.1(b)). In contrast, the multiple planes formed by the stacks are held together by weak van der Waals interactions. For example, the WS_2 bilayer possesses a sandwich-like structure when two monolayers interact with each other, as shown in Figure 1.1(c).

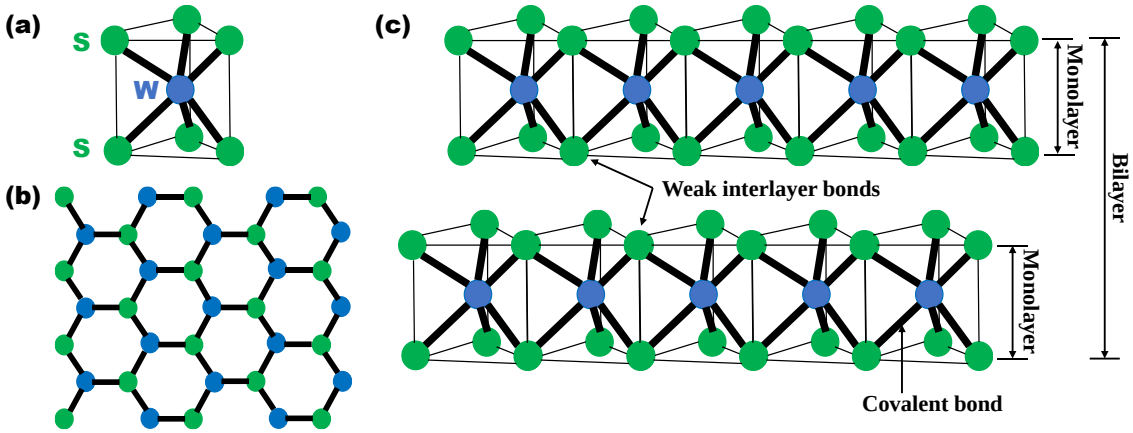

Figure 1. 1 Crystal structure of WS_2 with **(a)** tungsten atoms positioned between two layers of sulfur atoms, **(b)** single-layer projection of WS_2 onto the plane, and **(c)** WS_2 bilayer structure.

The electronic structure of TMDs depends on the filling of the d-orbitals in the transition metal and the coordination environment [35]. For example, three possible stacking forms of WS_2 are characterized by the 1T, 2H, and 3R structures, as shown in Figure 1.2(a). The 1T structure adopts a tetragonal symmetry (the D_{3d} group) and octahedral coordination of the W atoms, while one of the sulfur layers is shifted compared to the others. Instead, the 2H phase (or 1H in the case of a single layer) shows a hexagonal close packing (the D_{3h} group) with coordination of triangular prisms of the W atoms, where the sulfur atoms are vertically aligned along the z-axis. The 3R structure exhibits a rhombohedral symmetry [36, 37]. On the other hand, the octahedral coordination of WS_2 results in two energy levels represented by degenerate d-orbitals, d_{z^2},$_{x^2}$,$_{y^2}$, and d_{xy}, $_{xz}$, $_{yz}$. Since the p orbitals of chalcogens are located at lower energy than the Fermi level, it means that only the filling of the d orbitals determines the type of structure in MX_2 compounds. For the single-layer phases in the 2H and 3R structures, the d-orbitals split into three

energy levels d_{z^2}, $d_{x^2-y^2, xy}$ and $d_{xz, yz}$ with an energy gap of E_g between the d_{z^2} and $d_{x^2-y^2, xy}$ orbitals, as shown in Figure 1.2(b).

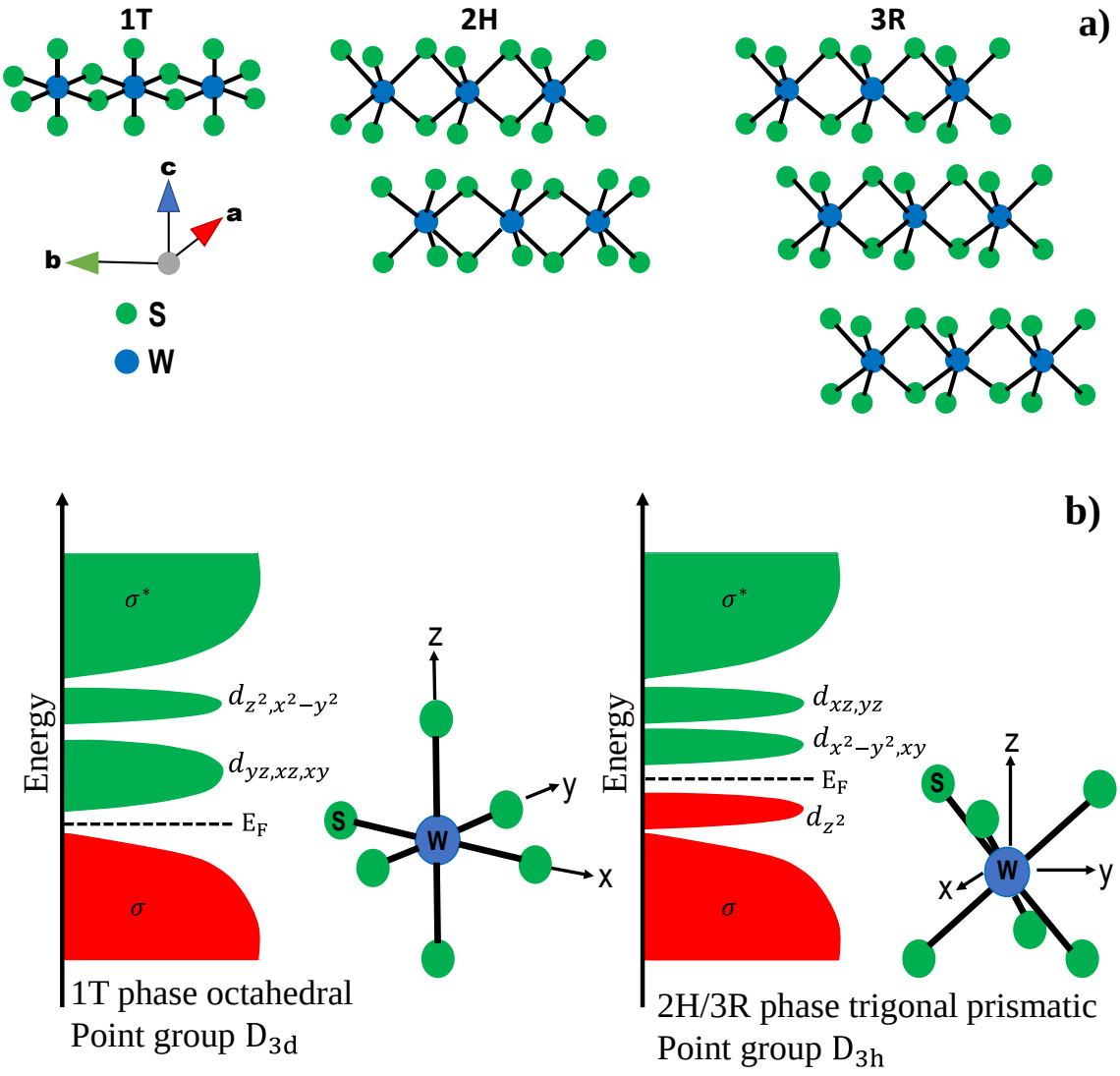

Figure 1. 2 (a) Crystal structure of WS_2: Octahedral (1T), Trigonal prismatic (2H), and Trigonal prismatic (3R) unit cell structures. **(b)** Energy levels: Phase octahedral and phase trigonal prismatic.

The 2H-WS_2 monolayer is a semiconductor in group 6 TMDs with a direct band gap of about 2.05 eV, whereas the distorted 1T-WS_2 possesses a metallic

character. The difference between these two structures was also observed by G. Ozin et al. [38] by measuring the optical properties of the exfoliated samples. According to their analysis, the 1T-WS_2 sample showed a gray color, while the 2H-WS_2 sample was brown-yellow. These changes also demonstrated the 1T-WS_2 dispersion efficiently absorbed light in the full spectral range (350−1200 nm), with a decrease of the absorbance with increasing wavelength. Instead, the 2H-WS_2 dispersion exhibited a strong increase in absorption at lower wavelengths.

In our study, we present the 2D WS_2 nanosheets which is a 2H-WS_2 structure of semiconducting behavior with excitonic features, corresponding to direct gap transitions A (1.95 eV) and B (2.35 eV) [39]. Figure 1.3(b) shows a single-particle energy diagram of the conduction and valence bands, with valley-specific optical selection rules in monolayer WS_2 at the K and K' points of the Brillouin zone (Figure 1.3(a)). The spin-orbit coupling (SOC) effect of the valence band splits the spin-up and spin-down components (by Δ_v ~ 400 meV), giving rise to two spectrally well-separated characteristic optical transitions, involving the upper (A) and lower (B) excitons. The circularly polarized (σ+) light couples to both the A and B transition in the K valley, while opposites circularly polarized (σ-) light couples to the exciton transitions in the K' valley [40].

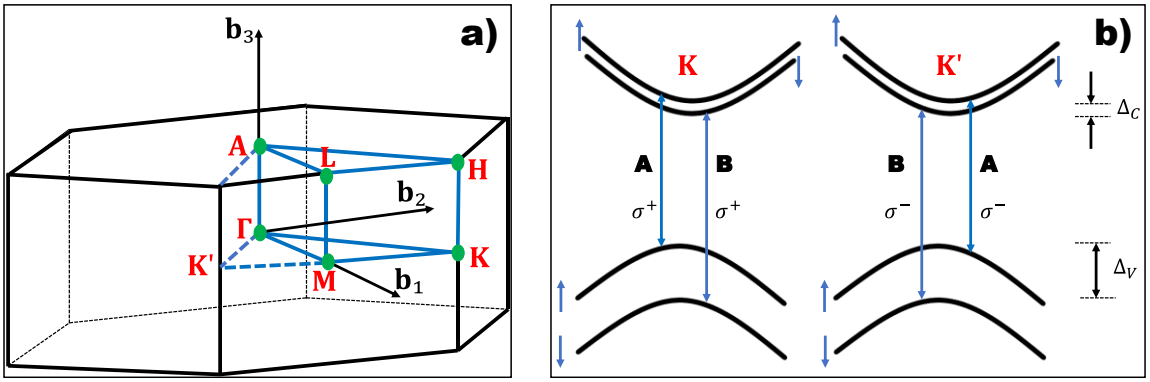

Figure 1. 3 Brillouin zone of 2H- WS_2 **(a)** in the conduction and valence bands and **(b)** valley-specific optical selection rules at the K and K' points.

1.2.3 2D WS_2 nanosheet-based devices

Therefore, Among the group of TMDs, 2D WS_2 nanosheets exhibit a unique electronic band structure that is characterized by its broadband spectral response, excellent light absorption, sensitivity to interlayer interactions, ultra-fast bleach recovery time, and tunable bandgaps ranging from 1.3 to 2.05 eV according to the layer structure [41,42]. This makes it a very promising semiconductor material for applications in catalysts, lasers, batteries, photodetectors, and lubricants. 2D WS_2 nanosheets could be a promising candidate in new generation solar cells [43,44], gas sensors [45,46], photoluminescence [47,48], collision detectors, biomedical imaging, humidity sensor [49], optically filtered detectors [50], etc. Additionally, they present particularly interesting structures, owing to their high charge carrier mobility, high switching speed, and optical properties. Y.H. Tsang et al. [51] confirmed that WS_2 thin sheets contributed to a remarkably enhanced nonlinear optical absorption performance at 532 nm and 1064 nm. In our study, we will

demonstrate that 2D WS_2 nanosheets exhibit high photon absorption in a wide range of spectra from the near-infrared (IR) to near UV spectrum.

1.3 2D hexagonal boron nitride nanosheets (BNNSs)

BNNSs are hexagonal structures composed of boron (B) and nitrogen (N) atoms, which construct a characteristic honeycomb crystal lattice structure based on six-membered B_3-N_3 hexagons (Figure 1.4(a)). Like the 2D WS_2 nanosheets, the stacked layers are held together by weak Van der Waals forces, while the B and N atoms are bound by covalent bonds. The inter-planar spacing between two parallel layers of h-BN is 0.332 nm and the bond length between B and N atoms is 0.144 nm, as shown in Figure 1.4(b). These values are very similar to the interplanar separation and the bond length of graphene (0.333 nm and 0.142 nm). However, graphene holds nonpolar homo-nuclear C-C intra-layer bonds, while BNNS presents highly polar B-N covalent bonds resulting in different optimal stacking modes suggesting large differences in the dispersive component of the interlayer bonding [52,53]. Despite these differences, the binding energy curves of both materials are very similar.

The interactions between single layers of BNNSs are often well characterized. These are determined by the balance between the London dispersion force, electrostatic interactions, and Pauli repulsions. Thus, understanding the relative contribution of interactions of interlayer bonding is essential for the effects of functionalization on the physical, mechanical, electronic, and electromechanical properties, as well as for the design of new materials.

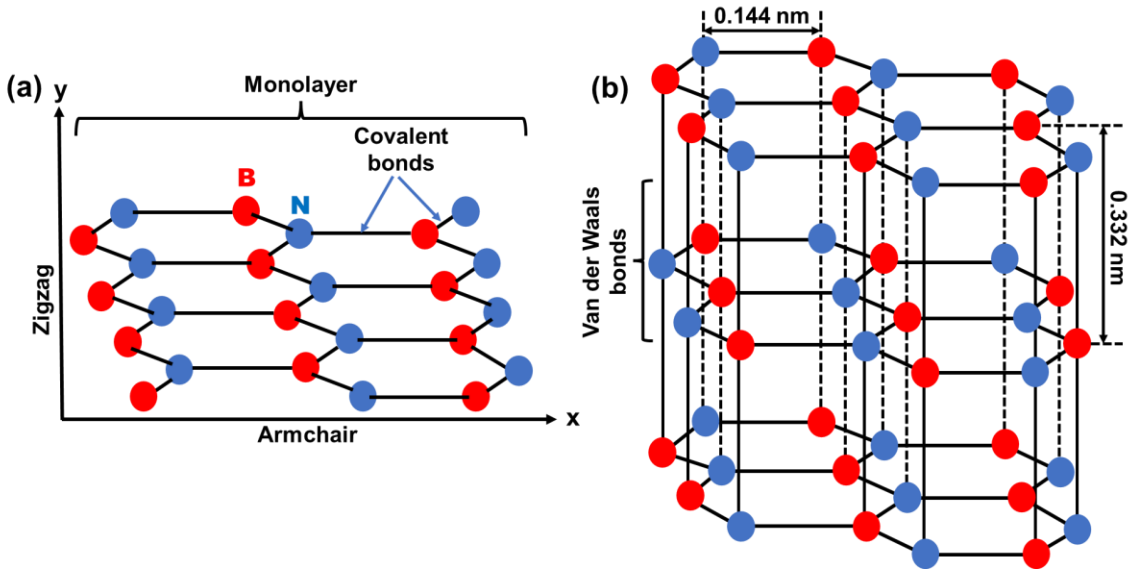

Figure 1. 4 Structural models of **(a)** monolayer h-BN or BNNS and **(b)** few-layer h-BN or BNNSs.

The ionic nature of the B-N bond also affects the stacking pattern of adjacent h-BNs. Layer-layer interactions are exerted by pseudo-delocalized out-of-plane π orbitals and weak Van der Waals forces, as previously described. This structure exhibits extremely high chemical stability and resistance to oxidation in the range of 400-870 °C, where monolayer h-BN starts to oxidize at 700 °C and can sustain up to a temperature of about 850 °C, making it very attractive for a range of practical applications in the bulk phase, which chemical stability and effective structural integrity are required. Therefore, it is interesting to carry out chemical reactions involving other atoms in the bulk h-BN lattice while retaining the intrinsic properties of the sample. With the recent progress in the field of 2D nanosheets, It is necessary to propose alternative chemical strategies to integrate and use BNNS as a type of semiconductor material to expand its applications.

1.3.1 Carbon-doped 2D hexagonal boron nitride nanosheets

BNNNSs exhibit a unique combination of wide bandgap semiconductors and layered crystal structures. However, these electronic properties have some limitations for applications in optoelectronic and electronic devices. For example, to make partial diodes or transistors, the BNNS layer needs to be doped by implanting impurities into the electronic structure. This process changes the energy levels and conductivity of the material, producing n-type and p-type semiconductors, respectively.

There are several alternative doping methods for wide-band-gap materials, such as diffusion doping; ion implantation; in-situ doping, etc. But the plasma ion implantation technique seems to be the most effective to introduce impurities into the BNNSs as it allows for optimal precision and control, helping to lead to the formation of different layered structures, improving the electrical, optical, and semiconductor properties of the material.

In particular, BNNSs exhibit typical characteristics of p-type semiconductors when doped with beryllium and n-type with sulfur, boron, silicon, or co-doped with nitrogen and carbon [54]. Of all these possibilities, it is reported that partial substitution of C atoms with B and N atoms could lead to the formation of their alloys (B_x-C_y-N_z) with well-defined layer structures. Theoretical calculations have also shown that B_x-C_y-N_z structures are semiconducting, with band gaps ranging from 0.02 to 2.00 eV [55] and depend on the composition and electronic arrangement of B, C, and N elements in the 2D layer lattice. T. Shimada et al. [56]

also indicated that a direct sp^3 covalent chemical bond was formed when C replaced adjacent B and N in different layers, which resulted in narrower band gaps (e.g., 0.37 eV). Thus, B_x-C_y-N_z hexagonal sheets seem to be the new generation of promising materials for the manufacture of nanoscale electronic devices. All this progress has stimulated our curiosity to investigate the electrical and optical properties of stacked layers of carbon-doped BNNSs.

Carbon doping in BNNS lattices can construe several possible structures with a direct band gap at the Γ point, which could open a wide range of advantages for optical applications due to their high sensitivity when compared with bulk silicon [57]. Figure 1.5 (a) shows the single-layer structure of BNNSs doped with carbon elements, while Figure 1.5 (b) shows several possible hybridized nanostructures BNNSs formed from some doping carbon atoms. For example, the structure of B_3N_3 can be hybridized in several possible ways, such as B_2-C_2-N_2, B_1-C_3-N_2, B_2-C_3-N_1, B_3-C_1-N_2, etc. [58]. These resulting layers lead to a larger overlap in forming bonds, which offers the greatest opportunity to fabricate more hybridized materials via controllable heteroatom doping.

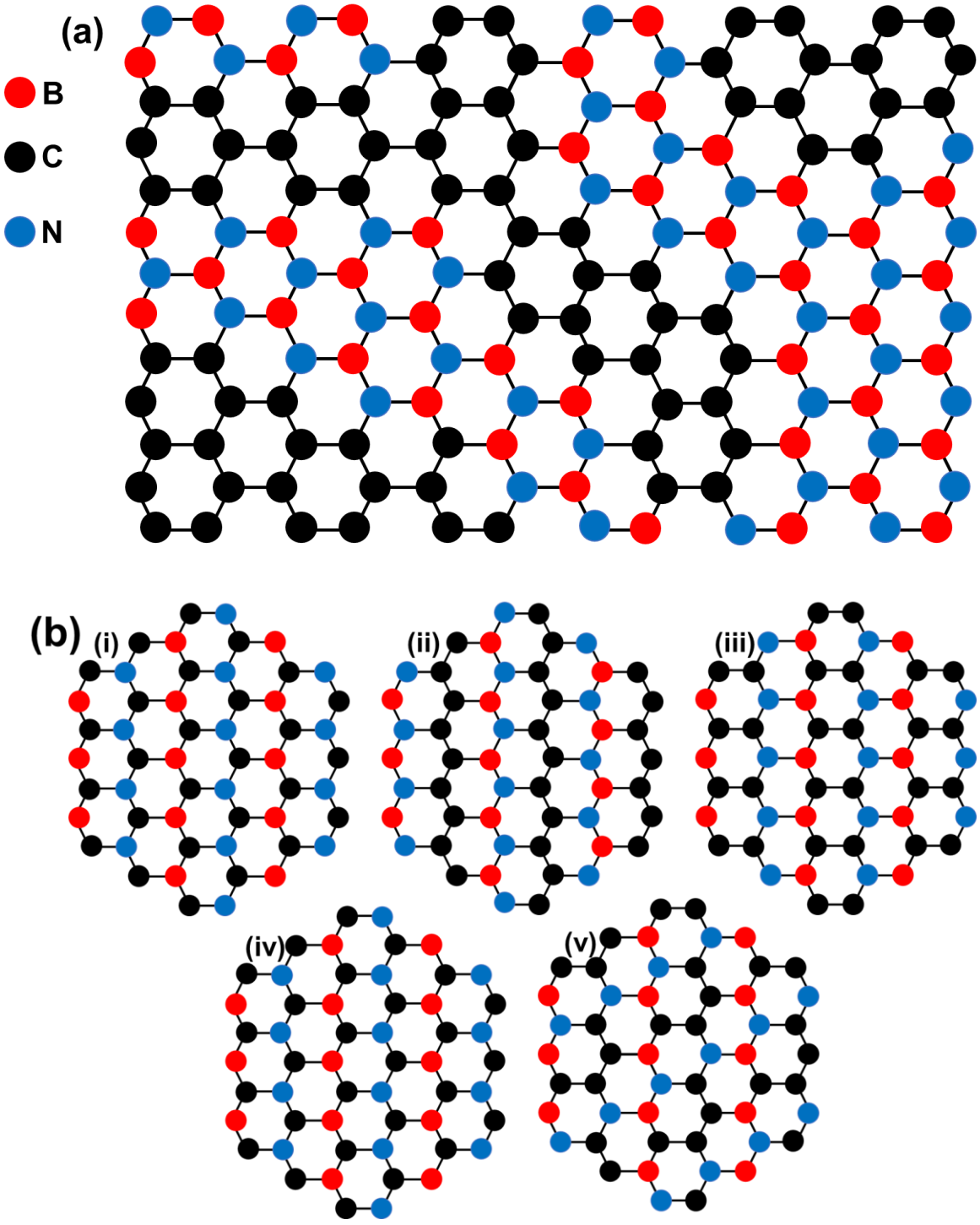

Figure 1. 5 (a) Schematic diagram of doped single-layer BNNS and **(b)** hybridized BNNSs structures with carbon atoms.

1.3.2 2D BNNS-based devices

BNNSs, as a unique class of 2D nanomaterials, consist of one to few atomic layers of the hexagonal boron nitride (h-BN), which hold a special place due to its excellent thermal, chemical, and mechanical stability similar to graphene. Likewise, this material has low compressibility, high thermal conductivity, insulation properties, and a wide bandgap in the range of 4-6 eV. Making it a promising candidate for many groundbreaking applications, such as optoelectronics, spintronics, chemical sensors, catalysis, energy storage, etc. BNNSs also have stronger resistance to oxidation than graphene [59], making them more suitable for applications at high temperatures, especially in miniaturized modern devices with electrical insulation. In addition to their chemical and crystalline qualities, these nanosheets exhibit a free exciton lifetime of 0.43 ns, confirming their interesting optical properties. BNNSs do not luminesce in the emission spectral range of TMDs in the near-infrared of the electromagnetic spectrum when some form of energy is supplied but show an ultraviolet luminescence band at 215 nm, which opens a new science research field for future applications in deep-UV light emitting and laser devices [60,61]. Although known for its structural similarities to graphene and other 2D materials, the potential applications of BNNSs in 2D electronics are limited because their insulating nature does not participate in charge carrier transport. By doping with enough carbon (C), the band gap is minimized, and a set of discrete energy levels with semiconductor electrical properties are formed of high spin density and charge density [62], resulting in the enhancement of O_2 adsorption. This allows the material to have enormous

potential for various applications, such as flexible electronics [63, 64], Junction Field Effect Transistor (JFET) [65,66], dielectric coating with excellent heat dissipation properties [67], etc. C. Zhao et al. [68] showed that carbon-doped BNNSs exhibited ferromagnetic hysteresis stable at room temperature and above, while they disappeared with the removal of carbon atoms from the BNNSs lattice. This suggests that the observed magnetism originated from carbon-doping rather than from extrinsic magnetic impurities, thus becoming a promising candidate for applications in materials based on non-volatile memory devices.

1.4 What are we trying to achieve?

In recent years, 2D layer materials have emerged as potential candidates for next-generation devices due to their intriguing mechanical strength, optical, flexibility, rigidity, and enhanced electrical. Within this family of materials, 2D WS_2 and BNNS nanosheets have attracted huge interest in scientific, medical, and industrial applications for their unique physical and chemical properties. Since they have semiconductor behaviors that include layered structures, layer-dependent optical bandgaps, and high-surface-area, it has given rise to the need to design a prototype with a metal-semiconductor-metal structure, capable of detecting light across a wider range of the visible spectrum than traditional light photodetectors. Thus, we believe that our back-to-back Schottky diode-based prototype is simple and low-cost to contribute to the needs of various applications, such as imaging, memory devices, environmental research, optical communication, chemical analysis, flexible electronics, health infrastructure, etc. This means that the device must have high sensitivity, higher stability, fast response time, and self-powering

properties; that is, operate in photovoltaic mode (zero bias) from the near-infrared (IR) to near UV spectrum. According to these considerations, the experimental results show the feasibility and effectiveness of fabricating a photodetector with 2D WS_2 nanosheets, with nonlinear current–voltage characteristics, and a simple architecture than heterostructure-based photodiodes. Instead, BNNSs exhibit stable hysteresis characteristics over a wide range of temperatures, which makes them a promising candidate for materials based on non-volatile memory devices. Its electronic properties also have special features that can enhance the device's performance and data retention due to its functional properties, thermal-mechanical stability, and its relation with resistive switching phenomena. Therefore, our work provides a facile route to develop self-powered photodetectors and memory devices with extremely low power consumption, opening up opportunities for future large-scale applications.

1.5 Main prototypes of photodetectors

Figure 1.6 illustrates the possible designs of the prototypes under which the photodetectors may operate over a wide range of illumination. The vast majority of PDs are composed of semiconductor materials that follow one of four fabrication mechanisms: photoconductors, metal-semiconductor-metal (MSM), Schottky barrier, and p-i-n photodiodes. Schematics of these prototypes, using 2D active semiconductors, provide the main forms to design detector and nonlinear current–vo devices, such as Schottky contact optical systems with different-barrier heights, non-rectifying electrical junctions, or a combination of these mechanisms.

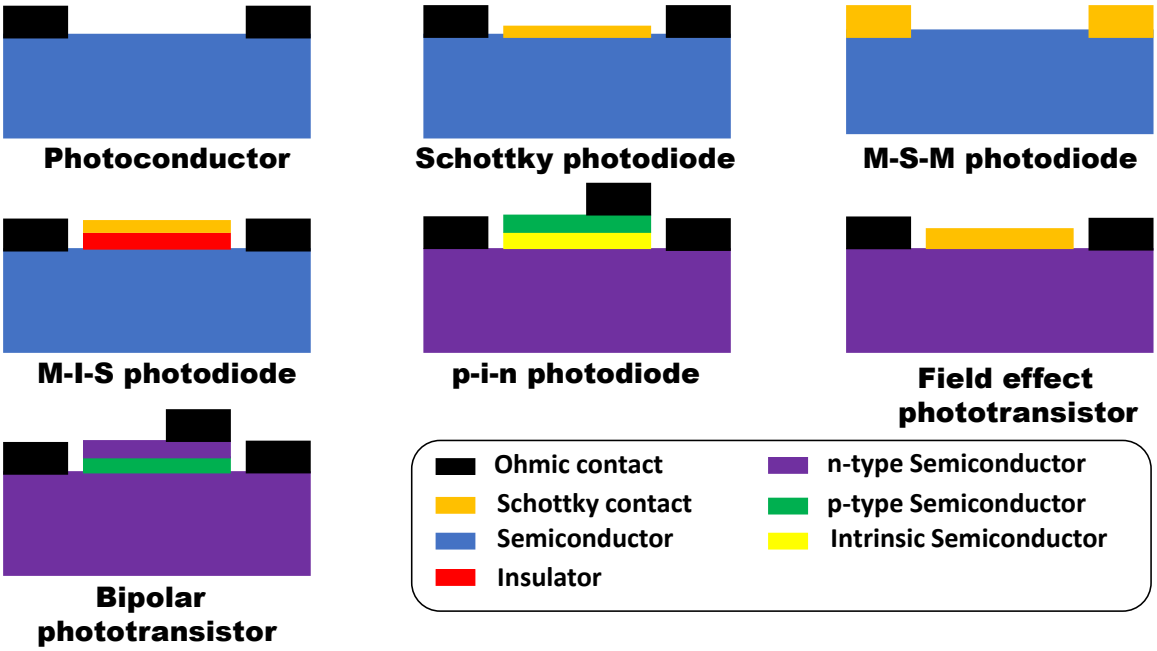

Figure 1. 6 Schematic of different prototypes applied to photodetectors.

1.5.1 Photoconductors

A photoconductor normally consists of a semiconductor active layer with two ohmic electrodes serially connected to resistance and an external bias voltage. When incident photons strike the active material that is present as a thin film, it changes the conductance of the semiconductor proportionally to the intensity of incident radiation. The main contributor to the conduction mechanism under illumination is the majority charge carrier that carries most of the electric charge in the semiconductor and they easily flow across the ohmic contacts [69]. Since the current depends in large quantity on majorities carriers, minority carriers accumulate at one of the ohmic contacts, causing additional majority carrier injection through minority carrier recombination. This effect induces again to large photoconductivity compared to other prototypes, which depends in particular on

the ratio between concentration (minority carrier lifetime) and majority carrier transit time [70]. The main disadvantage of photocurrent is the slow response time due to long carrier lifetimes before recombination and the relatively high dark current level. Therefore, photoconductors can be used for a variety of applications where response speed and dark current are not particularly important.

1.5.2 Schottky barrier photodiodes

Schottky barrier photodetectors consist of a thin metal layer deposited on the surface of a semiconductor which is in between two ohmic contacts. The metal film is thin enough to allow a large fraction of the incident radiation to be absorbed in the metal-semiconductor (M–S) junction, where photogenerated electron-hole pairs are collected near the depletion region formed at the Schottky junction. This leads to the generation of photovoltage across the two contacts which gives the device acceptable responsivity and stability since the active region in photodetection is shielded from all surface contaminants, as well as high photon absorption in a wide range of spectra of the conducting layer.

1.5.3 MSM Diodes

MSM diode-based photodetectors are two back-to-back Schottky barriers with M-S and S-M contact interfaces, respectively. The active semiconductor sandwiched between two metallic electrodes requires sufficient external bias to become fully depleted; however, this largely depends on the amountltage of impurities added to the semiconductor. In addition, according to the technique used in the fabrication of MSM photodetectors, the performance of the devices can vary.

Since the model of an MSM prototype consists of alternating metal layers deposited on the semiconductor active layer, its structure represents a very simple photodetector design, which has a high bandwidth capability and suitability for integration with field effect when compared to other architectures. Their main limitation includes a relatively large dark current when a bias voltage is required, but many of these models act as self-powered photodetectors.

1.5.4 p-i-n photodiodes

The most common photodetector is the p-i-n photodiode. This device is based on the p-i and n-i junctions with a region of highly doped atoms. The p-type side is connected to the negative terminal and the n-type side is connected to the positive terminal of the battery. The width of the space charge region (SCR) is more in the intrinsic region, and it is narrow in the n-type zone. The increase in the thickness of the depletion region allows an increase in the surface area on which light falls, which produces more electron-hole pairs because it contains a low number of charge carriers. Due to this, the conversion efficiency of a photodiode increases at the reverse bias, thus generating a large photocurrent. However, capacitance is inversely proportional to the width of the SCR, making the p-i-n diodes decrease their junction capability if the diode is forward biased since the depletion width gets thinner, resulting in an absorption adversely affecting the high performance of the photodetector. The major advantages of this p-i-n photodiode are the high response speed, high signal stability, and low noise-to-signal ratios. Nevertheless, one of the main disadvantages is that a small quantity of dopant atoms in the conducting regions can reduce resistance and produce a quite thin

depletion region. Thus, the prototype design will define the light-sensing mechanism in the visible spectrum.

1.5.5 Schottky mechanism

1.5.5.1 Schottky diode

A Schottky barrier is a potential energy barrier for electrons formed between a metal and a semiconductor. These junctions have rectifying characteristics, suitable for use as a semiconductor diode. It is characterized by low forward voltage drop and a very fast switching speed than PN junction diodes, and low-loss energy under high-frequency operating conditions. It is particularly useful in the electronics industry as it has many applications such as diode rectifiers, switching regulators, voltage clamping, discharge protection, charge control, radio frequency (RF), etc. It is also used as Schottky TTL in digital computers because these devices require fast switching diodes to improve the performance of their electrical components.

The Schottky diode, also known as a Schottky barrier diode, uses conductive materials instead of P-type semiconductors, thus forming a metal-semiconductor junction, as shown in Figure 1.7(a). The metal side acts as the anode while the n-type semiconductor acts as the cathode, which allows the charge to flow from the metal side to the semiconductor side, but not in the other direction due to the large Schottky-barrier height. A simple way to represent a Schottky diode is through a triangle adjoining by adding two additional legs on a line passing across one vertex, as shown in Figure 1.7(b).

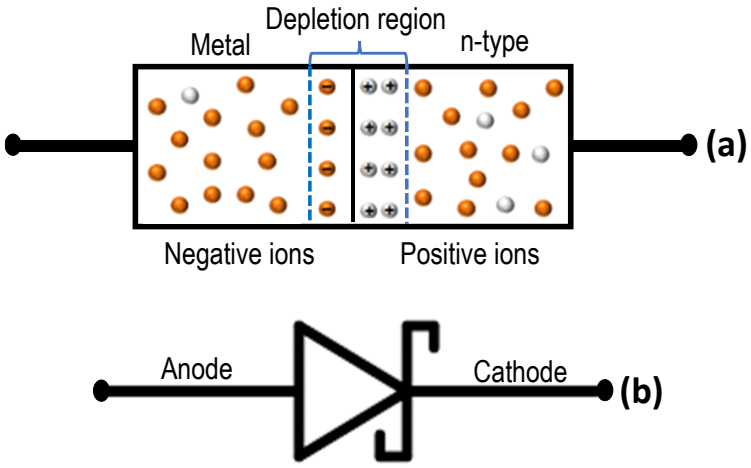

Figure 1.7 a) Schottky diode formed by the junction of a metal with a semiconductor and **b)** schematic symbol.

1.5.5.2 Energy band diagram of Schottky barrier

To construct the band diagrams, first, let us consider the metal and semiconductor energy band diagram separately, as shown in Figure 1.8(a). Where Φ_m is the work function of the metal; Φ_s is the work function of the semiconductor; χ is the electron affinity of the semiconductor ($q\chi_s$); E_{Fm} is the Fermi level of the metal; E_F is the Fermi level of the semiconductor; E_V is the valence band edge; E_c is the conduction band edge; and E_g is the energy gap (the top and bottom of valence and conduction bands). The Fermi level of the n-type semiconductor is higher than the metal because there are sufficiently electrons that can occupy higher energy levels, allowing the work function of the semiconductor to always be lower than the metals. When the metal-semiconductor junction is formed, the energy levels above the Fermi level tend to be empty of electrons while below they tend to be a cull. Consequently, electrons can flow from the semiconductor into the

metal, allowing the higher Fermi level to be lowered and the lower Fermi level to rise. Generating positive charges on one side of the semiconductor, negative charges on the metal side; and a contact potential, as shown in Figure 1.8(b). When the transfer is complete, the Fermi energies are lined up at equilibrium, leading to the formation of band diagrams, and the barrier height in the interface states. These junctions contribute to the formation of the Schottky barrier height (Φ_B), the built-in-voltage barrier (V_i), and the thickness of the depletion region (W_0), which depends on the concentration of ionized acceptor atoms.

Since the contacts are metal-semiconductor, the built-in voltage barrier in the Schottky junction is represented by the difference in work function

$$qV_i = \Phi_m - \Phi_s = \Phi_B - (E_c - E_F) \tag{1.1}$$

$$\Phi_B = \Phi_m - q\chi_s \tag{1.2}$$

If the semiconductor is n-type, the built-in-voltage barrier is also expressed by

$$V_i = \frac{\Phi_B}{q} - \frac{k_B T}{q} \ln\left(\frac{N_c}{N_D}\right) \tag{1.3}$$

where q is the elementary charge, k_B is the Boltzmann constant, T is the absolute temperature, N_C is the effective state density in the conduction band that is constant for a given temperature, and N_D is the donor doping level. If we use moderate to lower doped semiconductors, we can reduce the Schottky barrier even further.

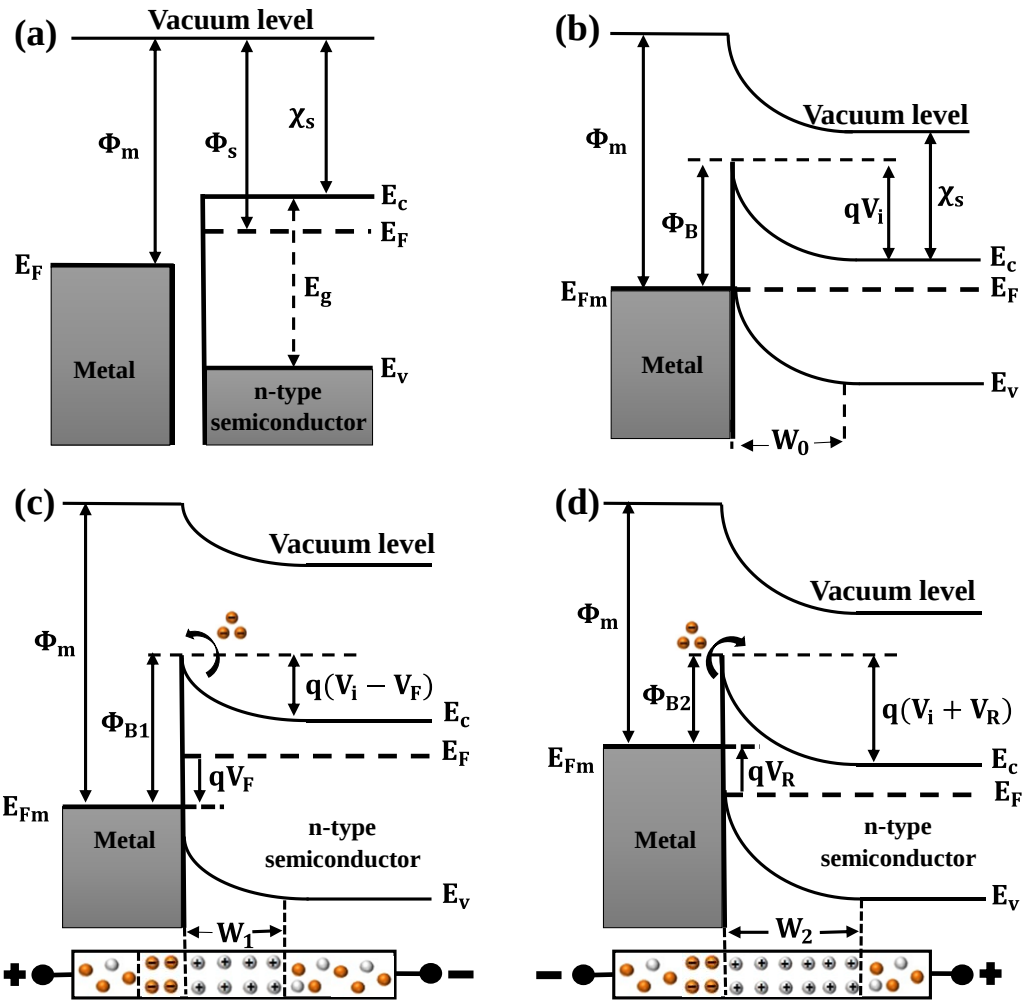

Figure 1. 8 Energy band diagrams of Schottky barrier **(a)** before contact, **(b)** after contact, **(c)** forward bias, **(d)** and reverse bias.

When an external voltage is applied under forward bias in the terminals of the metal-semiconductor junction, equilibrium between diffusion and drift is disturbed. Electrons tend to move toward a positive bias because the voltage drop from V_i to $V_i - V_F$ on semiconductor induces a narrow depletion region W_1, resulting the Fermi energy of the metal to be reduced with respect to the semiconductor, as shown in Figure 1.8(c). Conversely, under reverse bias, the voltage drops increases from V_i to $V_i + V_R$, which in turn causes a wide depletion region, as

shown in Figure 1.8(d). This behavior of the Schottky diodes is directly related to the concentration of dopants in the semiconductor material since a large amount of carriers are generated in the depletion region. The current in a Schottky diode under forward is described by the equations (1.4) and (1.5).

$$I = I_s \left[exp\left(\frac{qV_D}{\eta k_B T}\right) - 1 \right], \tag{1.4}$$

where I_s is the saturation current ($I_s \approx 10^{-12}$ to 10^{-6} A), q is the elementary charge ($q = 1.602\text{x}10^{-19}$ C), η is the ideality factor (η typically varies from 1 to 2), k is the Boltzmann constant ($k_B = 1.38\text{x}10^{-23}$ $m^2Kgs^{-2}K^{-1}$), T is the absolute temperature, and V_D is the voltage drop across the Schottky diode. I_s is given by

$$I_s = AA^*T^2 exp\left(-\frac{\Phi_B}{k_B T}\right), \tag{1.5}$$

where A is the active Schottky diode area and A^* is the Richardson constant (depends on the semiconductor material). The barrier height is also given by

$$\Phi_B = k_B T ln\left[\frac{AA^*T^2}{I_s}\right]. \tag{1.6}$$

Equation 1.4 is a better approximation among experimental curves for voltages not including higher forward bias (positive voltage). If the ideality factor approaches unity, the current in the diode is not driven by the potential barrier height for voltages higher than the barrier, but by the series resistance that is always in the circuit. The voltage drop across the resistor increases with current and is critical for limiting current at higher voltages [71]. Therefore, the expression for the current is

$$I = I_s \left[exp\left(\frac{q(V - R_s I)}{\eta k_B T}\right) - 1 \right], \quad (1.7)$$

thus $V_D = V - R_s I$, where V is the applied voltage and R_s is the semiconductor resistance.

1.6 Thesis Outline

In this present work, we will address the synthesis, fabrication, characterizations, and applications of two different types of wide bandgap semiconductors for the development of self-powered photodetectors with ultra-high sensitivity and stability and materials based on non-volatile memory devices.

Chapter 2 will describe all experiment details to fabricate lateral and vertical structures of back-to-back Schottky diode modules to measure the optical responses and the current-voltage effects in a set of metal-semiconductor-metal barriers. In this sense, we will describe two techniques for growing high-quality, large-area, uniform thin films. First, we will synthesize by mechanical exfoliation method to produce 2D tungsten disulfide nanosheets from the bulk material. It will be deposited on a SiO_2/Si substrate using the spin coating technique to obtain a thin film of the exfoliated nanosheets. Second, CO_2 pulsed laser plasma deposition technique will be used to synthesize two-dimensional (2D) hexagonal boron nitride nanosheets (BNNS) on SiO_2/Si and Mo substrates, using hexagonal boron nitride (hBN) target to grow mass-product nanostructures in a significantly short time. Based on both criteria, lateral (Au/WS_2/Au, Au/BNNS/Au) and vertical (Au/BNNS/Mo) heterostructures will be built by deposition of gold atoms using the sputtering technique.

Chapter 3 will describe the main characterization techniques developed to measure the chemical compositions, chemical structure, phase, crystallinity, molecular structure, and absorbance of 2D WS_2 and BN nanosheets; thus outlining their working principles and their relation to the studies carried out in this thesis. In this sense, a brief introduction will be made to the working principles of the characterization instrument, its importance in the analysis, and studies of samples. Therefore, scanning electron microscopy (SEM), energy dispersive X-ray spectroscopy (EDS or EDX), Raman spectroscopy, X-ray diffraction (XRD), and UV-Vis spectrophotometry will be used.

Chapter 4 will focus on the fabrication and application of 2D WS2 nanosheets for high-performance self-powered photodetectors. Therefore, for a detailed study of the synthesis of this material, it will be analyzed by SEM, EDX, XRD, Raman scattering, and UV-visible absorption spectra. A schematic diagram of the bandgap alignment in carrier transport will then be presented, where the Au/WS_2/Au symmetric lateral junction will be studied as a back-to-back Schottky diode, without and with bias voltage under light and dark conditions. Likewise, a schematic set-up for the characterization of the circuit photodetector will be shown, which will be measured in photovoltaic mode operation and bias effect. The device will exhibit photocurrent-time cyclical curves under the illumination of switched on/off at biases from 0 to 2.0 V and will be set in periods of 20 s during several testing cycles when the device will be exposed from 420 to 605 nm at room and high temperatures.

Chapter 5 will study the fabrication and application of 2D boron nitride nanosheets with hysteresis effect in the Schottky junctions. Based on this topic, BNNS structure will be characterized by Raman scattering, SEM, and XRD. The energy band diagram of back-to-back Schottky barriers will then be presented to understand the mechanism of charge carrier transport in Au/BNNS/Au symmetric lateral junction and Au/BNNS/Mo asymmetric vertical junction, respectively. Set up and operation of the current-voltage measurement system will be shown, which will be measured on scales from 0 a 3 V in steps of 0.01 V, both in forward and reverse bias voltages. Hysteresis stability will be exhibited at temperatures from 20 to 170 °C, which will be important for future memory devices or electronic systems. If the operating conditions of Au/BNNS/Au and Au/BNNS/Mo Schottky diodes will be taken from 0 to ±20 V in steps of ±0.1 V, non-ohmic behavior will be dominant, and the hysteresis of BNNS film will be negligible from 20 to 170 °C. However, its applications as rectifiers remain promising due to its low energy loss and high thermal stability.

1.7 References

[1] A.S. Mayorov, R. v. Gorbachev, S. v. Morozov, L. Britnell, R. Jalil, L.A. Ponomarenko, P. Blake, K.S. Novoselov, K. Watanabe, T. Taniguchi, A.K. Geim, Micrometer-scale ballistic transport in encapsulated graphene at room temperature, Nano Lett. 11 (2011) 2396–2399. https://doi.org/10.1021/NL200758B/ASSET/IMAGES/LARGE/NL-2011-00758B_0003.JPEG.

[2] A.A. Balandin, Thermal properties of graphene and nanostructured carbon materials., Nat Mater. 10 (2011) 569–581. https://doi.org/10.1038/NMAT3064.

[3] J. Kinaret, A.C. Ferrari, V. Fal'ko, J. Kivioja, Graphene-Driven Revolutions in ICT and Beyond, Procedia Comput Sci. 7 (2011) 30–33. https://doi.org/10.1016/J.PROCS.2011.12.013.

[4] D. Akinwande, C.J. Brennan, J.S. Bunch, P. Egberts, J.R. Felts, H. Gao, R. Huang, J.S. Kim, T. Li, Y. Li, K.M. Liechti, N. Lu, H.S. Park, E.J. Reed, P. Wang, B.I. Yakobson, T. Zhang, Y.W. Zhang, Y. Zhou, Y. Zhu, A review on mechanics and mechanical properties of 2D materials—Graphene and beyond, Extreme Mech Lett. 13 (2017) 42–77. https://doi.org/10.1016/J.EML.2017.01.008.

[5] S.Z. Butler, S.M. Hollen, L. Cao, Y. Cui, J.A. Gupta, H.R. Gutiérrez, T.F. Heinz, S.S. Hong, J. Huang, A.F. Ismach, E. Johnston-Halperin, M. Kuno, V. v. Plashnitsa, R.D. Robinson, R.S. Ruoff, S. Salahuddin, J. Shan, L. Shi,

M.G. Spencer, M. Terrones, W. Windl, J.E. Goldberger, Progress, challenges, and opportunities in two-dimensional materials beyond graphene, ACS Nano. 7 (2013) 2898–2926. https://doi.org/10.1021/NN400280C/ASSET/IMAGES/LARGE/NN-2013-00280C_0017.JPEG.

[6] A. Singh, A.K. Singh, Atypical behavior of intrinsic defects and promising dopants in two-dimensional WS$_{2}$, Physical Review Materials. 5 (2021) 84001. https://doi.org/10.1103/PhysRevMaterials.5.084001.

[7] S. Manzeli, D. Ovchinnikov, D. Pasquier, O. v. Yazyev, A. Kis, 2D transition metal dichalcogenides, Nature Reviews Materials 2017 2:8. 2 (2017) 1–15. https://doi.org/10.1038/natrevmats.2017.33.

[8] Z. Wang, Y. Zhu, D. Ji, Z. Li, H. Yu, Scalable preparation of 2D boron nitride nanosheets and enhancement of UV absorption and thermal conductivity of cellulose nanofibers membrane, J Mater Sci. 55 (2020) 13815–13823. https://doi.org/10.1007/S10853-020-04954-3/TABLES/1.

[9] N. Choudhary, M.D. Patel, J. Park, B. Sirota, W. Choi, Synthesis of large scale MoS2 for electronics and energy applications, Journal of Materials Research. 31 (2016) 824–831. https://doi.org/10.1557/JMR.2016.100.

[10] S.S. Varghese, S.H. Varghese, S. Swaminathan, K.K. Singh, V. Mittal, Two-Dimensional Materials for Sensing: Graphene and Beyond, Electronics 2015, Vol. 4, Pages 651-687. 4 (2015) 651–687. https://doi.org/10.3390/ELECTRONICS4030651.

[11] P. Forouzandeh, S.C. Pillai, Two-dimensional (2D) electrode materials for supercapacitors, Materials Today: Proceedings. 41 (2020) 498–505. https://doi.org/10.1016/J.MATPR.2020.05.233.

[12] I.M. Datye, A.J. Gabourie, C.D. English, K.K.H. Smithe, C.J. McClellan, N.C. Wang, E. Pop, Reduction of hysteresis in MoS2 transistors using pulsed voltage measurements, 2d Mater. 6 (2018) 011004. https://doi.org/10.1088/2053-1583/AAE6A1.

[13] Design and test of a CMOS image sensor with global shutter and High Dynamic Range., (n.d.). https://www.duo.uio.no/handle/10852/56886?show=full (accessed May 22, 2022).

[14] F. Fernandez, A Focal Plane Array and Electronics Model for CMOS and CCD Sensors in the AFIT Sensor and Scene Emulation Tool (ASSET), Theses and Dissertations. (2019). https://scholar.afit.edu/etd/2256 (accessed May 22, 2022).

[15] P. Centen, Complementary metal-oxide-semiconductor (CMOS) and charge coupled device (CCD) image sensors in high-definition TV imaging, High Performance Silicon Imaging: Fundamentals and Applications of CMOS and CCD Sensors. (2014) 373–410. https://doi.org/10.1533/9780857097521.2.373.

[16] M. El-Desouki, M.J. Deen, Q. Fang, L. Liu, F. Tse, D. Armstrong, CMOS Image Sensors for High Speed Applications, Sensors (Basel). 9 (2009) 430. https://doi.org/10.3390/S90100430.

[17] C. Vicario, C.P. Hauri, M. Shalaby, Single-silicon CCD-CMOS platform for multi-spectral detection from terahertz to x-rays, Optics Letters, Vol. 42, Issue 22, Pp. 4596-4599. 42 (2017) 4596–4599. https://doi.org/10.1364/OL.42.004596.

[18] H. Tian, A. el Gamal, Analysis of 1/f noise in CMOS APS, Https://Doi.Org/10.1117/12.385433. 3965 (2000) 168–176. https://doi.org/10.1117/12.385433.

[19] Photomultiplier tubes for application of toluene detection using Deep-UV Absorption spectrophotometry, (oral presentation & poster & proceedings with peer review) - Archive ouverte HAL, (n.d.). https://hal.archives-ouvertes.fr/hal-02366016 (accessed May 22, 2022).

[20] D.H. Lien, H.P. Wang, S. bin Chen, Y.C. Chi, C.L. Wu, G.R. Lin, Y.C. Liao, J.H. He, 360° omnidirectional, printable and transparent photodetectors for flexible optoelectronics, Npj Flexible Electronics 2018 2:1. 2 (2018) 1–7. https://doi.org/10.1038/s41528-018-0032-2.

[21] Y. Gu, T. Zhang, H. Chen, F. Wang, Y. Pu, C. Gao, S. Li, Mini Review on Flexible and Wearable Electronics for Monitoring Human Health Information, Nanoscale Research Letters. 14 (2019) 1–15. https://doi.org/10.1186/S11671-019-3084-X/FIGURES/11.

[22] D. Baran, D. Corzo, G.T. Blazquez, Flexible Electronics: Status, Challenges and Opportunities, Frontiers in Electronics. 0 (2020) 2. https://doi.org/10.3389/FELEC.2020.594003.

[23] Y. Xu, Z. Shi, X. Shi, K. Zhang, H. Zhang, Recent progress in black phosphorus and black-phosphorus-analogue materials: properties, synthesis and applications, Nanoscale. 11 (2019) 14491–14527. https://doi.org/10.1039/C9NR04348A.

[24] N. Goyal, N. Kaushik, H. Jawa, S. Lodha, Enhanced stability and performance of few-layer black phosphorus transistors by electron beam irradiation, Nanoscale. 10 (2018) 11616–11623. https://doi.org/10.1039/C8NR01678J.

[25] J. Zhao, H. Liu, Z. Yu, R. Quhe, S. Zhou, Y. Wang, C.C. Liu, H. Zhong, N. Han, J. Lu, Y. Yao, K. Wu, Rise of silicene: A competitive 2D material, Progress in Materials Science. 83 (2016) 24–151. https://doi.org/10.1016/J.PMATSCI.2016.04.001.

[26] I. Omkaram, Y.K. Hong, S. Kim, Transition Metal Dichalcogenide Photodetectors, Two-Dimensional Materials for Photodetector. (2017). https://doi.org/10.5772/INTECHOPEN.72295.

[27] K. Thakar, S. Lodha, Optoelectronic and photonic devices based on transition metal dichalcogenides, Materials Research Express. 7 (2020) 014002. https://doi.org/10.1088/2053-1591/AB5C9C.

[28] D. Shakthivel, M. Ahmad, M.R. Alenezi, R. Dahiya, S.R.P. Silva, 1D Semiconducting Nanostructures for Flexible and Large-Area Electronics: Growth Mechanisms and Suitability, 1D Semiconducting Nanostructures for

Flexible and Large-Area Electronics. (2019). https://doi.org/10.1017/9781108642002.

[29] J. Jalilian, M. Safari, Electronic and optical properties of α-InX (X = S, Se and Te) monolayer: Under strain conditions, Physics Letters A. 381 (2017) 1313–1320. https://doi.org/10.1016/J.PHYSLETA.2017.01.024.

[30] K.K. Kam, B.A. Parkinson, Detailed photocurrent spectroscopy of the semiconducting group VIB transition metal dichalcogenides, Journal of Physical Chemistry. 86 (2002) 463–467. https://doi.org/10.1021/J100393A010.

[31] A. Kuc, N. Zibouche, T. Heine, Influence of quantum confinement on the electronic structure of the transition metal sulfide TS2, Physical Review B - Condensed Matter and Materials Physics. 83 (2011) 245213. https://doi.org/10.1103/PHYSREVB.83.245213/FIGURES/6/MEDIUM.

[32] M. Bernardi, C. Ataca, M. Palummo, J.C. Grossman, Optical and Electronic Properties of Two-Dimensional Layered Materials, Nanophotonics. 6 (2017) 479–493. https://doi.org/10.1515/NANOPH-2015 0030/ASSET/GRAPHIC /J_NANOPH-2015-0030_FIG_004.JPG.

[33] M. Chhowalla, H.S. Shin, G. Eda, L.J. Li, K.P. Loh, H. Zhang, The chemistry of two-dimensional layered transition metal dichalcogenide nanosheets, Nat Chem. 5 (2013) 263–275. https://doi.org/10.1038/NCHEM.1589.

[34] M. Planells, B.C. Schroeder, I. McCulloch, Effect of chalcogen atom substitution on the optoelectronic properties in cyclopentadithiophene

polymers, Macromolecules. 47 (2014) 5889–5894. https://doi.org/10.1021/MA5014308/SUPPL_FILE/MA5014308_SI_001.PDF.

[35] Y. Xiao, M. Zhou, J. Liu, J. Xu, L. Fu, Phase engineering of two-dimensional transition metal dichalcogenides, Science China Materials 2019 62:6. 62 (2019) 759–775. https://doi.org/10.1007/S40843-018-9398-1.

[36] V. Sorkin, H. Pan, H. Shi, S.Y. Quek, Y.W. Zhang, Nanoscale Transition Metal Dichalcogenides: Structures, Properties, and Applications, Http://Dx.Doi.Org/10.1080/10408436.2013.863176. 39 (2014) 319–367. https://doi.org/10.1080/10408436.2013.863176.

[37] B. Groven, Y. Shi, P. Morin, al -, H. Salehi Vaziri, A. Shokuhfar, S. Salman Seyyed Afghahi -, J. Ding, A. Feng, X. Li, S. Ding, L. Liu, W. Ren, Properties, preparation, and application of tungsten disulfide: a review, Journal of Physics D: Applied Physics. 54 (2021) 173002. https://doi.org/10.1088/1361-6463/ABD9E8.

[38] B. Mahler, V. Hoepfner, K. Liao, G.A. Ozin, Colloidal synthesis of 1T-WS2 and 2H-WS2 nanosheets: Applications for photocatalytic hydrogen evolution, J Am Chem Soc. 136 (2014) 14121–14127. https://doi.org/10.1021/JA506261T/SUPPL_FILE/JA506261T.

[39] W. Ortiz, C. Malca, D. Barrionuevo, A. Aldalbahi, E. Pacheco, N. Oli, P. Feng, Two-dimensional tungsten disulfide nanosheets and their application in self-powered photodetectors with ultra-high sensitivity and stability,

Vacuum. 201 (2022) 111092. https://doi.org/10.1016/J.VACUUM.2022.111092.

[40] K.M. McCreary, M. Currie, A.T. Hanbicki, H.J. Chuang, B.T. Jonker, Understanding Variations in Circularly Polarized Photoluminescence in Monolayer Transition Metal Dichalcogenides, ACS Nano. 11 (2017) 7988–7994. https://doi.org/10.1021/ACSNANO.7B02554.

[41] H.L. Liu, C.C. Shen, S.H. Su, C.L. Hsu, M.Y. Li, L.J. Li, Optical properties of monolayer transition metal dichalcogenides probed by spectroscopic ellipsometry, Applied Physics Letters. 105 (2014) 201905. https://doi.org/10.1063/1.4901836.

[42] M. Terrones, A. Voshell, M.M. Rana, Review of optical properties of two-dimensional transition metal dichalcogenides, (2018) 21. https://doi.org/10.1117/12.2323132.

[43] M. Shanmugam, T. Bansal, C.A. Durcan, B. Yu, Schottky-barrier solar cell based on layered semiconductor tungsten disulfide nanofilm, Applied Physics Letters. 101 (2012) 263902. https://doi.org/10.1063/1.4773525.

[44] A.K. Patel, B.P. Pandey, Performance Analysis of WS2 TMD Material as an Absorber layer used in Solar Cell, International Conference on Electrical and Electronics Engineering, ICE3 2020. (2020) 382–384. https://doi.org/10.1109/ICE348803.2020.9122856.

[45] N. Sakhuja, R.K. Jha, N. Bhat, Tungsten disulphide nanosheets for high-performance chemiresistive ammonia gas sensor, IEEE Sensors Journal. 19 (2019) 11767–11774. https://doi.org/10.1109/JSEN.2019.2936978.

[46] D.J. Late, R. v. Kanawade, P.K. Kannan, C.S. Rout, Atomically thin WS2 nanosheets based gas sensor, Sensor Letters. 14 (2016) 1249–1254. https://doi.org/10.1166/SL.2016.3764.

[47] S. Sharma, S. Bhagat, J. Singh, R.C. Singh, S. Sharma, Excitation-dependent photoluminescence from WS2 nanostructures synthesized via top-down approach, Journal of Materials Science. 52 (2017) 11326–11336. https://doi.org/10.1007/S10853-017-1303-3/FIGURES/11.

[48] H.G. Ji, P. Solís-Fernández, U. Erkllç, H. Ago, Stacking Orientation-Dependent Photoluminescence Pathways in Artificially Stacked Bilayer WS2Nanosheets Grown by Chemical Vapor Deposition: Implications for Spintronics and Valleytronics, ACS Applied Nano Materials. 4 (2021) 3717–3724. https://doi.org/10.1021/ACSANM.1C00192/SUPPL_FILE/AN1C00192_SI_001.PDF.

[49] R.K. Jha, P.K. Guha, Liquid exfoliated pristine WS2 nanosheets for ultrasensitive and highly stable chemiresistive humidity sensors, Nanotechnology. 27 (2016) 475503. https://doi.org/10.1088/0957-4484/27/47/475503.

[50] G. Chen, H. Li, H. Guan, H. Lu, J. Dong, J. Yu, J. Zhang, M. Jiang, W. Zhu, W. Qiu, X. Wang, Y. Zhong, Y. Luo, Z. Chen, Z. Zhang, Highly sensitive all-

optical control of light in WS_2 coated microfiber knot resonator, Optics Express, Vol. 26, Issue 21, Pp. 27650-27658. 26 (2018) 27650–27658. https://doi.org/10.1364/OE.26.027650.

[51] H. Long, L. Tao, C.Y. Tang, B. Zhou, Y. Zhao, L. Zeng, S.F. Yu, S.P. Lau, Y. Chai, Y.H. Tsang, Tuning nonlinear optical absorption properties of WS2 nanosheets, Nanoscale. 7 (2015) 17771–17777. https://doi.org/10.1039/C5NR04389A.

[52] O. Hod, Graphite and Hexagonal Boron-Nitride have the Same Interlayer Distance. Why?, J Chem Theory Comput. 8 (2012) 1360–1369. https://doi.org/10.1021/CT200880M.

[53] D. Gonzalez Ortiz, C. Pochat-Bohatier, J. Cambedouzou, M. Bechelany, P. Miele, Pickering emulsions stabilized with two-dimensional (2D) materials: A comparative study, Colloids Surf A Physicochem Eng Asp. 563 (2019) 183–192. https://doi.org/10.1016/J.COLSURFA.2018.12.008.

[54] H. Zeng, C. Zhi, Z. Zhang, X. Wei, X. Wang, W. Guo, Y. Bando, D. Golberg, “White graphenes”: Boron nitride nanoribbons via boron nitride nanotube unwrapping, Undefined. 10 (2010) 5049–5055. https://doi.org/10.1021/NL103251M.

[55] A. Freitas, L.D. Machado, C.G. Bezerra, R.M. Tromer, S. Azevedo, Electronic and optical properties of BxCyNz hybrid α-graphynes, RSC Adv. 9 (2019) 35176–35188. https://doi.org/10.1039/C9RA02347J.

[56] W. Xie, T. Tamura, T. Yanase, T. Nagahama, T. Shimada, Rich interfacial chemistry and properties of carbon-doped hexagonal boron nitride nanosheets revealed by electronic structure calculations, Jpn J Appl Phys. 57 (2018) 04FL11. https://doi.org/10.7567/JJAP.57.04FL11/XML.

[57] W. Xie, T. Yanase, T. Nagahama, T. Shimada, Carbon-Doped Hexagonal Boron Nitride: Analysis as π-Conjugate Molecules Embedded in Two Dimensional Insulator, C 2016, Vol. 2, Page 2. 2 (2016) 2. https://doi.org/10.3390/C2010002.

[58] O. Hod, Quantifying the Stacking Registry Matching in Layered Materials, (2010).

[59] L.H. Li, J. Cervenka, K. Watanabe, T. Taniguchi, Y. Chen, Strong oxidation resistance of atomically thin boron nitride nanosheets, ACS Nano. 8 (2014) 1457–1462. https://doi.org/10.1021/NN500059S/SUPPL_FILE/NN500059.

[60] K. Watanabe, T. Taniguchi, H. Kanda, Direct-bandgap properties and evidence for ultraviolet lasing of hexagonal boron nitride single crystal, Nature Materials 2004 3:6. 3 (2004) 404–409. https://doi.org/10.1038/nmat1134.

[61] X. Wang, C. Zhi, Q. Weng, Y. Bando, D. Golberg, Boron Nitride Nanosheets: novel Syntheses and Applications in polymeric Composites, J Phys Conf Ser. 471 (2013) 012003. https://doi.org/10.1088/1742-6596/471/1/012003.

[62] J. Zhao, Z. Chen, Carbon-Doped Boron Nitride Nanosheet: An Efficient Metal-Free Electrocatalyst for the Oxygen Reduction Reaction, Journal of

Physical Chemistry C. 119 (2015) 26348–26354. https://doi.org/10.1021/ACS.JPCC.5B09037/ASSET/IMAGES/LARGE/JP-2015-090378_0007.JPEG.

[63] Y.J. Min, K.H. Kang, D.E. Kim, Development of polyimide films reinforced with boron nitride and boron nitride nanosheets for transparent flexible device applications, Nano Research 2017 11:5. 11 (2018) 2366–2378. https://doi.org/10.1007/S12274-017-1856-0.

[64] C. Teng, L. Su, J. Chen, J. Wang, Flexible, thermally conductive layered composite films from massively exfoliated boron nitride nanosheets, Compos Part A Appl Sci Manuf. 124 (2019) 105498. https://doi.org/10.1016/J.COMPOSITESA.2019.105498.

[65] X. Zou, C.-W. Huang, L. Wang, L.-J. Yin, W. Li, J. Wang, B. Wu, Y. Liu, Q. Yao, C. Jiang, W.-W. Wu, L. He, S. Chen, J.C. Ho, L. Liao, X. Zou, W. Li, J. Wang, C. Jiang, L. Liao, C.-W. Huang, -W W Wu, L. Wang, B. Wu, Y. Liu, L.-J. Yin, L. He, Q. Yao, S. Chen, C. Ho, Dielectric Engineering of a Boron Nitride/Hafnium Oxide Heterostructure for High-Performance 2D Field Effect Transistors, Advanced Materials. 28 (2016) 2062–2069. https://doi.org/10.1002/ADMA.201505205.

[66] K. Zhang, Y. Feng, F. Wang, Z. Yang, J. Wang, Two dimensional hexagonal boron nitride (2D-hBN): synthesis, properties and applications, J Mater Chem C Mater. 5 (2017) 11992–12022. https://doi.org/10.1039/C7TC04300G.

[67] Y. Jiang, X. Shi, Y. Feng, S. Li, X. Zhou, X. Xie, Enhanced thermal conductivity and ideal dielectric properties of epoxy composites containing polymer modified hexagonal boron nitride, Compos Part A Appl Sci Manuf. 107 (2018) 657–664. https://doi.org/10.1016/J.COMPOSITESA.2018.02.016.

[68] C. Zhao, Z. Xu, H. Wang, J. Wei, W. Wang, X. Bai, E. Wang, Carbon-Doped Boron Nitride Nanosheets with Ferromagnetism above Room Temperature, Adv Funct Mater. 24 (2014) 5985–5992. https://doi.org/10.1002/ADFM.201401149.

[69] R.F. Graf, I, Modern Dictionary of Electronics. (1999) 359–399. https://doi.org/10.1016/B978-0-08-051198-6.50014-X.

[70] Y. Dan, X. Zhao, K. Chen, A. Mesli, A Photoconductor Intrinsically Has No Gain, ACS Photonics. 5 (2018) 4111–4116. https://doi.org/10.1021/ACSPHOTONICS.8B00805/ASSET/IMAGES/LARGE/PH-2018-008054_0004.JPEG.

[71] R. Nouchi, Extraction of the Schottky parameters in metal-semiconductor-metal diodes from a single current-voltage measurement, Journal of Applied Physics. 116 (2014) 184505. https://doi.org/10.1063/1.4901467.

Chapter 2

Experimental methods

In this study, experiments were conducted to fabricate lateral and vertical structures with simple back-to-back Schottky diode modules designed to measure the optical responses and the current-voltage effects in a set of barrier metals/semiconductors/metals. Based on this criterion, Au/WS_2/Au, Au/BNNS/Au, and Au/BNNS/Mo heterostructures were built with particularly interesting features in the application of 2D materials. Hence, the main purpose will be to present all details of the experiments and the mechanism of operation under specific measurement conditions to determine the electrical and optical properties of the device. In addition, schematics of the purpose of the method will be remarked on for a precise-comprehension aid of the principal parts of this thesis.

2.1 Experiment purpose

Back-to-back Schottky junction devices were fabricated in this experiment with Au electrodes on 2D WS_2 and BN nanosheets on SiO_2/Si and Mo substrates. Especially, the prototypes present lateral and vertical geometries, where Au/WS_2/Au and Au/BNNS/Au contacts are on the same horizontal plane, while Au/BNNS/Mo is a vertical structure. The electric and optical properties of these devices are attractive due to their remarkable high sensitivity bandwidth, ease of fabrication, and integration with other electronic components into monolithic integrated circuits. Of all these possibilities, lateral photodetectors seem to attract a great deal of interest due to their low capacitance Schottky barrier diode. M.E.P.

Tweedie et al. [1] developed a transparent ultrathin all-two-dimensional lateral Gr/WS_2/Gr photodetector array on flexible substrates, with ease of large-scale fabrication. The device presented a highly stable photoconductance over a range of illumination powers, demonstrating that lateral heterostructure designs are a new simpler way of high-performance optimal photodetectors. Similarly, O. Tenghui et al. [2] investigated a lateral photodiode based on $MoTe_2$/WS_2/$MoTe_2$ heterojunctions, in which electron-hole pairs were generated in the 2D layers and Schottky junctions upon light illumination, which greatly benefited photodetection. R. Steinhagen et al. [3] also studied the use of fiber-coupled ultra-fast metal-semiconductor-metal photodetector as a possibility to measure signals derived from electro-optical, synchrotron-light-source-based diagnostics systems. Since modern particle accelerators are often governed by the ability to control beam stability. A. Aldalbahi et al. [4] presented BNNS-based DUV photodetectors in an Au–BNNS Schottky lateral contact, where the prototype was very good repeatability and stability features in a wide temperature range for the wavelength region from 250 nm to 350 nm. These results suggest that electron mobility and concentration-related charge carrier transport properties in BNNS structures seem to be highly attractive for future technologies, which has motivated the search for more improved structures for potential applications. Vertical contacts are a special case of back-to-back Schottky diodes of higher capacitance than lateral contacts. The design of its construction enables it to produce a more stable hysteresis under certain current-voltage curve measurements, even in high-temperature environments. These remarkable characteristics may be used in non-volatile

memory technologies. A. F. Zhou et al. [5] characterized vertical Al/BNNS/Mo deep UV photodetectors and demonstrated a stable operation from room temperature to 100 °C. This confirmed that the prototype also had a good spectral response. However, in the fabrication of MSM devices, our experimental technique is more effective and simpler, as it can cover wide wavelength detection ranges starting from the near-infrared (IR) to near UV spectrum. Thus, marking the difference with the rest of the devices similar to ours.

As for the metal contacts, Au was elected as the contact electrode because it is a good conductor of both electricity and heat. Copper and silver are also considered the best conductors, but gold connections can outlast both of them because they do not tarnish, which means it remains conductive for a longer time. In addition, H. A. Atwater et al. [6] demonstrated that Au was homogeneously semitransparent and that there were no visible bubbles created during the metal transfer process with the TMD. N. Bernhardt et al. [7] deposited a sputtered gold film about hBN \and resulted in a stronger bond to the topmost layers, thus allowing better adherence to the sample. These junctions contributed to the uniformity of the photocurrent in the Schottky junction photovoltaic device. On the other hand, the SiO_2/Si substrates are suitable materials for growing high-quality, large-area, uniform thin films. It is characterized by having good abrasion resistance, high thermal stability, electrical insulation, and amorphous nature.

Hence, the main purpose of this study was to design lateral and vertical contact back-to-back Schottky diode prototypes by forming Au electrodes on 2D WS_2 and BN nanosheets on SiO_2/Si and Mo substrates. Following this model, it is

intended to suggest an innovative and economically viable design device with a simple fabrication procedure for broadband photodetection and optoelectronic device applications.

2.2 Spin coating technique

The spin coating technique is used to deposit uniform thin films in the thickness range of micrometer to nanometer onto flat substrates by using centrifugal force. The force of inertia, viscous force, gravitational force, and surface tension are forces that are used for the spin coating process; and are the main causes of flat deposition on the surface. Thanks to its simplicity and inexpensiveness, the apparatus is widely used by the microelectronics industry, research, and technology sectors. There are many advantages offered by the coating operation with its primary benefit being the absence of coupled process variables. The thin film thickness is easily changed by changing the spin speed of the spin coater or switching to a different viscosity of the liquids. As compared with other deposition techniques, where there are too many parameters that need to be controlled and more complex methods, the spin coating process can produce high-quality thin films at a low-cost production and with a fast-porting time. T. D. Anthopoulos et al. [8] demonstrated that spin coating was the simplest and most cost-effective technique than that synthesized by chemical vapor deposition (CVD) processes during the growth of MoS_2 and WS_2 thin film as a hole transport layer for applications in highly efficient organic solar cells. J. A. Mera-Córdoba et al. [9] also indicated that the technique was useful to synthesize Perovskite thin films of high crystalline quality and nanometric size. Similarly, R. Mastria et al. [10] showed

the in-plane aligned colloidal 2D WS_2 nanoflakes deposited on glass substrates by spin coating were compact and homogeneous in a wide range of organic solvents. Thus, demonstrating that it is possible to obtain thin films with smooth and compact morphology under this method.

2.2.1 Spin coating operation

This section describes the details of the spin coating operation, as well as all the essential instruments to clarify how the system works. In this sense, we examine the parameters that must be optimized in the growth process of two-dimensional WS_2 thin films under atmospheric conditions, room temperature, and controllable humidity.

The vacuum pump and nitrogen tank are the main elements in the operation of the spin coating in a house vacuum environment, as shown in Figure 2.1(a). WS-400B-6NPP/LITE/8k spin coater has characteristics identical or equal to a variety of equipment that exists in industries and labs. Due to its weight, size, space, and easy transportation, it is accessible to researchers and students, which makes them the most widely used in several scientific applications. It is necessary to understand the operating mechanism of the equipment, before being carried out the deposition of the sample on the given substrate. Therefore, we present the details and main steps for the proper handling of the instrument.

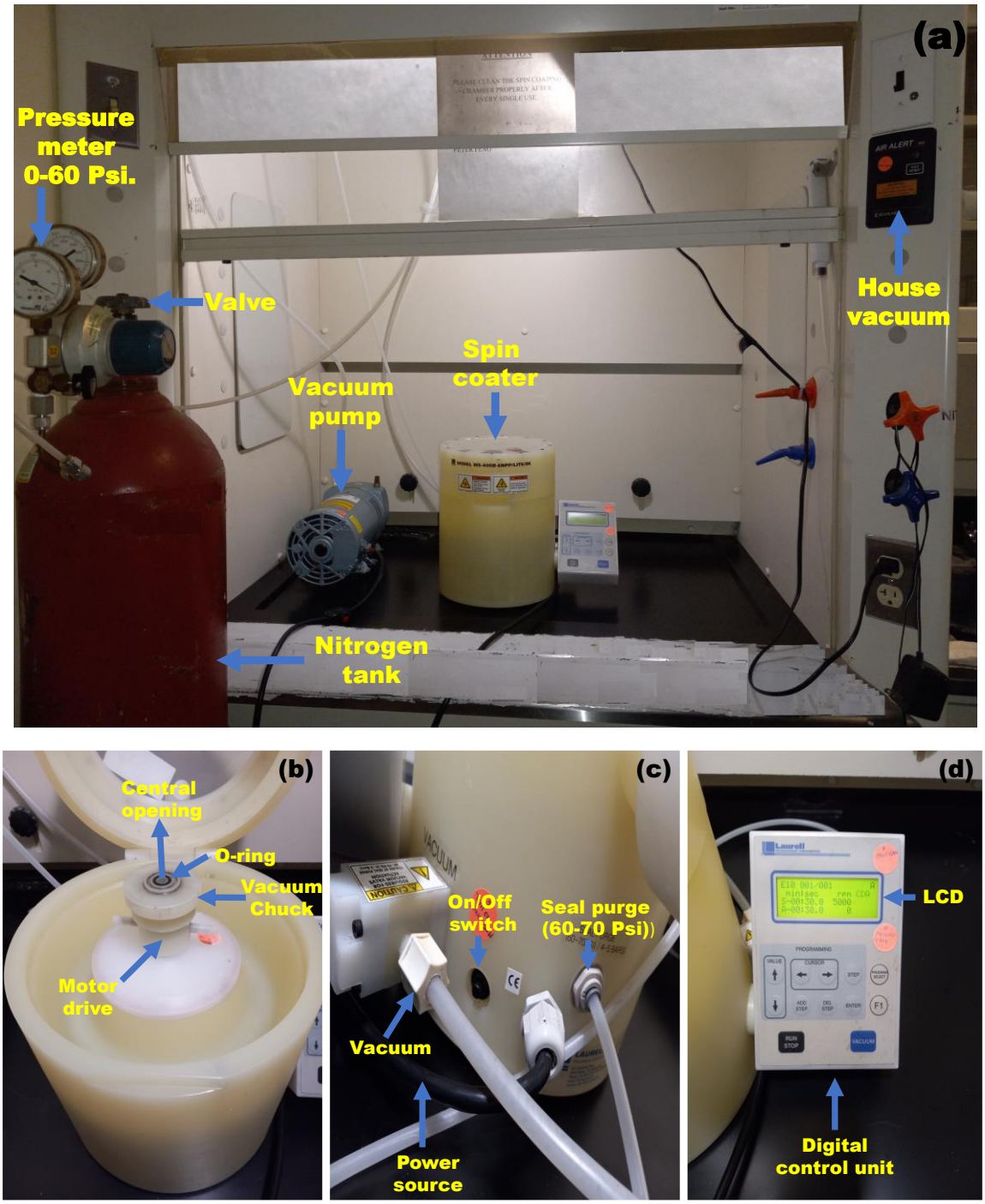

Figure 2. 1 shows **(a)** Spin coater system components; **(b)** WS-400B-6NPP/LITE/8k spin coater fitted with an O-ring and vacuum chuck; **(c)** The back of the machine connected to a power source, vacuum extractor, a nitrogen inlet port, and an on/off switch; and **(d)** digital controller unit with LCD.

The first step is to turn on the house vacuum on the wall to remove impurities and humidity from the environment that could be detrimental to the growth of thin films. Then the cover is opened, place the wafer on top of the chuck using a tweezer, and close again, as shown in Figure 2.1(b). When turning on the spin coater (Figure 2.1(c)), CDA should be immediately displayed on the liquid-crystal display (LCD) of the controller, indicating there is no vacuum applied yet (Figure 2.2(d)). Now we make sure the nitrogen tank valve is open and that the pressure meter shows 60 Psi., which is the magnitude required in the equipment operation. The valve connecting the nitrogen to the spin coater is then slowly opened, which will change from CDA to LID guaranteeing that there is enough vacuum to allow spin from 300 to 5000 rpm. Pressing the "Vacuum" button on the digital control unit locks the substrate wafer down on the chuck, making the display stop flashing the word “VACUUM,” and instead display a number between 23.5 to 25.5. It is important to verify that the wafer is well placed and that it covers the entire chuck to exceed the number 23.5; otherwise, will not run the spinner. If we want to change the speed and spin times, we press the "Program select" button and select the values using the UP/DOWN arrow keys, confirming with the "F1" key. If we need to customize any program or create a new one, we hold down the “F1” key and follow the programming instructions [11,12]. When all changes have been made, we press RUN/STOP, which will start the spin of the chuck with the wafer. Immediately after the spin coating cycle, the gas flow must close and CDA must be indicated on the LCD. This procedure will be the method used for the fabrication of the thin film.

2.3 Fabrication Procedure

The following section thoroughly describes how the synthesis was carried out in the fabrication of an Au/WS_2/Au photodetector on a SiO_2/Si substrate. In addition, providing the reader with comprehensive information about the techniques used.

2.3.1 Synthesis

WS_2 nanopowder (99% trace metal basis) and 90 nm avg part size were synthesized at a concentration of 1 mg/ml in a mixture of ethanol 90%, methanol 5%, and isopropanol 5%. 1.5 g of WS_2 was dispersed in a 500 ml Pyrex beaker with a magnetic stir bar placed within a solution volume of 250 ml, as shown in Figure 2.2. A digital stir plate drives the stir bar's motion beneath the vessel containing the solution for 2 hours at 450 rpm. Then it was sonicated in a 500 W ultrasonic processor at 60 Hz amplitude with pulse On and Off times of 10 s for 10 hours until a complete suspension of the powder in the solvent was achieved. Centrifugation at 3500 rpm for 30 min separated the suspended nanosheets from partially exfoliated WS_2. After standing for a few days in the Falcon beaker of 50 ml, three-fifths of the supernatants were collected using a 5 ml pipette, respectively. The low boiling point of solvents allows exfoliated nanosheets to have no extra steps required to remove the solvents since these are not pristine. Bulk TMDs crystals which have been exfoliated in solvents such as polymer solutions, N-Methyl-2- pyrrolidone (NMP), dimethylformamide (DMF), or surfactant solutions, are usually difficult to remove from the surface of exfoliated nanosheets [13-15].

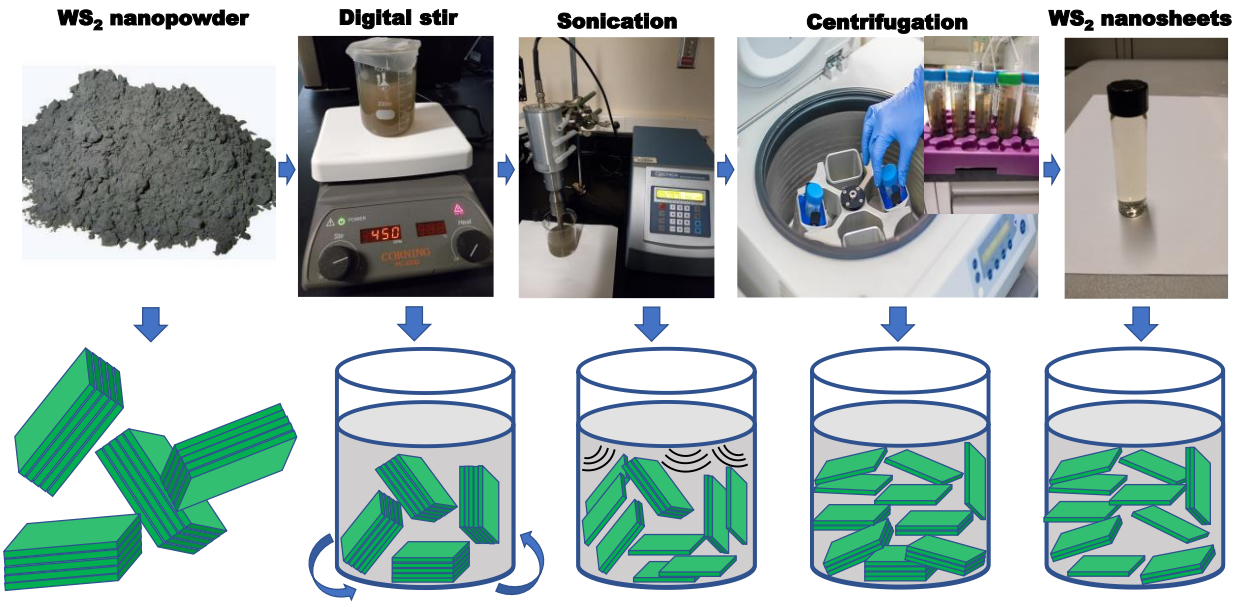

Figure 2. 2 Preparation of liquid-phase exfoliation of WS_2 nanopowder at a concentration of 1 mg/ml in a mixture of ethanol, methanol, and isopropanol.

We chose a 1x1 cm^2 SiO_2/Si substrate to assess the optimum conditions of the 2D WS_2 nanosheets. The material was carefully placed in a beaker and enough acetone was added to ensure it was fully immersed, as shown in Figure 2.3. This was supported over the tap water in the ultrasonic cleaning tank using a beaker cover or basket that immersed it about 3 cm in the water. The ultrasonic energy penetrated the glass walls for 15 minutes removing organic impurities or foreign contaminants; followed by isopropanol, which removed contaminated acetone before it could form streaks on the substrate surface; then, it was dried at 100 °C for 15 minutes using a hot plate. The spin coating method was used to produce thin films with uniform thickness ranging. The exfoliated liquid was loaded onto the center of the substrate and spun for 15 seconds at 1200 rpm until the coating material spread on the whole surface edge. This sample was dried at 200 °C on a

hot plate for 2 minutes to remove the solvent from the solution and monitor film growth. This procedure was repeated until a uniform surface of the WS_2 nanosheets was achieved, leaving a thin film of coating on the substrate. Then, the gold electrode elements were deposited in a vacuum chamber under an argon gas environment at a pressure of 5 to 8 mTorr by a sputtering technique at a power level of 150 watts, where the aluminum foil was used as a mask to protect the middle portion of the thin film. The sputtering for 1 minute yielded around 6 nm gold film on a 52 nm thick, 5 mm wide, and 1 mm long WS_2 film.

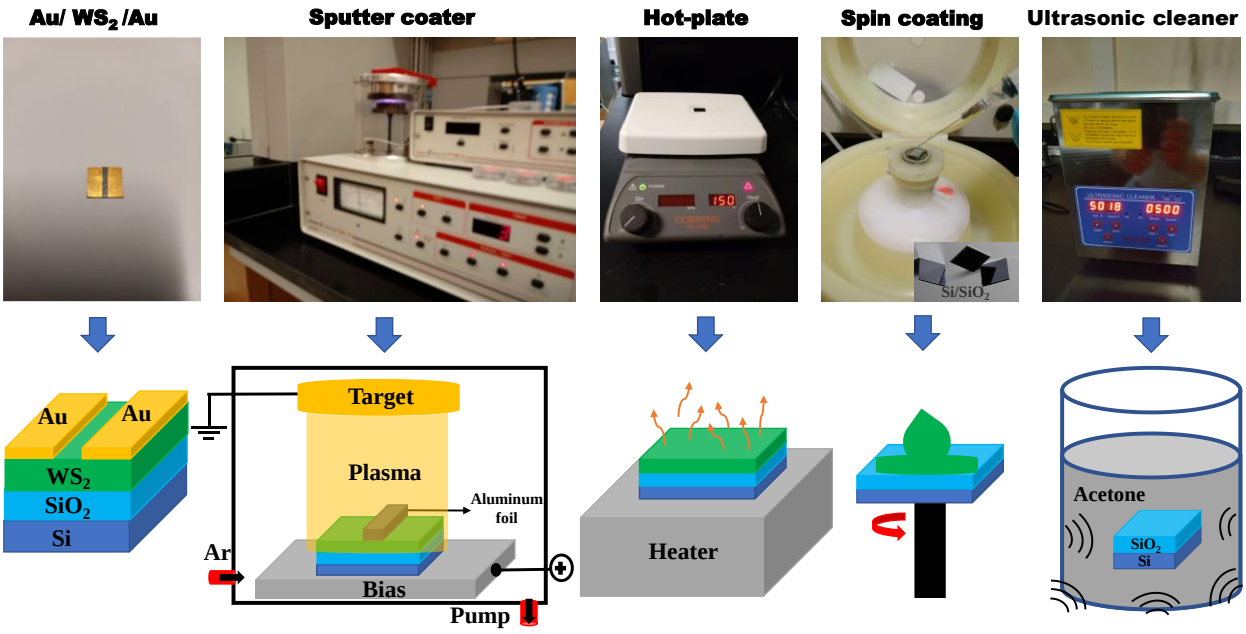

Figure 2. 3 Preparation in the fabrication of an Au/WS_2/Au photodetector by spin coating and sputtering techniques. 2D WS_2 nanosheets cover the entire surface of SiO_2/Si, while the thin film of the gold layer is deposited on two edges of the sample for the photogenerated charge carrier collection.

2.4 Pulse Laser Plasma Deposition Technique

Pulsed laser deposition (PLD) is a physical vapor deposition technique that uses high-energy laser light to evaporate target material, creating a deposition vapor into the vacuum chamber that can then condense onto the surface of the substrate to produce versatile thin films of different materials. This technique typically uses high-temperature and low pressure to grow BNNSs and has proven to be one of the most attractive methods for synthesizing high-yield thin films. One of the advantages of our PLD system is that it largely prevents contamination of the film layer after deposition, thereby avoiding changes to its high purity after condensation has taken place. Additionally, the laser is installed outside the chamber; this makes the operation of plasma deposition a highly flexible laser optical system, placing the system in a unique position to support a range of research.

In the fabrication of BNNS, the role of carbon dioxide (CO_2) in the PLD system was also considered. The CO_2 laser produces coherent radiations in the far infrared (FIR) range, 10.6 micrometers, and is used for produces a larger heating effect upon impact on the target surface to produce a plasma plume composed of high energy ions due to electronic relaxation of excited C, N, H, O, ionic fragments C^+, C^{2+}, C^{3+}, C^{4+}, and molecular features of C_2 [16], thereby the reactive species of the material to be deposited are created. Plasma plume morphology may have spherical to cylindrical geometry changes, depending on the varying pressure levels of the deposition environment within the vacuum chamber [17]. T. Donnelly et al. [18] presented the high electrical efficiency of a

CO_2 laser as a simple plasma shutter device, where the long wavelength (10.6 μm) of CO_2 laser radiation ensured that the laser-produced plasma emission in a 2% band centered on 13.5 nm was the leading candidate in high-volume manufacturing of computer processors and memory components than optical and near-infrared lasers.

In our study, we installed a CO_2-pulsed laser plasma deposition (CO_2-PLD) system for the quick synthesis of BNNSs in a series of experiments, using the hBN target to grow mass-product nanostructures in a significantly short time.

2.4.1 Steps for the installation of CO_2-Pulsed Laser Plasma Deposition System

In this experimental section, we installed a CO_2-pulsed laser plasma deposition (CO_2-PLD) system to quickly produce BN nanostructures and nanosheets by a simple method. Each part of CO_2- PLD system consists of a laser beam, sample holder, shutter, heater, type of gas, and gas flow rate, which can be controlled independently to assess the different experimental conditions in the growth of BNNS thin film on the substrate surface. After the equipment was installed, a series of experiments were carried out using h-BN targets. SEM analysis revealed that the entire surface of the substrate was covered with disk shape BN nanostructures; indicating a relatively short time to grow large-scale materials.

2.4.2 Experimental parameters

During this process, several experimental parameters were set to install CO_2-PLD system. The main components in the equipment operation are a laser machine, deposition chamber, CH_4 tank, vacuum pump, CO_2 tank, temperature box, heater DC power supply, and motor DC power supply, shown in Figure 2.4(a). While in the equipment back is connected to CO_2 gas inlet and out, cooling water in and out, and digital control, as shown in Figure 2.4 (b). Inside the vacuum chamber, devices, and equipment are installed to optimize and control the condensing of the plasma vapor on a substrate, as shown in Figure 2.4(c). It is important to keep the vacuum chamber clean because water molecules can slow the pump downtime. The humidity from the air normally attaches to the chamber walls or can get embedded deep within crevices, generating additional charges to the gas. The schematic diagram of the vacuum chamber and deposition mechanism is shown in Figure 2.4(d), where the designed components consist of a heater, a thermocouple, a substrate holder, a target, and a motor, which are carefully optimized before each deposition process. In addition, the PLD system has a digital remote control with key switches used to control the laser and a display to monitor the laser state and error messages, as shown in Figure 2.4(e).

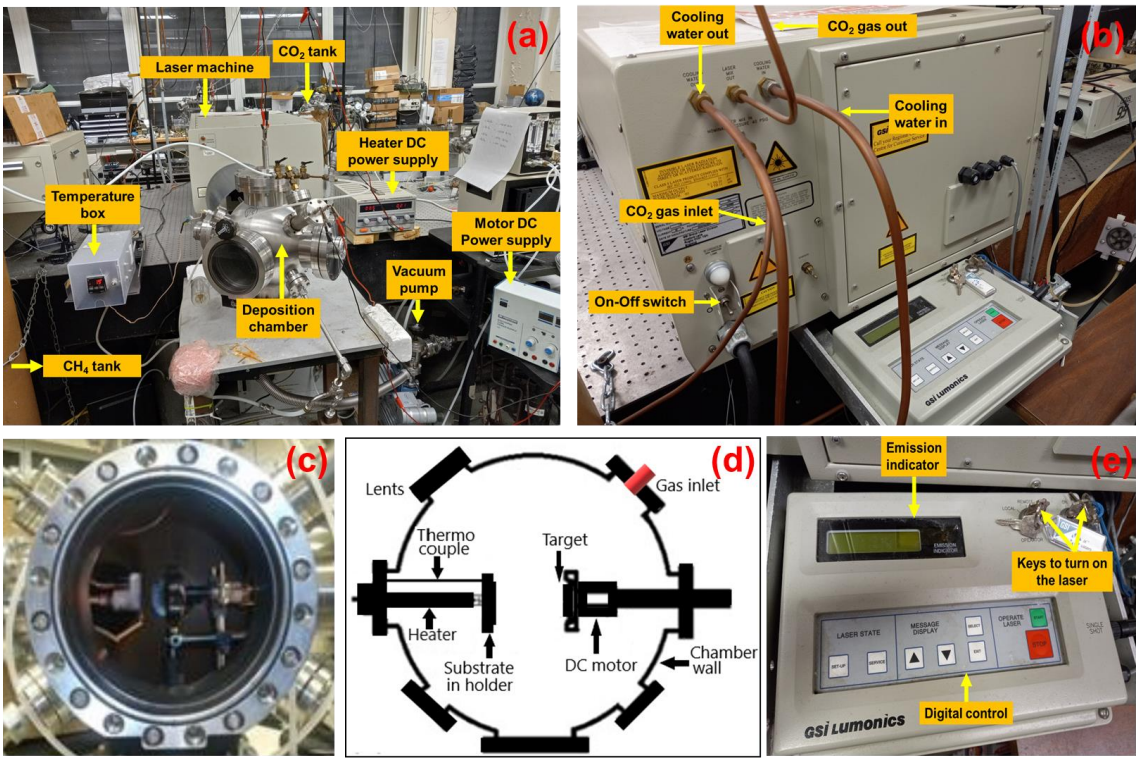

Figure 2. 4 (a) CO_2-PLD system components, **(b)** CO_2-PLD reverse part components, **(c)** inside view of the deposition chamber, **(d)** schematic view of the deposition chamber, and **(e)** digital remote control with emission indicator.

2.4.3 PLD operation

First, the target on the target holder is placed until this is tightly held. It is important to not over-tighten the screws, or else the target will break. Then we check the rotating motor and target holder to make sure it is working properly.

Secondly, the previously washed substrate is placed (see synthesis process) on the holder. This requires that the screw of the holder clamps be loosened to place the substrate, and it is screwed down until tight with the substrate. A temperature

meter is then placed on the surface of the substrate holder to control deposition conditions. Finally, the chamber closes.

Third, the CO_2 tank is loosened, and the laser is switched on using the first right key and then the left one. The next step is to press the Set-Up Button, then look for EXTERNAL by using up and down arrows. When found, EXTERNAL must be selected and changed to INTERNAL. Once everything is ready, the shelter is opened, which is in front of the laser.

Fourth, it must be connected the temperature box to the AC power supply and perform accurate temperature monitoring of the substrate through a digital display. Then vacuum the pump and unscrew slowly turn it on until it is on maximum. This process will remove air and other gases, which will create a low-pressure environment in the deposition chamber. When the pressure hand points within the 400 mTorr, the water-cooling system can be turned on, and then the turbo pump for 15-20 minutes to accelerate air extraction until the pressure meter points at 0. To heat the substrate, the heater and supply DC voltage turn on in abeyance for 2 minutes when it arrives at 5 V, 10 V, and 15 V.

Fifth, the DC motor turns on to rotate the target (24 rev/min) with constant speed to ensure uniform ablation. Next is to write down the number of shots on the laser screen, which starts when START and STOP are pressed to stop. Each time this sequence is repeated, the numbers must be written again.

To shut down the PLD system, the steps are: (1) close the shelter of the laser, (2) close the CH_4 tank valve; (3) lower voltage and current slowly and switch

off the power supply; (4) turn off the turbo pump (we make sure vacuum pump is working until turbo pump stops spinning), (5) close the cooling water system; (6) turn off the laser (First keys, second button), (7) close the CO_2 tank valve of the laser. When the system has cooled, the chamber clamp can be slowly loosened and opened to take the deposited sample.

2.5 Fabrication procedure of lateral and vertical contact

The following section thoroughly describes how the synthesis was carried out in the fabrication of Au/BNNS/Au and Au/BNNS/Mo prototypes on SiO_2/Si and Mo substrates.

2.5.1 Synthesis

A hexagonal Boron Nitride (hBN) sputtering target of 99.9% pure and 2.00" diameter x 0.125" thickness was chosen as shown in Figure 2.5 (a). Similarly, SiO_2/Si and Mo substrates of 5x1 mm^2 and 1 cm diameter x 0.5 mm thickness were used (Figure 2.5 (b)) to assess the optimum conditions of BN nanosheet structures. To remove organic impurities or foreign contaminants from the substrates, a Pyrex graduated beaker was used with enough acetone on regular tap water for ultrasonic cleaning for 15 minutes. Then, it was dried at 100 °C for 15 minutes using a hot plate.

A CO_2-pulsed laser-produced plasma deposition (CO_2 - PLD) technique with a laser wavelength of 10.6 μm and an output power of 75 W was used. Pulsed laser beam irradiated hexagonal Boron Nitride (hBN) target at 200 mTorr pressure of CH_4 environment in the vacuum chamber, as shown in Figure 2.5 (c). The

distance (d) between the target and the substrate (SiO_2/Si or Mo) could be adjusted to control the BNNS film growth rate, in the present case, d = 3 cm was selected. The idea was to achieve stoichiometric nanostructure growth with a B/N ratio near 1. Since the laser plasma deposition consists of ionic and molecular processes, it is possible that at a longer distance, boron and nitrogen ions recombine into molecules before reaching the substrate, which might affect the boron/nitrogen (B/N) ratio. At higher beam energies, the distance between the substrate and the target must be larger so that the high-energy plasma ions would not destroy the initially grown sample.

In contrast, the laser incident angle relative to the target plane was set at 45° to avoid overlapping with the plume, as shown in Figure 2.5 (d). The power density was 2×10^8 W/cm^2 per pulse, and the pulse repetition frequency was 5 Hz. In addition, two special lenses were used; the first was for focusing and the second was as CO_2 laser window so that the laser pulses hit the target accurately. If the angle was too small, the location of the light spots would have been difficult to control, while if the angle was too larger, the substrate holder would have obstructed the incident beam. Thus, the angle is an important parameter in the PLD technique. To get uniform deposition, the DC motor was optimized at 24 rpm; this way, the plasma plume also rotated with the target and covered the entire substrate surface. The deposition was kept at 300 °C for 20 min until thin films were achieved, as shown in Figure 2.5(e).

Then, the sputtering coating technique was used to deposit gold atoms in a vacuum chamber under an argon gas environment at a pressure of 5 to 8 mTorr

and a power level of 150 watts. The aluminum foil was used as a mask to protect the middle portion of the sample, where the sputtering for 1 minute yielded around 6 nm gold film on a 4 nm thickness BNNS films, as shown in the actual and illustrative image (Figures 2.5 (f) and (g)). Finally, prototypes of lateral and vertical contact were obtained, as shown in Figure 2.5 (h).

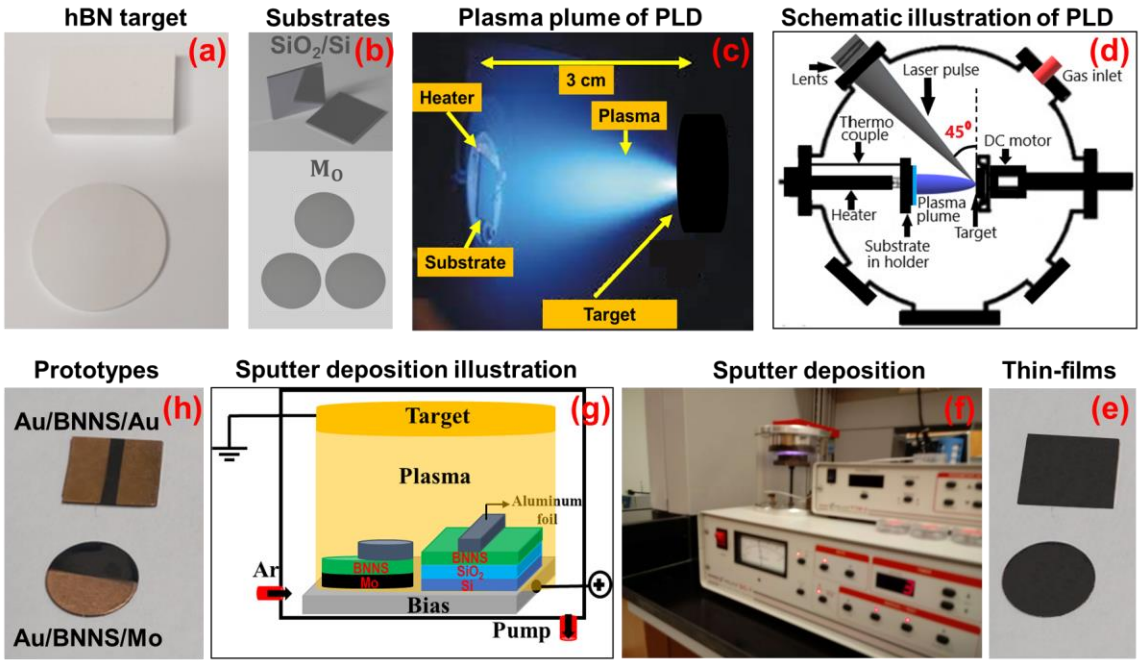

Figure 2. 5 In the synthesis of BNNS thin films with lateral and vertical contact, the following materials are used: **(a)** an hBN target of 99.9% pure, **(b)** SiO_2/Si and Mo substrates; **(c)-(d)** a plasma deposition chamber with a laser incidence angle of 45 relatives to the target plane. After deposition, **(e)** substrate surfaces are completely covered by BNNSs. Then, **(f)-(g)** the sputtering coating deposit gold atoms on the aluminum foil and BNNS samples. **(h)** Finally, Au/BNNS/Au and Au/BNNS/Mo contact prototypes are gotten.

2.6 References

[1] M.E.P. Tweedie, C.S. Lau, L. Hou, X. Wang, Y. Sheng, J.H. Warner, Transparent ultrathin all-two-dimensional lateral Gr:WS2:Gr photodetector arrays on flexible substrates and their strain induced failure mechanisms, Materials Today Advances. 6 (2020). https://doi.org/10.1016/J.MTADV.2020.100067.

[2] T. Ouyang, X. Wang, S. Liu, H. Chen, S. Deng, A Complete Two-Dimensional Avalanche Photodiode Based on MoTe2−WS2−MoTe2 Heterojunctions With Ultralow Dark Current, Frontiers in Materials. 8 (2021) 303. https://doi.org/10.3389/FMATS.2021.736180/BIBTEX.

[3] R. Steinhagen, M. Boland, T. Lucas, R. Rassool, T. Geoffrey Lucas, R. Paul Rassool, Application of Metal-Semiconductor-Metal (MSM) Photodetectors for Transverse and Longitudinal Intra-Bunch Beam Diagnostics, (2013).

[4] A. Aldalbahi, M. Rivera, M. Rahaman, A.F. Zhou, W.M. Alzuraiqi, P. Feng, High-Performance and Self-Powered Deep UV Photodetectors Based on High Quality 2D Boron Nitride Nanosheets, Nanomaterials (Basel). 7 (2017). https://doi.org/10.3390/NANO7120454.

[5] P. Feng, A. Aldalbahi, A.F. Zhou, Vertical metal-semiconductor-metal deep UV photodetectors based on hexagonal boron nitride nanosheets prepared by laser plasma deposition, Optical Materials Express, Vol. 6, Issue 10, Pp. 3286-3292. 6 (2016) 3286–3292. https://doi.org/10.1364/OME.6.003286.

[6] C.M. Went, J. Wong, P.R. Jahelka, M. Kelzenberg, S. Biswas, M.S. Hunt, A. Carbone, H.A. Atwater, A new metal transfer process for van der Waals contacts to vertical Schottky-junction transition metal dichalcogenide photovoltaics, Science Advances. 5 (2019). https://doi.org/10.1126/SCIADV.AAX6061/SUPPL_FILE/AAX6061_SM.PDF.

[7] N. Bernhardt, N. Bernhardt, S. Kim, S. Kim, J.E. Fröch, S.J.U. White, N.M.H. Duong, Z. He, B. Chen, J. Liu, I. Aharonovich, I. Aharonovich, A.S. Solntsev, A.S. Solntsev, Large few-layer hexagonal boron nitride flakes for nonlinear optics, Optics Letters, Vol. 46, Issue 3, Pp. 564-567. 46 (2021) 564–567. https://doi.org/10.1364/OL.416564.

[8] B. Adilbekova, Y. Lin, E. Yengel, H. Faber, G. Harrison, Y. Firdaus, A. El-Labban, D.H. Anjum, V. Tung, T.D. Anthopoulos, Liquid phase exfoliation of MoS2 and WS2 in aqueous ammonia and their application in highly efficient organic solar cells, Journal of Materials Chemistry C. 8 (2020) 5259–5264. https://doi.org/10.1039/D0TC00659A.

[9] J.A. Mera-Córdoba, M.A. Mera-Córdoba, C.A. Córdoba-Barahona, J.A. Mera-Córdoba, M.A. Mera-Córdoba, C.A. Córdoba-Barahona, Spin Coating technique for obtaining nanometric thin films in the system La0.7Sr0.3MnO3, Revista Facultad de Ingeniería. 26 (2017) 125–133. https://doi.org/10.19053/01211129.V26.N44.2017.5293.

[10] R. Mastria, R. Scarfiello, D. Altamura, C. Giannini, A. Liscio, A. Kovtun, G.V. Bianco, G. Bruno, V. Grillo, A.H. Tavabi, R.E. Dunin-Borkowski, C. Nobile,

A. Cola, P.D. Cozzoli, S. Gambino, A. Rizzo, In-plane Aligned Colloidal 2D WS2 Nanoflakes for Solution-Processable Thin Films with High Planar Conductivity, Scientific Reports 2019 9:1. 9 (2019) 1–13. https://doi.org/10.1038/s41598-019-45192-1.

[11] LAURELL SPIN COATER OPERATION 1. Equipment Operation, (n.d.).

[12] Laurell Spin Coater Standard Operating Procedure, (n.d.).

[13] V. Vega-Mayoral, C. Backes, D. Hanlon, U. Khan, Z. Gholamvand, M. O'Brien, G.S. Duesberg, C. Gadermaier, J.N. Coleman, Photoluminescence from Liquid-Exfoliated WS2 Monomers in Poly(Vinyl Alcohol) Polymer Composites, Advanced Functional Materials. 26 (2016) 1028–1039. https://doi.org/10.1002/ADFM.201503863.

[14] C. Berrueco, P. Álvarez, S. Venditti, T.J. Morgan, A.A. Herod, M. Millan, R. Kandiyoti, Sample contamination with NMP-oxidation products and byproduct-free NMP removal from sample solutions, Energy and Fuels. 23 (2009) 3008–3015. https://doi.org/10.1021/EF900036M/ASSET/IMAGES/LARGE/EF-2009-00036M_0011.JPEG.

[15] A. O'Neill, U. Khan, J.N. Coleman, Preparation of High Concentration Dispersions of Exfoliated MoS2 with Increased Flake Size, Chemistry of Materials. 24 (2012) 2414–2421. https://doi.org/10.1021/CM301515Z.

[16] J.J. Camacho, L. Díaz, M. Santos, D. Reyman, J.M.L. Poyato, Optical emission spectroscopic study of plasma plumes generated by IR CO2

pulsed laser on carbon targets, J Phys D Appl Phys. 41 (2008) 105201. https://doi.org/10.1088/0022-3727/41/10/105201.

[17] P.K. Diwakar, S.S. Harilal, A. Hassanein, M.C. Phillips, Expansion dynamics of ultrafast laser produced plasmas in the presence of ambient argon, J Appl Phys. 116 (2014) 133301. https://doi.org/10.1063/1.4896169.

[18] T. Donnelly, M. Mazoyer, A. Lynch, G. O'Sullivan, F. O'Reilly, P. Dunne, T. Cummins, CO2 laser pulse shortening by laser ablation of a metal target, Review of Scientific Instruments. 83 (2012) 035102. https://doi.org/10.1063/1.3690066.

Chapter 3

Processing and characterization techniques

This chapter will briefly describe the main processing characterization techniques developed in the measurement of 2D WS_2 nanosheet thin film, outlining their working principles and their relation to the studies carried out in this thesis.

3.1 Scanning electron microscopy

Scanning electron microscopy (SEM) uses a focused electron beam to generate a variety of two-dimensional images by scanning the surface of a sample (Figure 3.1). It also provides millimeters to nanometer-scale imaging with high magnification and resolution by analyzing selected point locations.

The working principle of SEM is that a high-energy electron beam is accelerated at high voltage, which is typically 1-10 kV, and penetrates the sample surface to a depth of around 1 μm, resulting in signals that can be used to reveal information about the surface topography, orientation, and crystalline structure with higher spatial resolution than optical microscopy. Collected data over a selected region contains an overview of the entire material volume. The most common mode in SEM analysis is secondary electrons emitted by atoms excited by the electron beam with energies < 50 eV, which allows imaging of the surface structures from which they originate. This is because the low-energy electrons can only escape from a thin layer near the sample's surface. It is also important to note that non-conductive materials such as organic residues are transparent to electrons due to their weak interaction with the primary beam, i.e., without an

appreciable scattering of light, so they may not appear at all in SEM. If these materials are in higher quantities such as in low-conductivity substrates, such charging-induced imaging instability could be of tolerance, particularly at higher voltages where atomic structure imaging at high resolution is attempted to map.

On the other hand, SEM can be used to identify phases in the qualitative chemical analysis due to the generation of X-ray photons in the samples by the electron beam. Displacement of core-level electrons alters the chemical environment due to transitions of valence electrons to the vacancy shell, generating the emission of an X-ray of characteristic energy, which is particularly useful for qualitatively determining chemical compositions using Energy Dispersive X-Ray Spectroscopy (EDS or EDX).

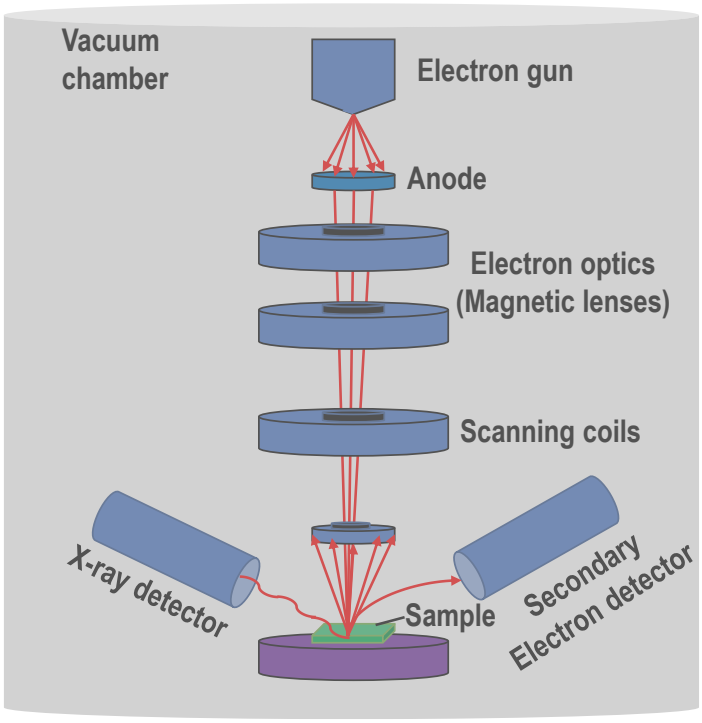

Figure 3. 1 Schematic diagram of scanning electron microscope (SEM).

3.2 Raman spectroscopy

Raman spectroscopy is a spectroscopic technique typically based on inelastic scattering of incident light through the excitation of vibrational modes of solids or molecules when photons gain or lose energy by absorbing or exciting phonons. Rayleigh scattering is the predominantly elastic scattering of light, which naturally affects the number of photons transmitted or reflected. Instead, the Raman effect is far less probable because it affects only about 1 in 107 photons, but modifies their energy by molecular vibration in the material. This is due to an incident photon stimulating a system from the ground state to an excited virtual state, followed by relaxation to a higher vibrational level of the ground state, which results in the scattering of a photon with some reduction in energy due to the difference between the ground and vibrational state, as shown in Figure 3.2. This behavior increases the energy of the molecules, resulting in scattered photons being redshifted, which is known as Stokes-Raman scattering. If a system is in an excited vibrational state, it transfers energy to the photons through a virtual state, by relaxing into the ground state, causing the spectrum of the scattered light to be blueshifted and is known as anti-Stokes Raman scattering, which essentially occurs at a reduced intensity due to the smallest number of molecules in the excited vibrational state at a given instant of time.

In addition, since the vibrational modes of molecules are characterized by their well-defined energy states related to the distortion of the bonds between lattice atoms, Raman scattering has resulted in an optical process where incoming excitation light interacting with nanoparticles and molecules can be identified by

vibrational signatures. The Raman spectrometer typically consists of an optical microscope to visually identify samples at high magnification using visible wavelength laser excitation (Figure 3.3), with a certain bandwidth, capable of providing high spectral resolution [1]. Raman scattered light is usually collected and either dispersed by a spectrograph or interferometer using interference patterns [2]. Raman spectrometers also use charge-coupled devices (CCD) or array detectors, which are suitable for the analysis of different wavelength ranges, since they are extremely sensitive to light [3]. It is often necessary to separate the Raman scattering from the Rayleigh scattering signal and reflected laser signal to collect the highest quality Raman spectra using a laser rejection filter to attenuate the scattered energy reaching the detector. The measured spectrum is identified as a function of Raman shift, which is the difference between excitation and scattering wavenumbers associated with well-known modes for material identification and analysis.

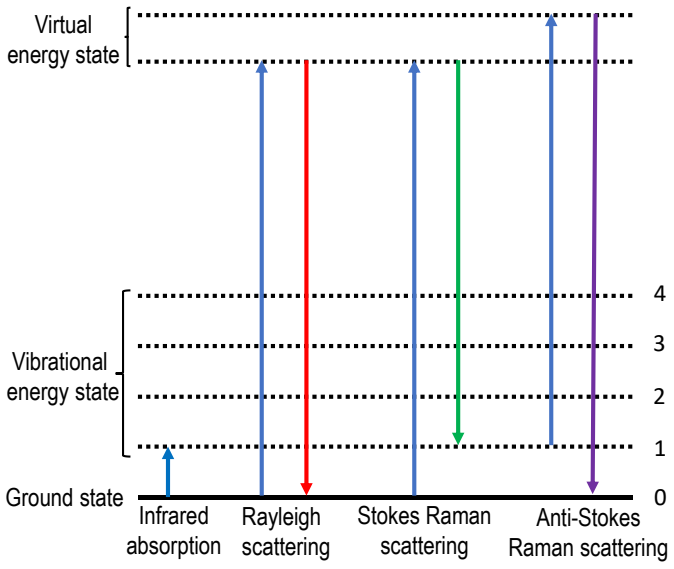

Figure 3. 2 Energy level diagram involved in Raman spectroscopy.

2D materials are usually Raman active, and intensities and frequencies of their vibrational modes are particularly sensitive to the number of layers and lateral size of sub-micrometers to a few micrometers due to interlayer coupling. In this sense, Raman spectroscopy was used for exfoliated 2D WS_2 nanosheets to analyze the chemical structure, phase, and crystallinity in a wide distribution of size and thickness compared to commercial WS_2 nanopowder [4-6]. Thus, providing detailed information on their impact on the electrical properties of materials when characterizing them.

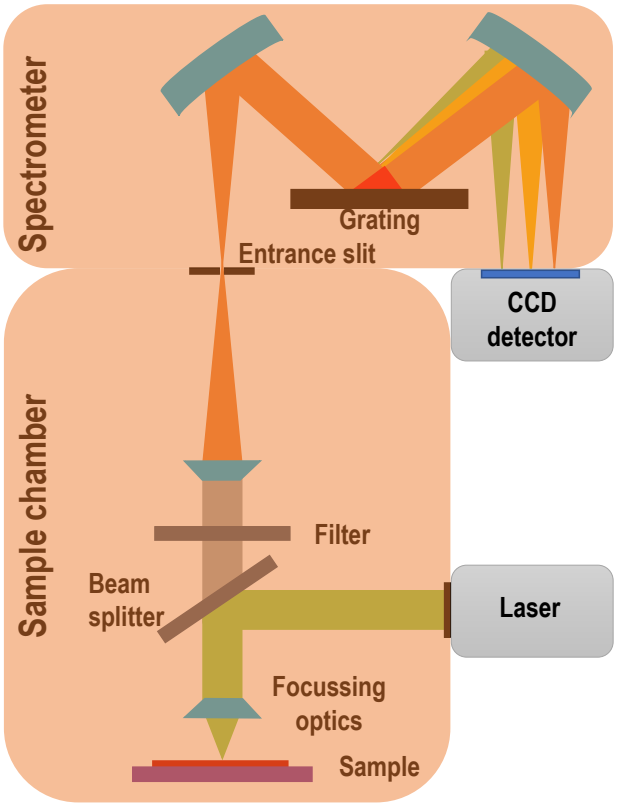

Figure 3. 3 Schematic diagram of dispersive Raman spectroscopy setup.

3.3 X-ray diffraction

X-ray diffraction (XRD) is a technique used for determining the atomic and molecular structure of a crystal when an incident X-ray beam is diffracted into many specific directions. By measuring the diffraction angles and intensities of these beams, a crystallographer can produce a three-dimensional representation of the electron density picture within the crystal [7]. Thereby determining the positions of the atoms, chemical bonds, crystallographic disorder, and other information surrounding the material.

In single-crystal X-ray diffraction, it is mounted a goniometer to position the crystal at selected orientations. By illuminating a monochromatic beam of X-rays onto the crystal, a diffraction pattern of spaced-apart spots is produced, called reflections. These are collected as two-dimensional images in different orientations by an area detector, which is then converted into a three-dimensional model of the electron density map within the crystal using Fourier transform mathematical methods, combining with two or more chemical data known from the sample for atomic model reconstruction, as shown in Figure 3.4.

In all X-ray diffraction-based methods, the scattering of the atoms is elastic; the scattered beams maintain the same wavelength as the incoming beams. In contrast, inelastic X-ray scattering methods are used to study the excitation of the sample, rather than the distribution of its atoms [8].

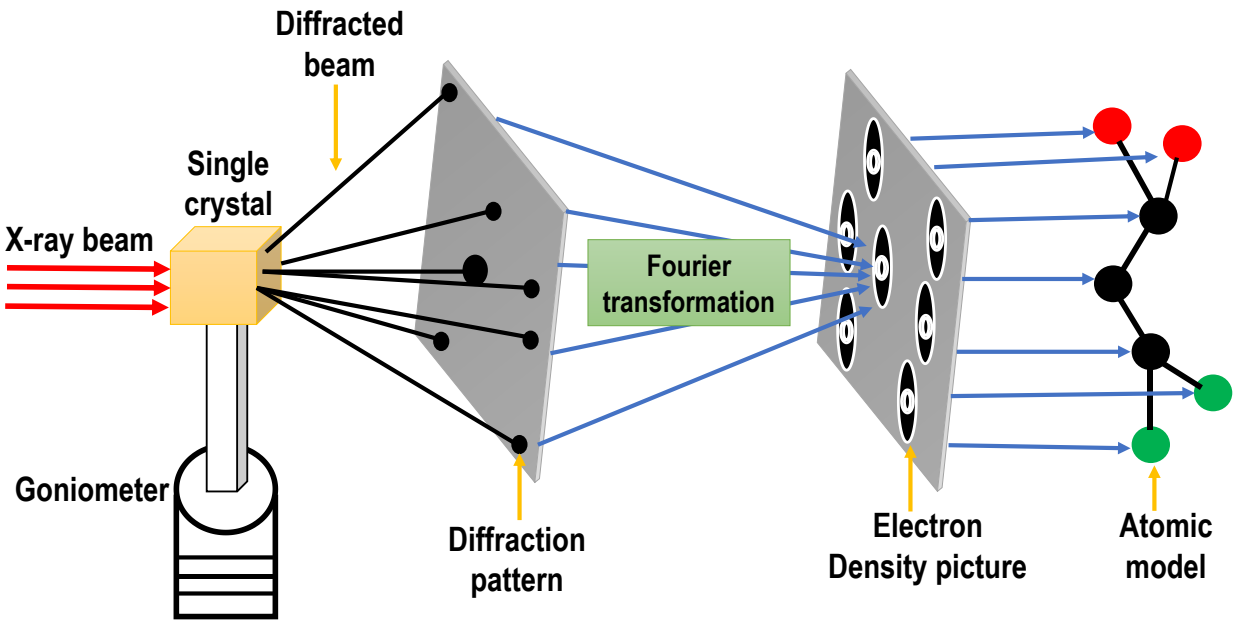

Figure 3. 4 Schematic diagram of X-ray diffraction (XRD).

Crystalline solids are periodic arrays of atoms, ions, or molecules with an interatomic spacing of about 1A. The wavelength of the incident X-ray should be on the same order of magnitude as the spacing of atoms. This allows the atoms to scatter X-ray waves through the electron cloud surrounding the atoms and emit secondary spherical waves originating from the electron (scatterer). This effect is particularly known as elastic scattering since the energy of the scattered wave is conserved. In this sense, a regular array of scatterers produces a regular array of spherical waves that are destructive in most directions (the reflected waves cancel each other out), but in some cases constructive [9]. However, these add constructively in a few directions following Bragg's law:

$$n\lambda = 2dsin\theta \tag{3.1}$$

where d is the distance between diffracting planes, θ is the angle of incidence, n is the order of reflection, and λ is the wavelength of the X-ray source. These specific directions appear as bright spots on the diffraction pattern known as reflections. X-ray diffraction occurs when an electromagnetic wave interacts with a periodic atomic structure or a regular array of scatterers whose repeat distance is about the same as the wavelength of the beam, allowing us to predict the angles at which X-rays are diffracted by the material, as shown in Figure 3.5. Thus, the diffracted beam must be in phase to emit a signal. Only angles that satisfy the following condition will register:

$$sin\theta = \frac{n\lambda}{2d} \tag{3.2}$$

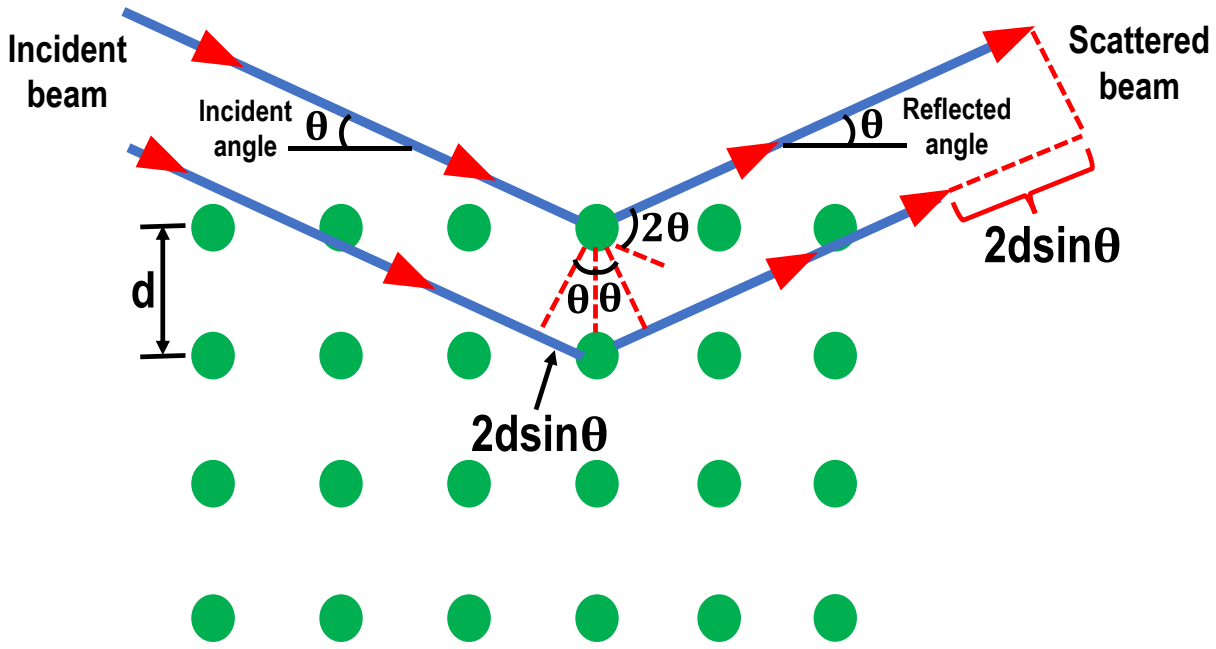

Figure 3. 5 Schematic representation of Bragg's law.

3.3.1 Crystal structures

A crystal structure is a periodic arrangement of the unit cell into a lattice (Figure 3.6(a)). The unit cell contains a single atom or atoms with the smallest unit of volume with identical symmetries, which stack together in all directions to construct the entire crystal lattice, as shown in Figure 3.6(b). Thus, a crystal consists of planes of symmetrically organized atoms that are spaced a distance d apart but can be separated into some atomic planes, each of different spaces.

The lengths a, b, and c and the angles α, β and γ are lattice constants or parameters that can be precisely determined by XRD, allowing us to know the structure of crystalline sample and molecular formula of the crystalline compound.

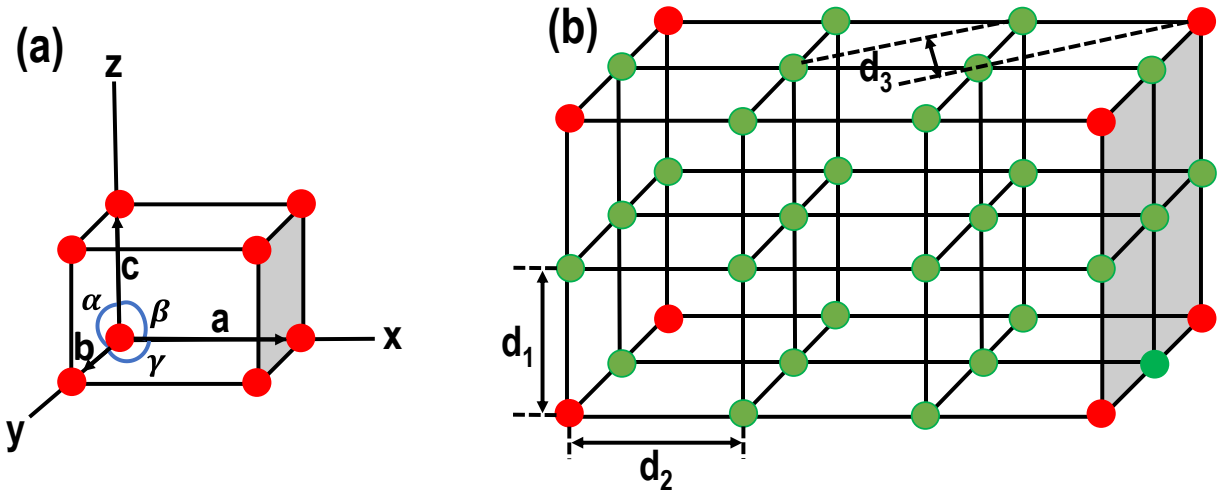

Figure 3. 6 (a) Unit cell and **(b)** crystal lattice.

3.3.2 Seven crystal systems

Table 3.1 shows seven crystal systems that describe all the ways in which rotational axes of symmetry are combined to construct simple 3-dimensional

lattices. These crystals are cubic, tetragonal, hexagonal, rhombohedral, orthorhombic, monoclinic, and triclinic.

Table 3. 1 Seven crystal systems.

Crystal class	Axis system
Cubic	$\boldsymbol{a = b = c,\ \alpha = \beta = \gamma = 90°}$
Tetragonal	$\boldsymbol{a = b \neq c,\ \alpha = \beta = \gamma = 90°}$
Hexagonal	$\boldsymbol{a = b \neq c,\ \alpha = \beta = 90°, \gamma = 120°}$
Rhombohedral	$\boldsymbol{a = b = c,\ \alpha = \beta = \gamma \neq 90°}$
Orthorhombic	$\boldsymbol{a \neq b \neq c,\ \alpha = \beta = \gamma = 90°}$
Monoclinic	$\boldsymbol{a \neq b \neq c,\ \alpha = \gamma = 90°, \beta \neq 90°}$
Triclinic	$\boldsymbol{a \neq b \neq c,\ \alpha \neq \beta \neq \gamma \neq 90°}$

3.3.2 Miller Indices

There are two ways to define the Miller indices [10]. Considering as a point in the reciprocal lattice or determining the inverse intercepts through the lattice vectors. In either case, the direct lattice vectors $\mathbf{a_1}$, $\mathbf{a_2}$, and $\mathbf{a_3}$ that define the unit cell are chosen. Then, the reciprocal lattice vectors normal to the direct lattice planes are also determined, denoted by $\boldsymbol{b_1}$, $\boldsymbol{b_2}$, and $\boldsymbol{b_3}$.

The Miller indices (hkl) are planes orthogonal to the reciprocal lattice vector defined by

$$\boldsymbol{g}_{hkl} = h\boldsymbol{b_1} + k\boldsymbol{b_2} + l\boldsymbol{b_3} \tag{3.3}$$

where (hkl) indicates a normal to the family of lattice planes in the basis of the reciprocal lattice vectors. Also, the plane (hkl) denotes fractional intercepts of the points a_1/h, a_2/k, and a_3/ℓ, as shown in Figure 3.7(a). Thus, the Miller indices result from the inverses of the intercepts of the plane, based on the lattice vectors, representing the edges of a unit of a lattice. If the crystal plane is parallel to one of the axes, the intersect is at infinity, so one of the indices $^1/_\infty$, or zero. For example, in Figure 3.7(b), the axial lengths are 4Å, 8Å, 3Å, and the intercept lengths are Å, 4Å, 3Å. The fractional intercepts of these two lengths turn out to be 1⁄2, 1⁄2, 1; and the Miller index of the plane is (221), respectively. The analysis for the plane (100) is performed similarly, with the only difference being that the intersections of the planes in the **b** and **c** directions are at infinities.

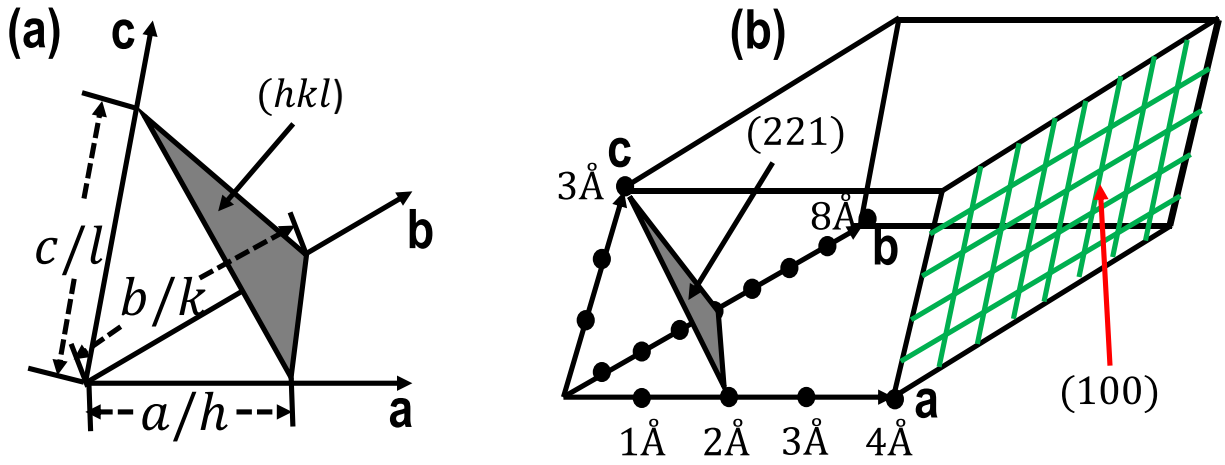

Figure 3. 7 Miller indices of **(a)** the reciprocal lattice of the fractional intercepts of the a/h, b/k, and c/l axes. **(b)** Describes the family of planes with Miller indices (221) and (100).

To measure the perpendicular d-spacing between adjacent lattice (hkl) planes is related to the nearest neighbor distance of the reciprocal lattice vector orthogonal to the planes (Figure 3.8), by the following formula:

$$d = \frac{2\pi}{|\boldsymbol{g}_{hkl}|} \tag{3.4}$$

It should be noted that the notation $[hk\ell]$ describes the direction: $h\boldsymbol{a_1} + k\boldsymbol{a_2} + l\boldsymbol{a_3}$. This is the representation of the direct lattice basis, which is not necessarily normal to the (hkl) planes, except in a simple cubic lattice, where the lattice vectors are orthogonal and of equal magnitudes, denoted by a. Therefore, the Miller indices $(hk\ell)$ and $[hk\ell]$ only represent normal/directions in a three-dimension cartesian coordinates system, as shown in Figure 3.9.

$$d = \frac{a}{\sqrt{h^2 + k^2 + l^2}} \tag{3.5}$$

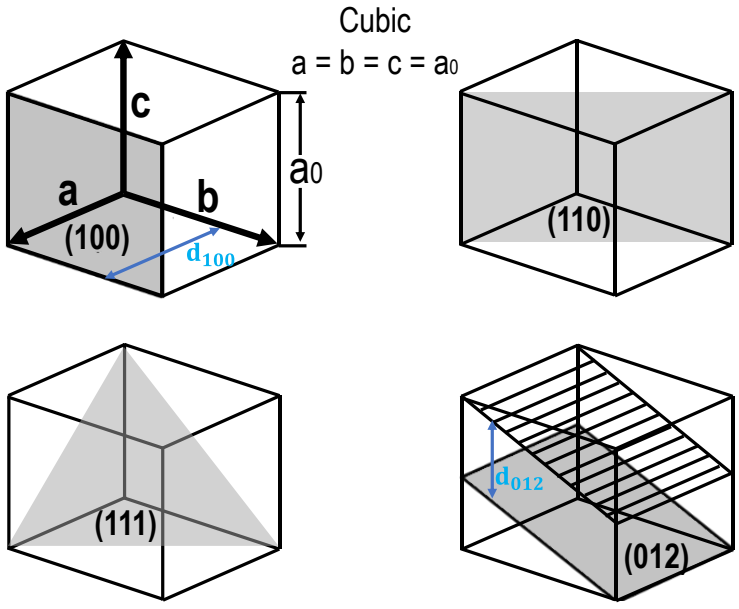

Figure 3. 8 Miller indices of atomic planes and their d-spacings in a simple cubic.

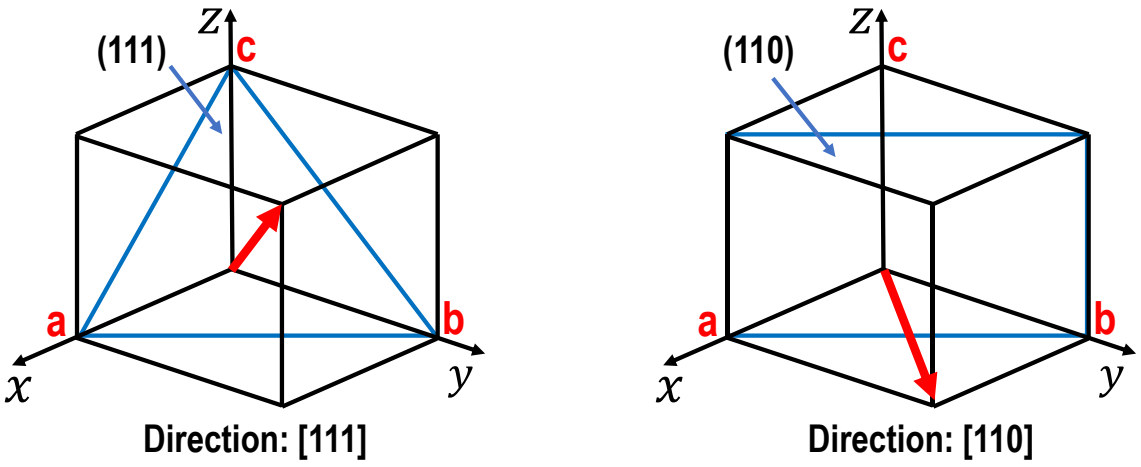

Figure 3. 9 Indexing of planes and directions.

In the case of hexagonal and rhombohedral lattice crystals, directions and planes are designated by the four indices $(hkil)$ as established in the Bravais-Miller systems, which obey the constraint.

$$h + k + i = 0$$

where h, k, and ℓ are identical to the Miller indices, and i is a redundant index. For example, the notation (110) ≡ (1120) and (120) ≡ (1210) is more apparent when the indices have redundant information, as these point in three directions. Figure 3.10 shows that the (001) plane remains unchanged in a rotation of 2π/3 rad or 120°, while the [100], [010], and [110] crystallographic direction vectors are similar. If the notation S indicates the intercept of the plane with the [110] axis, then $i = 1/S$.

On the other hand, in a hexagonal lattice system, the interplanar distance is calculated in the form:

$$d = \frac{a}{\sqrt{\frac{4}{3}(h^2 + k^2 + hk) + \frac{a^2}{c^2}l^2}} \tag{3.6}$$

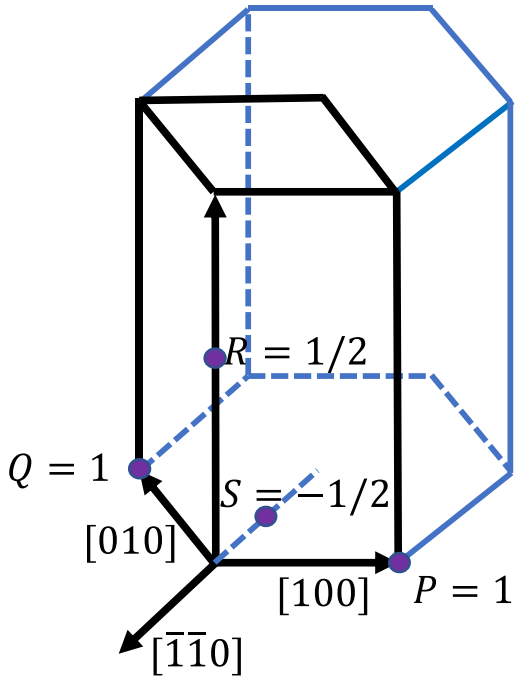

Figure 3. 10 Miller-Bravais indices of hexagonal structure.

3.4 UV-Visible spectrophotometer

UV–visible spectrophotometry (UV/Vis) is a technique for measuring light absorbance based on frequencies or wavelengths in the ultraviolet and visible regions of the electromagnetic spectrum. Absorption wavelengths normally range from 200 to 700 nm and are widely used in diverse applications such as in the analysis of organic compounds [11], biological chemicals, proteins [12], paintings, manuscripts, textiles, etc [13]. The only condition is that the sample absorbs in the UV/Vis region, where the energy difference between two separate molecular orbitals is mainly in the visible spectrum range.

The spectrophotometer consists of a monochromator that contains an entrance slit to direct white light to a dispersive element that separates the colors of light. This also has a mechanism for directing the selected color to the exit slit, which focuses monochromatic light onto the solution for subsequent analysis in the detector, as shown in Figure 3.11. When light strikes the sample, generates an increase in the energy of the molecules or atoms that compose them. The absorbed radiation excites the electrons from the ground state to another higher energy state. This allows the formation of an absorption line, many of which form an absorption spectrum, which in particular appears as a pattern of dark lines. The incident light (monochromatic light) of a UV-visible spectrophotometer is between the ultraviolet range (185-400 nm) and visible range (400-700 nm) of the electromagnetic spectrum. The rotating slit of the device selects a specific wavelength of light with sufficient energy to allow electrons to attain a higher energy state when excited. The fraction of incident radiation absorbed results in the formation of the absorption spectrum, which is measured in terms of absorbance, also known as optical density (OD), which is the quantity of light absorbed by a solution. This process depends on the number of excited electrons in the ground state, as well as on the concentration of molecules in the sample. Likewise, the plot of absorbance (A) versus wavelength (λ) produces the spectrum, which helps identify an unknown compound. For example, the more easily the electrons are excited, the longer the wavelength of light that the compound absorbs.

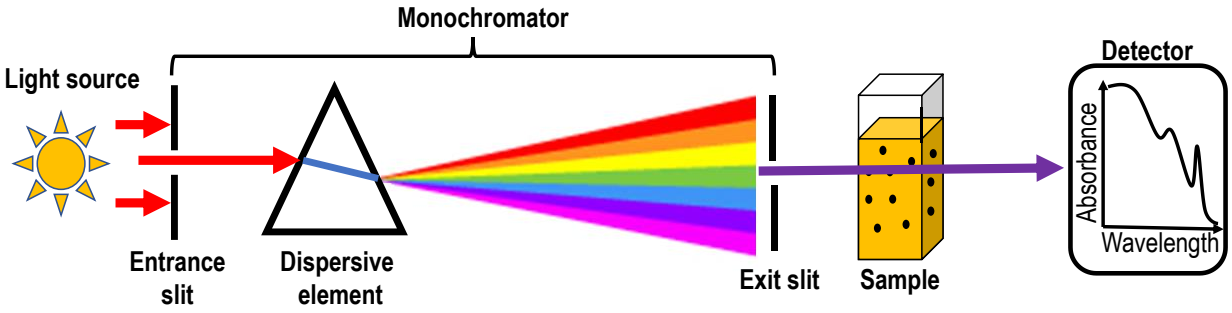

Figure 3.11 UV–visible spectrophotometry (UV/Vis).

Figure 3.12 shows four possible types of electronic interactions or transitions that can be considered. These are π–π*, n–π*, σ–σ*, and n–σ*. The order of these interactions is classified according to the energy, these are: σ–σ* > n–σ* > π–π* > n–π*. Thus, the spectrum arises because of the electron transition in a molecule when they are excited from a lower energy level to a higher energy level. Since the σ–σ* and n–σ* transitions need larger energy to take place, most absorption organic compounds are not based on these transitions but on π–π* y n–π* transitions. This is due to the absorption peaks falling in an experimentally determined region of the spectrum (200 - 700 nm).

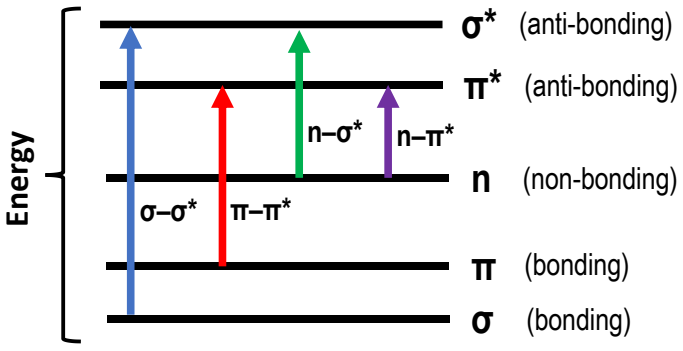

Figure 3. 12 Possible types of electronic transitions in UV-visible spectrophotometer analysis.

3.5 References

[1] P. Kukura, D.W. McCamant, R.A. Mathies, Femtosecond Stimulated Raman Spectroscopy,Http://Dx.Doi.Org/10.1146/Annurev.Physchem.58.032806.104456. 58 (2007) 461–488. https://doi.org/10.1146/ANNUREV.PHYSCHEM.58.032806.104456.

[2] B.H. Bunch, A. Hellemans, The timetables of technology : a chronology of the most important people and events in the history of technology, (1993) 490.

[3] M.J. Pelletier, C.C. Pelletier, RAMAN SPECTROSCOPY | Instrumentation, Encyclopedia of Analytical Science: Second Edition. (2005) 94–104. https://doi.org/10.1016/B0-12-369397-7/00529-X.

[4] A.C. Ferrari, J.C. Meyer, V. Scardaci, C. Casiraghi, M. Lazzeri, F. Mauri, S. Piscanec, D. Jiang, K.S. Novoselov, S. Roth, A.K. Geim, Raman spectrum of graphene and graphene layers, Phys Rev Lett. 97 (2006) 187401. https://doi.org/10.1103/PHYSREVLETT.97.187401/FIGURES/3/MEDIUM.

[5] C. Backes, B.M. Szydłowska, A. Harvey, S. Yuan, V. Vega-Mayoral, B.R. Davies, P.L. Zhao, D. Hanlon, E.J.G. Santos, M.I. Katsnelson, W.J. Blau, C. Gadermaier, J.N. Coleman, Production of highly monolayer enriched dispersions of liquid-exfoliated nanosheets by liquid cascade centrifugation, ACS Nano. 10 (2016) 1589–1601. https://doi.org/10.1021/ACSNANO.5B07228/ASSET/IMAGES/NN-2015-07228X_M011.GIF.

[6] C. Backes, K.R. Paton, D. Hanlon, S. Yuan, M.I. Katsnelson, J. Houston, R.J. Smith, D. McCloskey, J.F. Donegan, J.N. Coleman, Spectroscopic metrics allow in situ measurement of mean size and thickness of liquid-exfoliated few-layer graphene nanosheets, Nanoscale. 8 (2016) 4311–4323. https://doi.org/10.1039/C5NR08047A.

[7] L.F. Bermejo, Crystallography Made Crystal Clear, (n.d.). https://www.academia.edu/40916922/Crystallography_Made_Crystal_Clear (accessed August 23, 2022).

[8] W. Schuelke, Electron Dynamics by Inelastic X-Ray Scattering (Oxford Series on Synchrotron Radiation), (2007). http://www.amazon.com/exec/obidos/redirect?tag=citeulike07-20&path=ASIN/0198510179 (accessed August 23, 2022).

[9] D.A. Skoog, F.J. Holler, S.R. Crouch, Principles of instrumental analysis, Published in 2007 in Belmont Calif) by Thomson Brooks/Cole. (2007). https://lib.ugent.be/catalog/rug01:001256198 (accessed August 23, 2022).

[10] hajir muhajir, Introduction to Solid State Physics, 8th Edition Charles Kittel, (n.d.). https://www.academia.edu/33545480/Introduction_to_Solid_ State _Physics_8th_Edition_Charles_Kittel (accessed August 23, 2022).

[11] A.M. Mohammed, UV-Visible Spectrophotometric Method and Validation of Organic Compounds, European Journal of Engineering Research and Science. 3 (2018) 8. https://doi.org/10.24018/EJERS.2018.3.3.622.

[12] V.F. Kalb, R.W. Bernlohr, A new spectrophotometric assay for protein in cell extracts, Anal Biochem. 82 (1977) 362–371. https://doi.org/10.1016/0003-2697(77)90173-7.

[13] M. Picollo, M. Aceto, T. Vitorino, UV-Vis spectroscopy, Physical Sciences Reviews. 4 (2019). https://doi.org/10.1515/PSR-2018-0008/MACHINEREADABLECITATION/RIS.

Chapter 4

Fabrication and application of two-dimensional tungsten disulfide nanosheets for self-powered photodetectors in the visible spectrum

2D WS_2 nanosheets are considered promising materials for highly sensitive self-powered photodetectors based on Au/WS_2/Au lateral contact. Its favorable bandgap and atomically thin profile have allowed for outstanding achievements with novel applications due to their semiconducting properties, large absorption coefficient, sensitivity to interlayer interactions, and tunable bandgaps ranging from 1.4 to 2.1 eV according to the number of layers, which are fundamental properties of semiconductors that regulate many electronic device characteristics. In addition, the material exhibits some particularly interesting properties, such as high charge carrier mobility, high switching speed, and high photon absorption in a wide range of spectra [1,2], making it a promising candidate for next-generation photovoltaic technology [3]. Y. Gao et al. [4] indicated that WS_2 nanosheets can be used for ultrashort pulse generation and a wide spectral range optical absorber, ranging from 450 to 700 nm. This implies huge applications including broadband saturable absorbers, photoluminescence, optical computer, biomedical imaging, communications, optically filtered detectors, and so on.

In this investigation, we showed a self-powered photodetector based on Au/WS_2/Au junctions, in which the responsivity reached 0.12 mA/W at 640 nm light illumination with 5.2 mW/cm^2 at a bias of 0 V. Instead, the R_λ was 12.74 mA/W at 640 nm with an intensity of 4.1 mW/cm^2 and at a bias of 2 V, respectively. Y.J. Yoon

et al. [5,6] developed the direct WS_2 photodetector fabrication on a flexible substrate; the WS_2 film was less deficient in S, with an S/W ratio of 1.83, while the most deficient was 1.76. R_λ value was 0.53 mA/W at 635 nm with an intensity of 10.7 mW/cm^2 at a bias voltage of 10 V. Thus, S/W ratios are higher than our bulk material and even higher than exfoliated nanosheets, which also explains the need to apply a high bias. K. Huang et al. [7] also obtained an R_λ of 4.04 mA/W at 532 nm with an intensity of 59.09 mW/cm^2 at a bias of 5 V for a flexible broadband photodetector based on WS_2 nanosheets. The device exhibits a lower electrical output per photon input than our prototype over the entire visible spectrum.

Since our device presented an excellent photoresponse to the mere action of light without the addition of an external power supply. It was discovered that the WS_2 film could activate the broader optical spectrum than the visible range, which makes it more attractive for applications of solar cells and broadband photodetectors (PDs). Xu et al. [8] studied oxygen-incorporated and layer-by-layer stacked WS_2 nanosheets for broadband and found that the photodetector is still sensitive at a wavelength in the NIR region (1100–2000 nm). These discoveries suggest great potential for future applications. Z. Wang et al. [9] also investigated a flexible self-powered photoelectrochemical-type photodetector based on 2D WS_2-graphene heterojunction, recording a photocurrent density of 1.4 μA/cm^2 at an illumination intensity of 30 mW/cm^2. This Promotes the rapid migration of carriers and enhances the optical response of TMDs.

4.1 Structural analyses of 2D WS_2 nanosheets

In the fabrication of the 2D nanostructures, several methods have been used to obtain the WS_2 thin films on SiO_2/Si substrates. The most common TMDs were synthesized by chemical vapor deposition (CVD) [10], Magnetron Sputtering [11], Pulsed-Laser Deposition (PLD) [12], and sulfurization of metal films [13,14]. However, the liquid exfoliation method seems to be the most effective, particularly for quickly obtaining nanomaterials for light sensing applications, where a large quantity of 2D nanosheets with inherent defects are favorable for high carrier mobility. M. Terrones et al. [15] showed that chemical exfoliation methods have a scalability advantage over CVD. The challenge is to achieve the intercalation of bulk layered materials followed by efficient exfoliation without damaging the sheets. T.D. Anthopoulos et al. [16] informed that liquid-phase exfoliation of WS_2 yielded high-concentration suspensions, where the extracted 2D nanosheets exhibited high structural and stoichiometric quality. This behavior is related to structural defects and strongly influences their optical properties.

As described in synthesis methods, 2D WS_2 nanosheets were obtained via liquid phase exfoliation with a large number of randomly orientated sheets in a solvent mixture. The spin coating technique was used to successfully produce thin films with a uniform thickness of about 52 nm on a 1x1 cm^2 SiO_2/Si substrate. Every single plane of WS_2 is composed of a two-dimensional structure with tungsten atoms positioned between two layers of sulfur atoms in trigonal prismatic coordination, where the projection of sheet WS_2 (monolayer) onto the plane exhibits a clear hexagonal honeycomb structure. In addition, each 2D WS_2

nanosheet is composed of stacked 2D WS_2 atomic layers with a wide distribution of monolayers per nanosheet, as shown in Figure 4.1. Thus, to describe the properties of the crystal structure of nanosheets, various features of the sample are explored, such as surface morphology, chemical composition, crystallinity, and absorbance, using SEM, EDX, Raman scattering, XRD, AFM, and UV/Vis techniques; outlining their relation with other previous studies carried out.

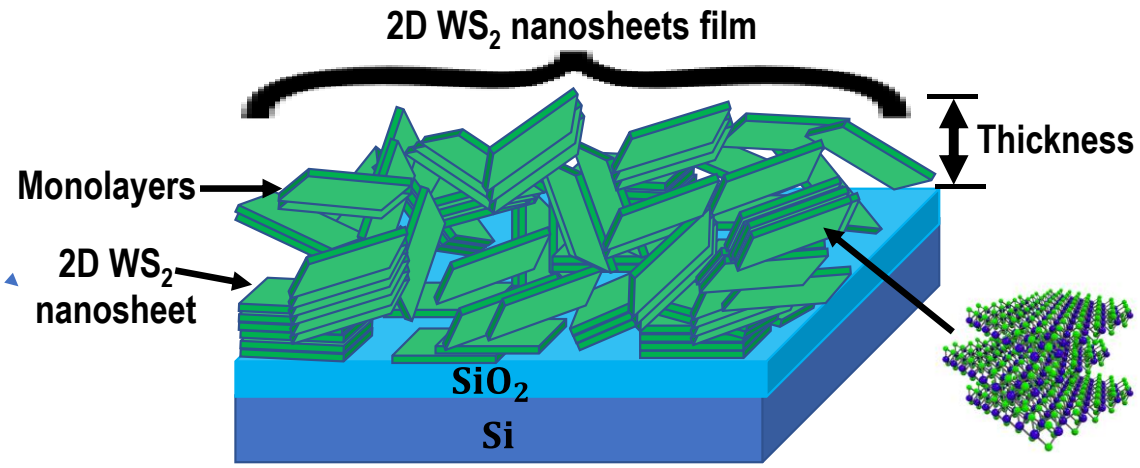

Figure 4. 1 Illustration of 2D WS_2 nanosheets on a SiO_2/Si substrate.

4.2 Scanning Electron Microscopy (SEM) with EDX Analysis

Figure 4.2(a) shows the SEM image of the bulk WS_2 nanopowder precursor of a density of 7.5 g/mL with 99% trace metal basis and a 90 nm average part size. SEM did not provide a clear image of the surface topography of the thick sheet structures at the 5-μm scale but may show smaller powder particle sizes. Instead, on the 1 μm and 100 nm scales (Figures 4.2(b) and (c)), the bulk material exhibits several thick hexagonal sheets of different diameters ranging from 40 to 80 nm. These conditions are favorable for obtaining a thinner layer when separating the

nanosheets. After ultrasonic exfoliating, a large amount of flexible 2D nanosheets is visible as shown in Figure 4.2(d), which is characteristic of multilayer thin films. In particular, the asymmetric growth of the nanosheets could be due to the weak interlayer coupling and the non-uniform size of the bulk sample. In addition, the horizontal and vertical orientation in certain substrate regions is partly attributed to the compression and extrusion between nanosheets with an average width smaller than nanopowder. X. Zhang et al. [17] reported nanosheet thicknesses in the order of 6 nm and spacing between single sheets of about 0.64 nm, corresponding to two adjacent (002) basal planes of WS_2. These values can range from 0.62 to 0.65 nm according to the number of stacking layers in the mechanical exfoliation. Since the morphology of the nanosheets is similar to that of Zhao, we can attribute that the measurement range is very close to that of our sample.

EDX analysis of bulk WS_2 precursor showed spatial distribution of elements through mapping, where the peak positions of each atomic structure were found in both the bulk material and the WS_2 thin film. The most intense sharp peaks of W and S have atomic percentages of 23.38 and 39.88, which gives an S/W ratio of 1.70, characteristics of the accurate composition of the bulk sample, as shown in Figure 4.3(a). After exfoliation, the atomic percentages of the elements in the WS_2 film were 1.85 and 2.49, respectively, and the S/W ratio was 1.34, which showed S atom deficiencies (Figure 4.3 (b)). We can verify that the S vacancies start in the mechanical exfoliation since the bulk material exhibits a higher S/W ratio than the dispersed nanosheets on the SiO_2/Si substrate.

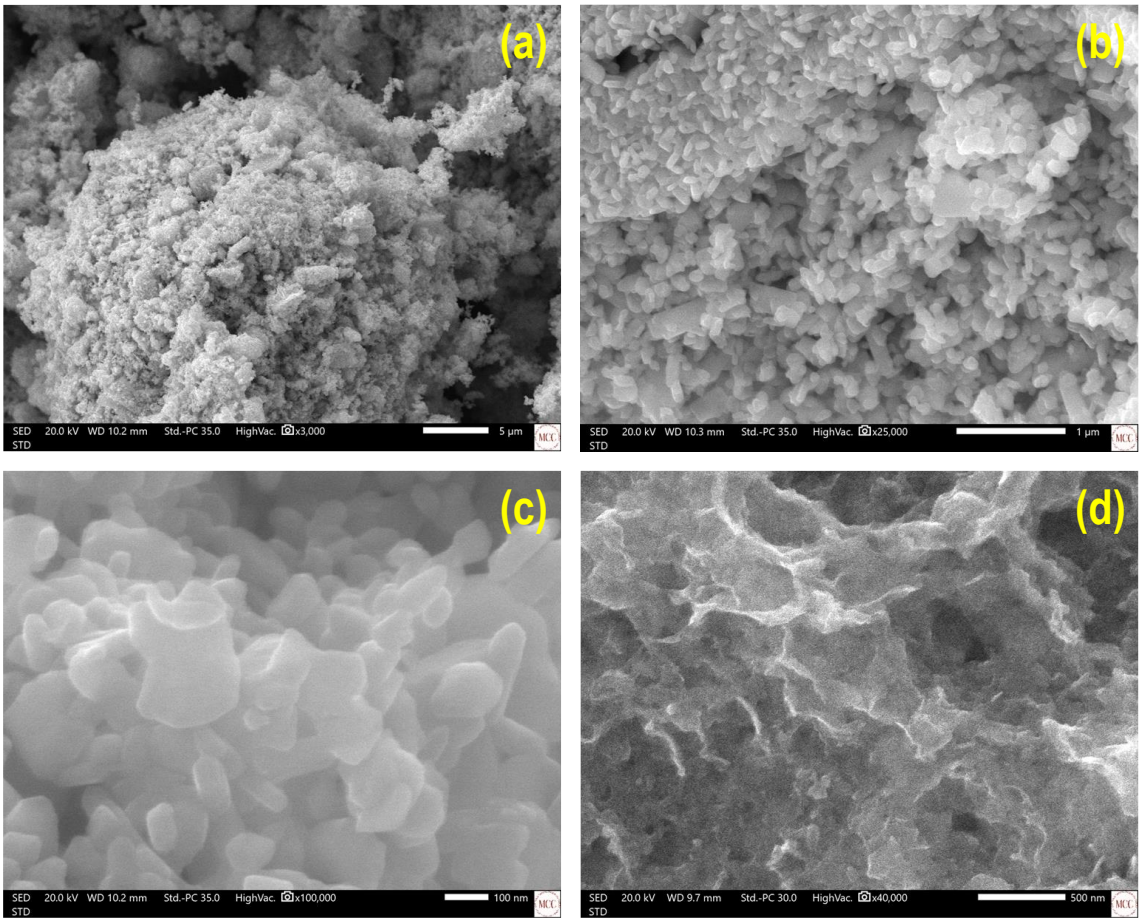

Figure 4.2 Scanning electron microscopy (SEM) images of the bulk WS_2 precursor on scales of **(a)** 5 µm, **(b)** 1 µm, and **(c)** 100 nm. **(d)** 2D WS_2 nanosheets on SiO_2/Si substrates after liquid-phase exfoliation.

The weak van der Waals interactions between WS_2 individual layers allow easy exfoliation of the bulk structure, affecting some ionic-covalent bonds at the edges of the WS_2 monolayer that generate structural defects, mainly S vacancies, which in turn are substituted by oxygen atoms so as not to create defect states in space or an optically accessible subgap state in the WS_2 crystal structure. Byeong-Kyu Lee et al. [18] also showed that S atoms substituted for oxygen atoms during the oxidation process did not change the morphology structure of WS_2, but only

the concentrations of the elements, which is consistent with the EDX results. But the chemisorbed oxygen can act as an electron receptor that alters the local intrinsic charge density, leading to recombination and optical properties changes. Previous studies by E. Stratakis et al. [19] demonstrated that chemisorbed oxygen, as well as physisorbed molecules (mainly O_2), affected the emission properties of exfoliated WS_2 single layers when sulfur was replaced by oxygen at the edges. These statements effectively support our analysis method on the mechanical exfoliation evolution of the bulk sample to the 2D WS_2 nanosheets.

S. Salehi and A. Saffarzadeh [20] studied that sulfur vacancies on the electronic structure of the monolayer induce a midgap band in the vicinity of the VBM, manifesting itself as defect states, which shift the Fermi level to the bottom of the conduction band due to unsaturated electrons in the Mo and W orbitals around the vacancy defect. This property suggests that the defect states induced by S vacancies in transition metal dichalcogenides can activate higher carrier mobility in the 2D WS_2 nanosheets and improve the photodetector's responsivity. A.K. Sharma et al. [21] observed a huge S deficiency in all WS_2 films deposited using the PLD technique. Where WS_2 film showed interesting linear and nonlinear optical properties, these arguments consolidate our assertions about the optical properties of S-deficient 2D WS_2 nanosheets.

On the other hand, EDX analysis of the atomic % of oxygen showed a relative increase from 2.07 to 5.05 % after the exfoliation process. Since WS_2 has a two-dimensional structure with tungsten atoms positioned between two layers of sulfur atoms, the atomic % of W (1.85 %) is expected to be less than S (2.49 %).

If the sample is pure, the ratio of S and W must be 2 to 1, which is impossible under ambient conditions and even in vacuum environments due to the interstitial defects of the lattice in the film growth process. In addition, the atomic % of carbon in the bulk sample and the thin film was reported to be much higher than the rest of the elements, this usually happens when a thin layer of carbonaceous material is found on the air-exposed samples, which is generally known as adventitious carbon.

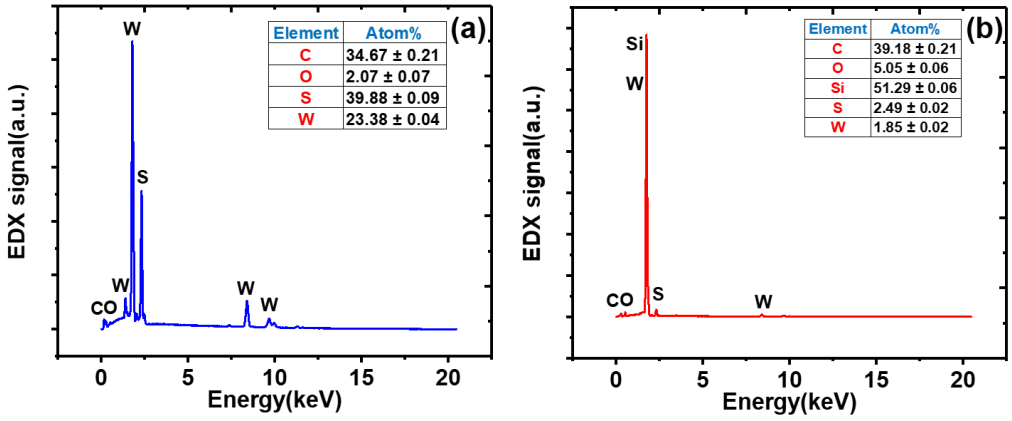

Figure 4. 3 EDX analyses of **(a)** bulk WS_2 precursor and **(b)** 2D WS_2 nanosheets after liquid exfoliation.

4.3 X-ray diffraction (XRD) patterns measurements

The nanosheets ' X-ray diffraction (XRD) patterns were compared with the commercial WS_2 nanopowder, as shown in Figure 4.4. The bulk WS_2 and the exfoliated products have a highly crystalline structure with the most intense and sharp peak at $2\theta = 14.15°$, corresponding to the (002) crystallographic plane consistent with the hexagonal phase WS_2 (2H-WS_2), as shown in Figure 4.4(a). However, nanosheets do not exhibit other peaks as in the bulk material ((004),

(100), (103), (106), (105), (110), and (112)); there is only the addition of the silicon peak due to the contact between the substrate and the sample, as shown in Figure 4.4(b). These absences confirm that the nanosheets were exfoliated along the (002) plane, leading to the enhanced intensity in XRD measurement preferentially orientated into substrates with the (002) basal plane parallel to the substrate. Compared with the intensity of bulk WS_2, those of the nanosheets were reduced by more than half. This is a consequence of the effective lateral size reduction and the high degree of delamination of the bulk sample in the exfoliation process. The obtained diffraction peaks indicated that the surface of the nanosheets did not show other impurities that could significantly affect the crystallinity and original structure of the sample. Another detail of the XRD pattern is the disappearance of planes (100) and (110), corresponding to the 33.34° and 58.52° angles. This proves that the number of stacked layers decreases significantly compared to the bulk WS_2, i.e., exfoliation-assisted nanosheets consist of few layers, which reduces energy states. Using Bragg's law, we calculated the interlayer distance at WS_2 film through relation $d = \frac{n\lambda}{2sin\theta}$, where λ is the wavelength of the x-ray source (λ = 1.54 Å), n is the order of reflection ($n = 1$), and θ is the angle of incidence in degrees of the plane (002). The interlayer spacing of 2D WS_2 nanosheets turns out to be ~ 0.6 nm, respectively. This value suggests that the stacked nanosheets are sturdily coupled due to the strong van der Waals interactions.

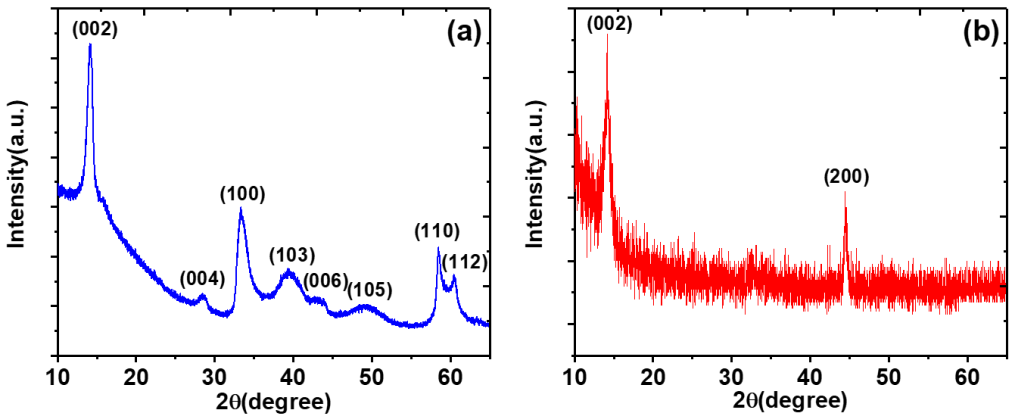

Figure 4. 4 X-ray diffraction (XRD) patterns of the **(a)** commercial WS_2 nanopowder and **(b)** nanosheets of the bulk sample after the exfoliation process.

4.4 Raman scattering measurements

Figure 4.5(a) shows the Raman spectra of bulk 2D WS_2 powder precursor. In this figure, bands belonging to W-S bonds at 349.05 and 414.60 cm^{-1} were identified. These bands correspond to the Raman active vibrational modes, assigned to the E^1_{2g} phonon mode of W+S movement in the *x-y* plane and the A_{1g} phonon mode of the S movement in the *z*-axis [22]. Raman spectra also revealed that crystalline WO_3 was formed in the dashed lines belonging at 696.21 and 804.42 cm^{-1}; the band at 696. 21 cm^{-1} is assigned to the O-W-O stretching vibration of $WO_3 \cdot nH_2O$, while the band at 804.42 cm^{-1} is attributed to the asymmetric stretching vibration of oxygen bridges (O-W-O) [23,24]. The WO_3 structure is formed by distorted corner shared WO_6 octahedrons extending in three dimensions. Accordingly, the peaks in the Raman spectrum are generated by the distortion of the $W0_3$ structure from the ideal octahedral arrangement of $Re0_3$

[25,26], where the distortion of each octahedron can lead to cubic, hexagonal, monoclinic, tetragonal, orthorhombic, and triclinic structures, respectively [27].

In 2D WS_2 nanosheets, neither crystalline nor amorphous WO_3 was formed. According to the results in Figure 4.5 (b), no signals of the displacement of crystalline WO_3 are shown, as attested by the absence of broad peaks illustrated in Figure 4.5 (a). The exfoliated nanosheets seem to considerably reduce bonds at cell edges of the bulk material so that the thin film surface also affects the electronic states that act as recombination sites and electrochemical corrosion. As a result, the O-W-O bands exhibit no orientations in basal planes perpendicular to the substrate surface. In contrast, only peaks are shown at 351.46 and 419.91 cm^{-1} belonging to the A_{1g} and E^1_{2g} vibrational modes. The peak at 519.64 cm^{-1} corresponds to the substrate (i.e., crystalline SiO_2/Si). In addition, the decrease in the number of layers results in the decreasing separation between E^1_{2g} and A_{1g} vibration modes, where 69.5 cm^{-1} is for bulk material and 68.45 cm^{-1} is for nanosheets. F. Wang et al. [28] showed the intensity of the photoluminescence peaks in WS_2 dropped significantly as the number of layers increased. This fact confirms that few-layer and multilayer films can absorb photons that excite electrons to a higher energy level in atoms, generating more recombination of photogenerated electron-hole pairs.

As the A_{1g} mode always has a stronger peak than that E^1_{2g} mode, A_{1g} can be used as a mechanism to trace the signature of mono, and a few layers in the TMD samples since the vibrational spectrum is sensitive to the number of layers. For example, as the WS_2 layer thickness increases, the A_{1g} mode intensity

increases due to the increase in S atoms. Since it rests on the separation between the short-range interatomic force constants, the weak interlayer interactions are dominant. Thus, the exchange of S atoms with the nearest layers is crucial in A_{1g}-mode changes to the interlayer coupling. Meanwhile, E^1_{2g} is attributed to the long-range Coulomb interactions with macroscopic electric fields acting in the shift in frequency between longitudinal optical (LO) and transverse optical phonons (TO) about the neighborhood of the Brillouin zone center. The origin of this LO-TO splitting can be understood most readily if one considers the arguments of P. Giannozzi et al. [29].

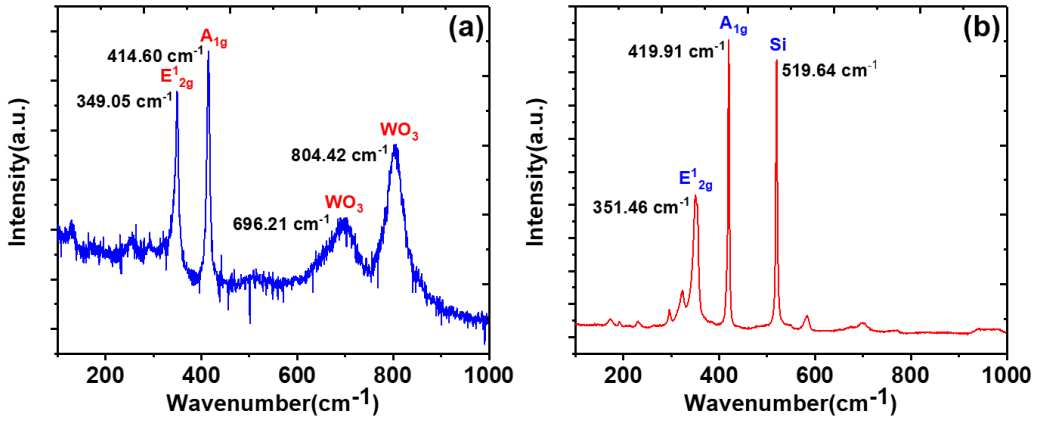

Figure 4. 5 Raman scattering spectrum of **(a)** bulk WS_2 precursor and **(b)** 2D WS_2 nanosheets after liquid exfoliation.

4.5 The optical absorbance spectra

Figure 4.6 shows the UV-visible absorption spectra of the 2D WS_2 nanosheets with A and B excitonic peaks at 634 nm and 528 nm corresponding to the direct transitions at the K point of the Brillouin zone in the 2H-WS_2 structure

(2H-phase trigonal prismatic). Instead, the C and D bands at 456 nm and 413 nm originate from inter-band transitions from the occupied dz^2 orbital below the Fermi level to the unoccupied d_{xy}, $d_{x^2-y^2}$ and $d_{xz,\ yz}$ orbitals in few-layered WS_2 nanosheets. Optical transitions between the density of states (DOS) in the valence and conduction bands, it is attributed to the transition from an indirect-to-direct bandgap. The origin of these transitions is attributed predominantly to the interlayer coupling effect or quantum confinement, which controls the bandgap evolution according to the spatial confinement of electron-hole pairs in one or more 2D WS_2 nanosheets. L. Zhang and A. Zunger [30] also suggested that the dominating physical factor on the layer thickness for all the MX_2 (M = Cr, Mo, W and X = S, Se, Te) was the quantum confinement effect, where the energy level of nanostructures increased as the result of increased kinetic energy when the size of nanostructures reduced. Electronic energy levels in this configuration are discrete, so the nanosheets' optical energy absorption is within allowed levels—these contrast with the excitonic energy levels and the optical absorption of light in the visible range. Thus, the photoluminescence energy of excitons helps us understand the evolution of the electronic structure as a function of the number of layers.

The band structure of bulk WS_2 has an indirect bandgap in the range 1.3 eV < ΔEg < 1.4 eV, and it increases as the number of stacked layers decreases until reaching a value of 2.05 eV, corresponding to the total density of states for the WS_2 monolayer, which is the direct bandgap at the K point of Brillouin zone [31,32]. In bulk, transitions A and B observed by absorption spectroscopy are direct optical transitions at K point and calculated as excitons A (1.95 eV) and B (2.35

eV), using the equation $E_g = \frac{hc}{\lambda}$, where E_g is the energy gap, h is the Plank's constant (6.6267 × 10^{-34} J.s), c is the speed of light (3.0 × 10^8 m/s), and λ is the wavelength of light. Thus, the UV-visible absorption spectrum data confirms the existence of a few-layer WS_2 film and is consistent with the previous analysis reported in the literature. The first peak at the long wavelength of 634 nm, corresponding to WS_2 nanosheets, has an optical bandgap of 1.95 eV, higher than the bulk sample value of about 1.35 eV. An increase in bandgap is a clear indication of quantum confinement among the stacked few layered. In addition, 1.95 eV < 2.05 eV, confirming that the binding energy of the monolayer WS_2 is higher than that of nanosheets. Therefore, exciton transition A allows us to identify the quality of the exfoliation and the optical absorption of the sample.

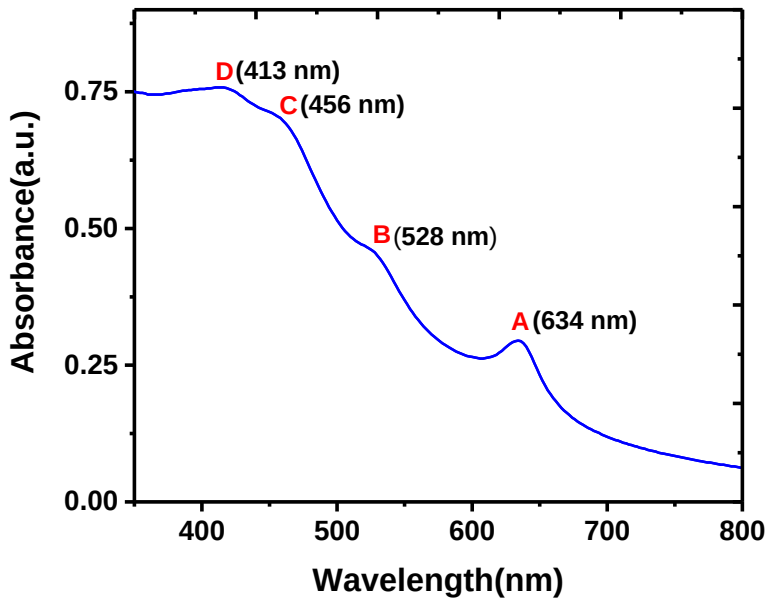

Figure 4. 6 UV-visible absorption spectra of the 2D WS_2 nanosheets.

4.6 Schematic bandgap alignment diagram in the carrier transport

On the one hand, in a back-to-back Schottky diode, it can be written as two different voltage drops on single diodes with forward and reverse bias [33,34]. Figure 4.7 shows the schematic energy band alignment diagrams for the case of two back-to-back Schottky diodes in Au/WS_2/Au contacts. Under dark conditions and without applying a bias voltage, the device exhibits a symmetric Schottky structure under the same vacuum level, as shown in Figure 4.7(a). Alignment of Fermi energy leads to the formation of band diagrams in the Au/WS_2 interface states. Since each Schottky barrier acts as a current rectifier, electrons can move from the semiconductor to metal and be controlled by two sides of the interface in equilibrium (constant barrier height) if there is no external effect on the system. However, electron-hole pairs are generated when an amount of voltage is supplied, creating the charge flow and voltage drops on single diodes, as shown in Figure 4.7(b). Electrons tend to move toward a positive bias because the voltage drop from V_2 ($V_2 < V_i$) induces a narrow depletion region (W_2) than V_1 ($V_1 > V_i$) with W_1, which changes the Schottky barrier height, as well as the direction and magnitude of the dark current. In addition, not all valence electrons become free electrons, so lattice defects trap some of them in the two-dimensional layers of the semiconductor. The increased external power supply will lower the barriers and extract more charge carriers from the trap states, thus increasing the net dark current due to a larger electric field.

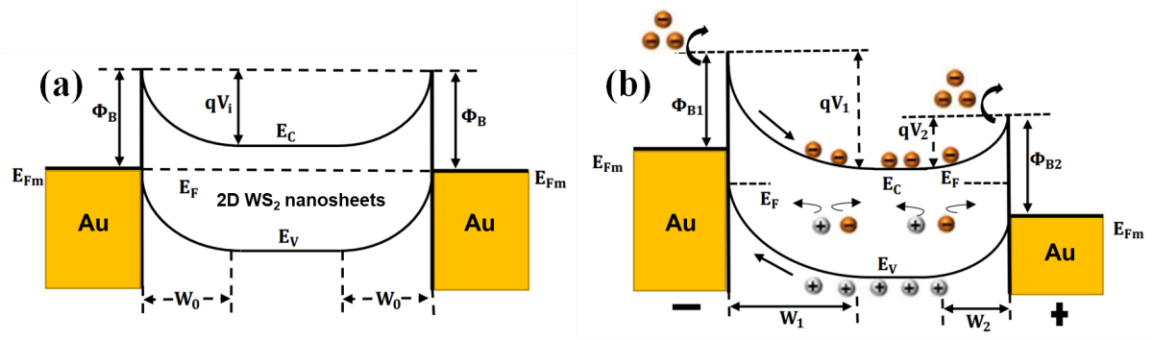

Figure 4. 7 Schematic energy band alignment diagrams for two Schottky barriers connected back-to-back **(a)** without and **(b)** with bias voltage.

Since the current through the diodes is the same, the diode equations can be expressed as

$$I = I_{s1}\left[\exp\left(\frac{qV_1}{\eta_1 k_B T}\right) - 1\right], \tag{4.1}$$

$$I = -I_{s2}\left[\exp\left(-\frac{qV_2}{\eta_2 k_B T}\right) - 1\right], \tag{4.2}$$

where V_1 and V_2 are the voltage drops on single diodes, k_B is the Boltzmann constant, η is the ideality factor, q is the electron charge, I_s is the leakage current, and T is the absolute temperature, respectively.

Under illumination and zero bias voltage, the barrier heights depend on the generation and recombination of photogenerated charge carriers when the photodetector device absorbs the light. The excitation of an electron or other charge carrier to a higher-energy state produces an electrical potential by the separation of charges by diffusion. Therefore, depending on the concentration of carriers in the metal-semiconductor junction, the photocurrent can take any direction, as shown in Figure 4.8(a). Instead, under bias voltage and illumination,

photogenerated charge carriers start distribution at metal/semiconductor interfaces. Depending on the charge accumulation process, the Schottky barrier height of the two interfaces tends to vary further due to bandgap light excitation and the addition of voltage, which allows the magnitude of the electric field to increase further, as shown in Figure 4.8(b). Thus, additional photogenerated charge carriers are swept from the trap states of the photodetector and move by hopping process from the semiconductor to the barrier interfaces, thus generating a reduction in the resistance of the device and an increase in the photocurrent due to the tunneling of carriers.

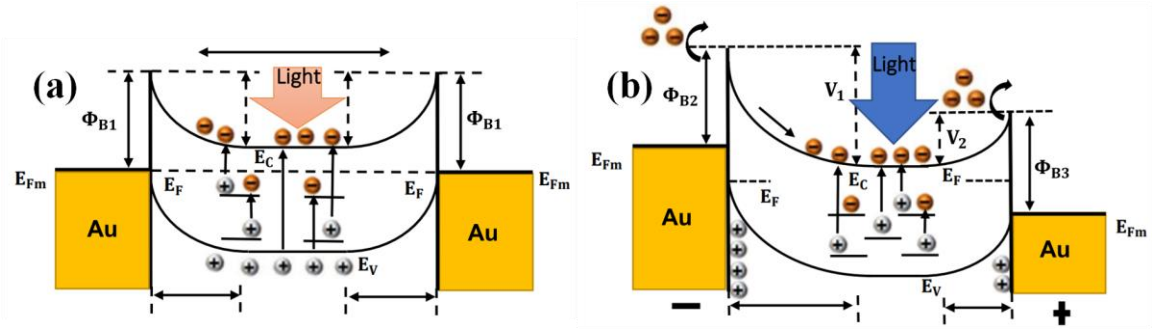

Figure 4. 8 Schematic energy band alignment diagrams for MSM diode-based photodetectors, under illumination **(a)** without and **(b)** with bias voltage.

Thus, MSM-based photodetector under illumination builds up an electric field which leads to the separation of photogenerated charge carriers (electrons in the metal region and holes in the n-type region). This additional charge flow in the semiconductor is incorporated into the back-to-back Schottky diode current, giving rise to a photocurrent, which is expressed in equations (4.3) and (4.4), respectively.

$$I_{ph} = I_L - I_D \,, \tag{4.3}$$

where I_{ph} is the photocurrent, I_L is the light-generated current, and I_D is the back-to-back Schottky diode current. Since the photocurrent is the same for both voltage drops and series resistance, we can write the diode equation in forward bias.

$$I_{ph} = I_L - I_{s1}\left\{exp\left[\frac{qV_1}{\eta_1 k_B T}\right] - 1\right\}. \quad (4.4)$$

In this case, $V_1 = V - V_2 - R_s I_{ph}$, where R_s is the series resistance between back-to-back connected diodes.

4.7 Photocurrent measurement

According to the circuit diagram shown in Figure 4.9, Au/WS_2/Au prototype was connected in series to a resistor R_0 of 38 kΩ and a power supply with adjustable voltage from 0 to 2 V. Then, a lamp was placed approximately 20 cm from the device to illuminate the middle portion of the 2D WS_2 nanosheets thin film. The device was fixed on a variable temperature plate with settings from 18 to 90 °C, respectively. Analog input C of the 850 universal interface was connected in parallel to the resistor to measure the voltage signal due to the photocurrent generated by the photodetector; instead, analog input D was used as a voltage monitoring sensor of the circuit power supply. In addition, a USB cable between the interface and the computer for data acquisition in PASCO Capstone Software was used. The methodology was to evaluate the spectral response of the device in the On and Off state of the light in periods of 20 s during several testing cycles, controlled by a synchronized digital timer. Measurements were made over a wide range of visible spectra, i.e., from near-UV to near-infrared (IR). Where, first, the

photodetector was examined in photovoltaic mode at zero bias. Then, the device was re-evaluated under different temperature conditions generated by a hot plate in contact with the sample substrate. The thermocouple thermometer was used on the gold thin film layers because the substrate base indicated less than the top surface. The procedure was repeated at a power supply from 0.5 to 2 V, exploring the features of the photocurrent spectral response as a function of time under on/off light illumination.

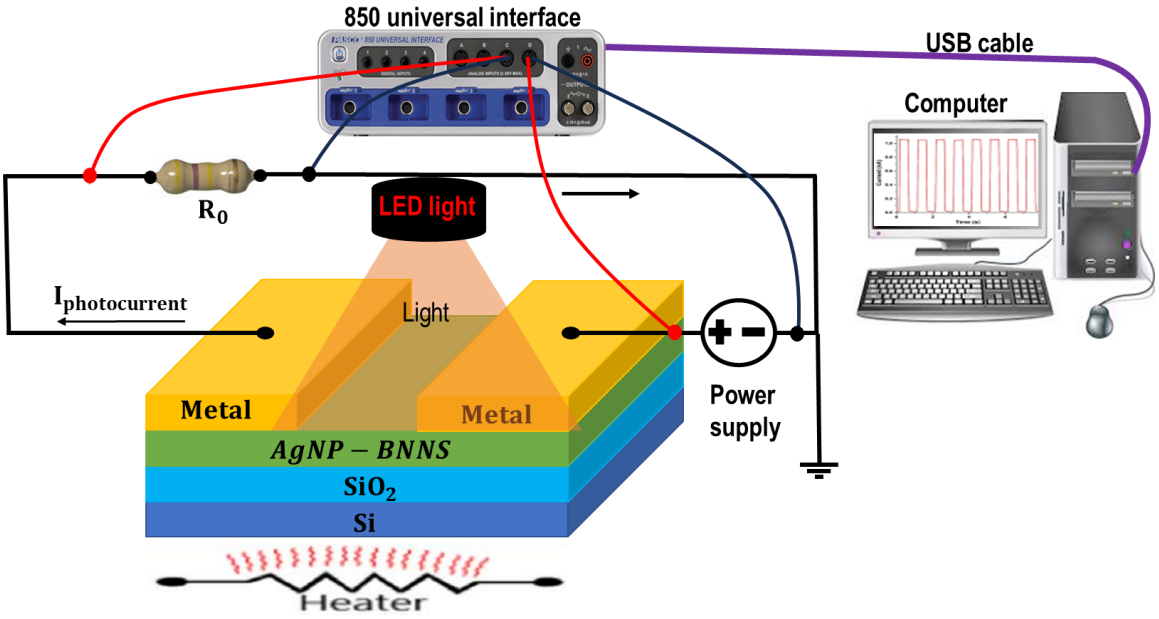

Figure 4. 9 Schematic set-up for the characterization of the circuit photodetector.

4.8 Photovoltaic mode operation

Succeeding characterizations, the photoelectric current was studied in a photosensitive device designed as a back-to-back Schottky diode under the light on/off mode, as shown in Figure 4.10(a). In this test, no external power supply was used. Only 670 nm light-induced photocurrents (I_{ph}) at the illumination intensity

($I_{intensity}$) of 5.2 mW/cm^2 on the surface of the active layer were measured. When the illumination was applied, the light-induced photocurrent was immediately generated up to 3.06 × 10^{-8} A, and when the light was turned off, it was instantly restored to zero. Such a photovoltaic effect was reproduced during multiple testing cycles in 20 s. These results indicate that the developed photosensitive semiconductor device shows an excellent photoresponse to illumination in the near-infrared region of the electromagnetic spectrum. Similarly, at ranges of light wavelengths from 420 to 605 nm, the photodetector device responded selectively and stably, revealing a strong photoresponse at 670 nm, as shown in Figures 4.10(b) and (c). Alternation of the excitation source between the green and red light for the integrated photodiode results in switching of photocurrents between 2.45 ×10^{-8} A and 3.1 × 10^{-8} A, respectively, the latter being because of higher photon absorption in the near-infrared than the rest of the spectra. Photocurrent transport properties in the photovoltaic semiconductor are dependent on light excitation frequencies. This behavior is closely related to the photoelectric effect, as well as to physical and chemical phenomena. In both cases, the light spectrum absorbed by the 2D WS_2 nanosheets is dominated by discrete energy states that condition the charge carrier excitation to a higher energy level that is still contained within the sample. This effect generates photovoltage by separating charges by diffusion, and the illumination pattern must have sufficient energy to overcome the potential barrier for excitation. If we look at Figure 4.10(b) and (c), we can see that each colour of light has a different wavelength and, therefore, excitation energy change defines the generation of charge carriers in the Au/WS_2 contact.

The behavior of the 2D WS_2 nanosheets as a multilayer structure seems to have high efficiency in absorbing photons in a wide range of frequencies to the mere action of light. The top layer nanosheets absorb shorter wavelengths, and the bottom converts the longer ones, as UV-visible absorption spectrum data confirms, giving significantly better conversion efficiency and better photocurrent output. Newer photovoltaic cell designs achieve higher efficiency by converting more light into useful electrons, so expectations are promising for future applications. In addition, 2D WS_2 nanosheets with deficient S atoms could minimize the energy barrier and charge accumulation at the interface to enhance the extraction of photoinduced charge separations and carrier-transfer dynamics in photovoltaic devices.

To further study the effect on the performance of the photodetector device, we define the photocurrent as:

$$I_{ph} = I_{light} - I_{dark}\,, \tag{4.5}$$

$$I_{ph} = c\left(I_{intensity}\right)^{\alpha}, \tag{4.6}$$

where I_{light} is the photocurrent under illumination, I_{dark} is the dark current or the unwanted leakage current, c is a proportionality constant of 6×10^{-10}. α is an empirical value of 0.93 between 0.5 and 1, indicating that the saturation is mainly due to the photogenerated carriers' kinetics involving recombination states and carrier-carrier interactions. This behavior plays a vital role in determining the performance of fast optoelectronic devices.

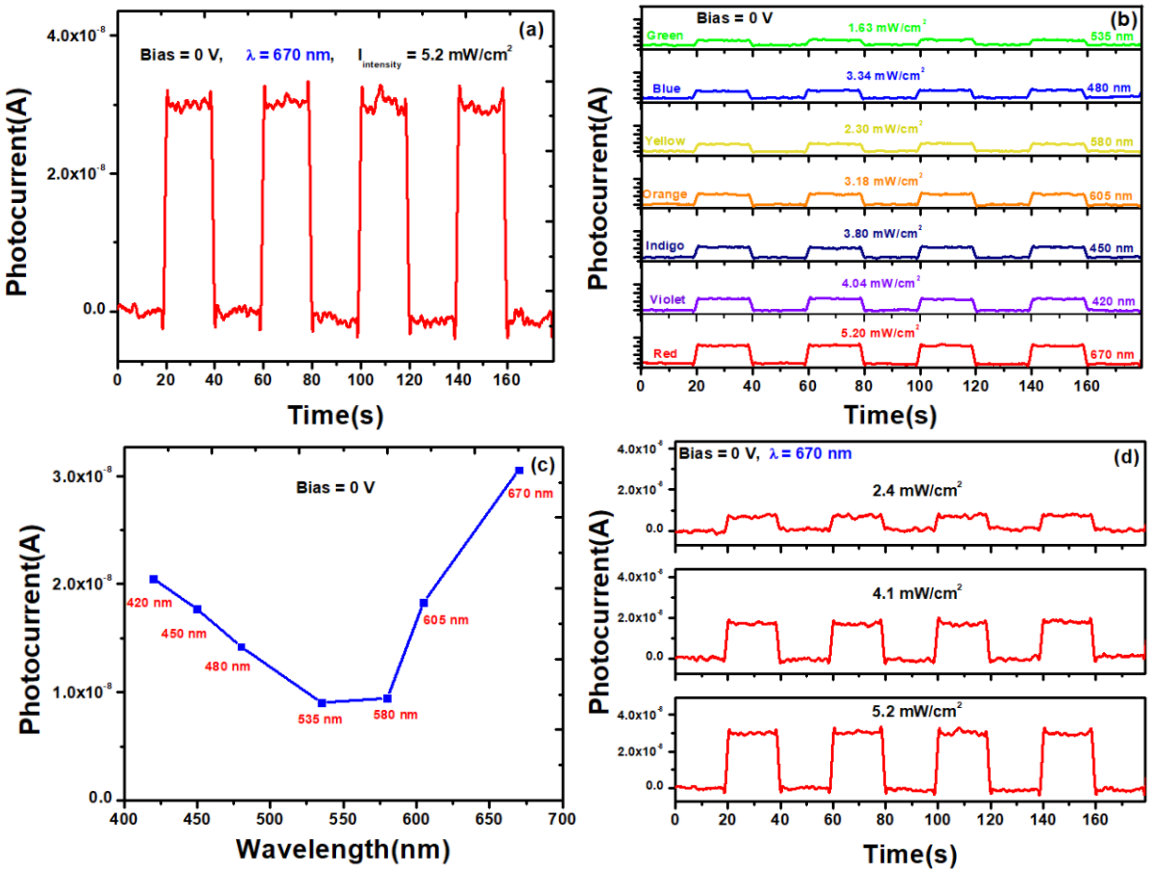

Figure 4. 10 Photodetector device designed as back-back Schottky diode (Au/ WS_2/Au). **(a)** Photocurrent-time cyclical curve under cyclical illumination at 5.20 mW/cm^2, **(b)** photocurrent-time curves at light intensities from 1.63 to 5.20 mW/cm^2, **(c)** photocurrent-wavelength curve, and **(d)** photocurrent-time curves excited with 670 nm light at different illumination intensities.

The illuminating of the light source (P) and the responsivity of an ideal photodetector (R_λ) are described by equations:

$$P = I_{intensity} \times A\,, \tag{4.7}$$

$$R_\lambda = \frac{I_{ph}}{P}\,, \tag{4.8}$$

where A is the active layer surface of the WS_2 film (5×10^{-6} m^2). The responsivity of the device with a bias voltage of zero reached values from 0.1 to 0.12 mA/W in almost the full spectrum of visible light under intensities from 1.63 to 5.2 mW/cm^2. Previous studies by Y.J. Yoon et al. [35] showed the R_λ value in large-area and low-temperature synthesis of few-layered WS_2 films for photodetectors, fabricating by sputtering with 3 kV EBI was 0.19 mA/W at a wavelength of 635 nm with the intensity of 10.7 mW/cm^2 at a bias voltage of 10 V. Similarly, Y.J. Yoon et al. [36] developed the direct WS_2 photodetector fabrication on a flexible substrate using 1kV EBI treatment, where R_λ value was 0.53 mA/W, respectively. These measures are not significantly large compared to the R_λ of our material, characterized under zero bias. This may be because the light S atoms are not so deficient in WS_2 thin-film growth since the S vacancies generate most carrier generation and carrier recombination. According to Yoon, the WS_2 film was less deficient in S, with an S/W ratio of 1.83, while the most deficient was 1.76. These values are higher than our bulk material (S/W = 1.70) and even higher than exfoliated nanosheets (S/W = 1.3), which also explains the need to apply a high bias in photodetectors fabricated with kV EBI treatment. M. Terrones et al. [37] also characterized photosensor devices based on few-layered WS_2 films, where the smallest spectral photoresponse was 2.0 μA/W, a value measured for the red laser of 647 nm, while the highest recorded photoresponse corresponded to 21.2 μA/W, measured with the blue laser of 458 nm at a bias of 5 V. The optical signal magnitudes of our prototype are much higher than the photosensors of Terrones fabricated using the CVD technique. Although the article did not report the atomic concentrations of S

and W, we believe that the absence of S vacancies could be the answer to the low signal at a high bias. An additional advantage of the works of Ali Aldalbahi et al. [38] in the mechanical exfoliation of two-dimensional atomic layer molybdenum disulfide showed high responsivity at wavelengths of 670 nm, where photocurrent measurements were also comparable to the values of 2D WS_2 nanosheets. Therefore, S deficiency and layer stacking of the bulk sample seem to induce higher mobility of charge carriers at low light intensity.

Given that R_λ is used to evaluate the sensitivity of a photodetector, we can say that our material generates a higher photocurrent at low illumination of the light source. This is attributed to the fact that the setting curve follows a power law of photocurrent and light intensity, resulting in more photocurrent generated through the metal-semiconductor junction with a low trapping effect in the width of the depletion region is broadened. Captured carriers are reduced with increasing light power intensity; conducting, more photogenerated electron-hole pairs can contribute to the photocurrent.

When the distance between the light source and the WS_2 thin film was varied, the light intensity on the surface of the active layer decreased as the distance increased, as shown in Figure 4.10(d). The 670 nm light-generated photocurrent was 3.1×10^{-8} A at 5.2 mW/cm^2, 1.8×10^{-8} A at 4.1 mW/cm^2, and finally 0.82×10^{-8} A at 2.4 mW/cm^2, respectively. The photocurrent value decreases as the light power density decreases.

Table 1 shows the performance of some WS_2-based photodetectors on different substrates, fabrication methods, and illumination intensities in the visible spectrum.

Table 4. 1 Comparisons of the performances of WS_2-based photodetectors.

Year	Substrate	Fabrication Method	Wavelength [nm]	Intensity [mW/cm^2]	Responsivity [mA/W]	Detectivity [cm Hz W^{-1}]	Bias Voltage (V)
2021	Polyimide **[24]**	Sputtering with 1 kV EBI treatment	450 532 635	14.9 3.9 10.7	1.25 1.66 0.53	2.52×10^7 3.34×10^7 1.08×10^7	10
2018	SiO_2/Si **[25]**	Sputtering with 3 kV EBI treatment	450 532 635	14.9 3.9 10.7	0.36 1.37 0.19	--------	10
2020	Flexible filter membrane **[26]**	Vacuum filtration	532	59.09	4.04	2.55×10^9	5
2018	SiO_2/Si **[41]**	CVD	532	450	5	--------	10
2013	Quartz **[38]**	CVD	647 458 514	---------	2×10^{-3} 21.2×10^{-3} 0.21×10^{-3}	--------	5
Our work	SiO_2/Si	Spin coating	420 450 670 420 450 670	3.16 2.95 4.13 3.16 2.95 4.13	0.102 0.100 0.120 12.0 10.0 12.74	1.0×10^8 0.9×10^8 1.35×10^8 1.10×10^{10} 0.91×10^{10} 1.20×10^{10}	0 2

This mechanism is because there is an inverse relationship between distance squared and light intensity, i.e., as the distance away from a light source increase, photons of light become spread over a wide area before reaching the WS_2 thin film. The responsivity of the device also decreases slightly, as it is directly proportional to the photocurrent or power law of intensity. However, the periodic On/Off cycles of 20 seconds showed excellent stability under environmental conditions, except for the photocurrent changes due to the decrease in light intensity.

Temperature-correlated photocurrent measurement was performed to validate its viability under normal operating conditions of the photodetector, where the 2D WS_2 nanosheets showed higher sensitivity to light in a wide range of wavelengths. The results verify the effectiveness and stability of the device up to an acceptable temperature range, as shown in Figure 4.11(a) and (b). As the temperature goes up, the absorption depth of light decreases slightly, which could be due to a significant amount of carriers being recombined because of the non-uniform concentration of WS_2 atoms by the vacancies of S. Therefore, changes in environment temperature affect the device more in photovoltaic mode than in the photoconductive mode of operation (reverse biasing). According to the back-to-back Schottky diode's biasing conditions, the anode and cathode are at the same potential in a photovoltaic implementation, i.e., the diode is zero-biased. This implies that the device depends on the generation and recombination of photogenerated charge carriers, the wavelength of the incident light, and the Schottky barrier heights. In addition to this is the temperature dependence of the bandgap, which varies according to the number of stacked layers of the 2D WS_2 nanosheets. For example, the liquid exfoliation of the bulk WS_2 sample showed a direct optical transition of 1.95 eV, which was lower than that of the monolayer (2.05 eV). This allows us to infer that nanosheets with a reduced number of layers may be more resistant to degradation as temperature increases.

On the other hand, the weak Schottky barrier allows the prototype to act as an ohmic contact for a self-powered photodetector in the entire visible spectrum at intensities from 1.6 to 5.2 mW/cm^2, as shown in Figure 4.11(c). Electrical current

can be conducted in both directions of the M-S contact when the WS_2 nanosheets absorb the photons of light to generate pairs of electrons and holes; such the electron diffuses from the metal to the semiconductor, thus increasing the concentration of electrons and not causing depletion of the semiconductor near the junctions. Photodetectors with these features are required since external contacts to a photovoltaic cell need to be ohmic to prevent an unnecessary voltage drop at the contact. Therefore, the low contact resistance and a junction between M-S that has a linear photocurrent-photovoltage curve, as with Ohm's law, are critical for the performance and reliability of semiconductor devices.

The rise and decay times of the WS_2-based prototype exposed to 670 nm light illumination were also measured. The rise time (1.20 s) was slightly longer than the decay time (1.21 s) but with a difference of 0.01 s in the switching change. When the light source was On mode, the photocurrent quickly rose to a high-level steady state, followed by a relatively slow tail, while a reversed behavior was observed when the light switched off, as shown in Figure 4.11(d). This response speed is faster than highly responsive and broadband photodetection based on large-area multilayered WS_2 films grown by pulsed-laser deposition, as reported by G. W. Yang [39]. In our case, we characterized it with zero bias.

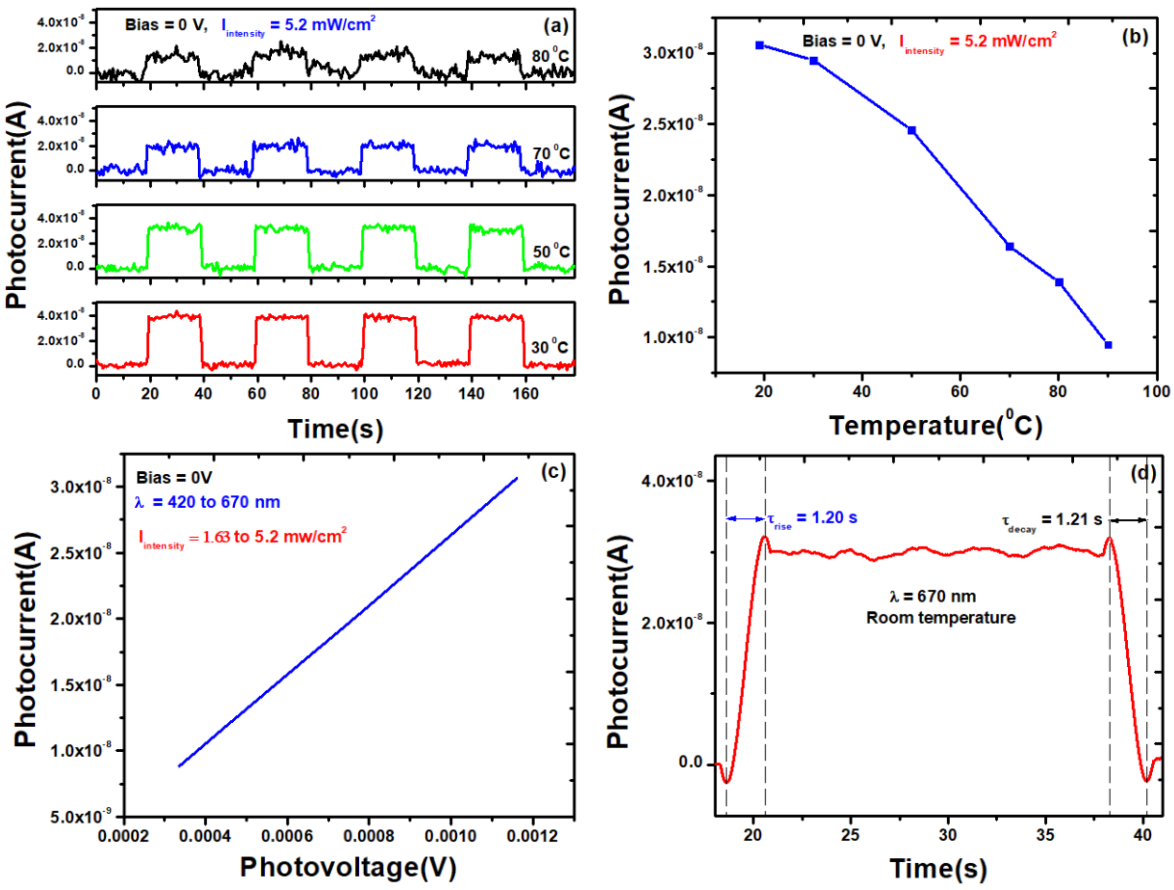

Figure 4. 11 (a, b) Temperature-correlated photocurrent curves under operating conditions from 19 to 90 °C at a light intensity of 5.2 mW/cm^2, **(c)** photocurrent-photovoltage curve at ranges of light wavelengths from 420 to 605 nm and intensities from 1.63 to 5.2 mW/cm^2, and **(d)** rise and decay times of Au/WS_2/Au photodetector device under the illumination of switched On/Off in periods of 20 s.

The detectivity (D*) evaluates the device's sensitivity to weak optical signals. The equation that describes this parameter is:

$$D^* = \frac{R_\lambda A^{1/2}}{(2qI_{dark})^{1/2}}, \tag{4.9}$$

where A is the area of the photosensitive region of the detector and I_{dark} is the dark current (1.84×10^{-7} A). When performing the calculation, a value of 1.35×10^{8} cm Hz W^{-1} was obtained at 5.2 mW/cm^2, representing the acceptable value of a high-performance photodetector under zero bias. A device with these characteristics can be attributed to the higher mobility and absorption of the present WS_2 nanosheet-based film, associated with increased carrier recombination dynamics and excellent photoresponse at low light intensities. Thus, confirming that the signal/noise ratio is within the allowed standards for a self-powered photodetector. However, as the temperature increases, the detectivity of the device decreases due to increased signal/noise.

4.9 Bias effect

Variation characteristics as a function of time have been explored for the photodetector device to a 670 nm light illumination at different applied biases and a light intensity of 4.1 mW/cm^2, as shown in Figure 4.12(a). Similar to the previous case, the illumination of switched on/off was set in periods of 20 s during several testing cycles. The device exhibited switching behavior and repeatability without degradation at bias voltage ranges from 0.5 to 2 V. The typical photocurrent response of the device to the light source increased from 2.0×10^{-7} to 2.6×10^{-6} A with an increase of bias. Thus, a high bias and light irradiation favor the fast separation and transportation of the photoinduced charge carriers to the working electrodes, increasing the photocurrent, as shown in Figure 4.12(b). As the width of the depletion region is broadened, the built-in electric field of the optical metal-semiconductor heterostructure is enhanced, generating recombination of photo-

generated electron and hole pairs favoring the rapid separation of the photogenerated charge carriers, resulting in the increment of photocurrent and a faster response time to the On/Of light cycles as the bias voltage increases. With the depletion layer (forward bias) reduction, charge traps generated by interstitial impurities, S vacancies, and lattice defects are minimized, which also contributes to a higher photocurrent between WS_2/Au junctions.

Performing cyclic tests under On/Off mode at a bias of 2.0 V, good repeatability and a stable baseline was visible when the device was exposed to 670, 420, and 450 nm at the same distance between the sample and the light source, respectively. When generating light-induced photocurrents, the prototype's conversion efficiency for red illumination appears to be higher than that for the violet and indigo spectra (Figure 4.12(c)), reaching a responsivity of 12.74 mA/W to 670 nm, as shown in Figure 4.12(d). This value is more significant than that of the growth of wafer-scale standing layers of WS_2 for self-biased high-speed UV–visible–NIR optoelectronic devices grown by the CVD technique, where the responsivity and intensity were 450 mW/cm^2 and 5 mA/W at a bias voltage of 10 V, according to the measurements obtained by J.C. Ho et al. [40]. Similarly, K. Huang et al. [41] characterized a flexible broadband photodetector based on WS_2 nanosheets films obtained by the vacuum filtration method, reaching a spectral photoresponse of 4.04 mA/W at 532 nm with an intensity of 59.09 mW/cm^2 at the bias of 5 V. These values exhibit a lower electrical output per photon input than our photodetector device. In addition, under 2 V detectivity reached up to 1.2×10^{10} cm $Hz^{1/2}$ W^{-1}, which confirms the intrinsic quality of the prototype. This

photodetector device that exhibits highly sensitive to light intensity is even better than WS_2 photodetectors shown in Table 1 due to the rapid separation of the photogenerated carrier at the Au/WS_2 interface.

Therefore, 2D WS_2 nanosheets exhibit a better absorption for the light spectra of 420 nm and 670 nm, the latter being the maximum intensity in the visible range due to the higher number of optically generated carriers with an excitation photon energy of about 1.85 eV of the bandgap. This value is within the range of the direct optical transitions at the K point of the Brillouin zone for exciton A. Accordingly, the quantum confinement in WS_2 nanosheets defines the absorption of light in the visible range. If adding a bias voltage of 2 V is on the illuminated nanosheet terminals, the magnitude of the electric field increases, generating additional photogenerated charge carriers from the semiconductor to the barrier interfaces, which improves responsivity and detectivity.

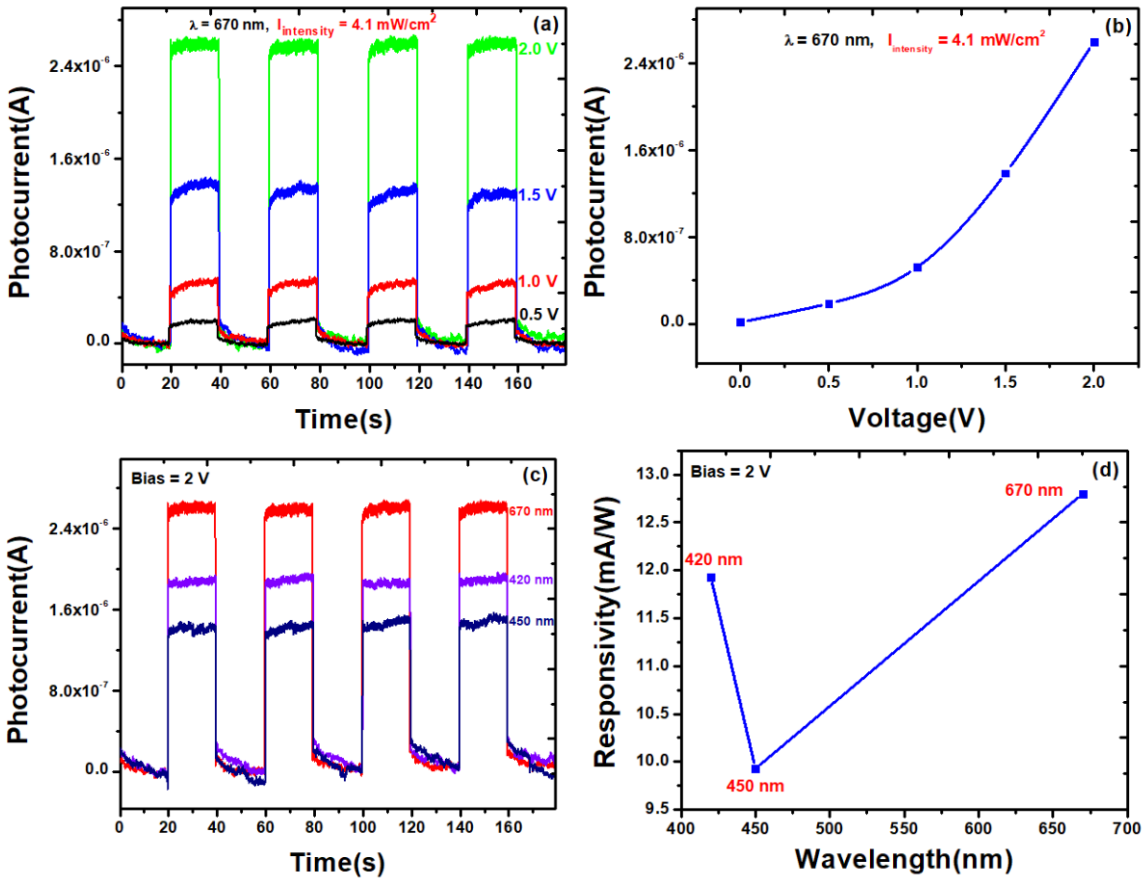

Figure 4. 12 The bias voltage effect on the fabricated photodetector was exposed to the light intensity of 4.1 mW/cm2. **(a)** Photocurrent-time curve under On/Off mode with bias from 0.5 to 2 V on the spectral response of 670 nm, **(b)** photocurrent-voltage curve from 0 to 2 V, **(c)** photocurrent-time curve under On/Off mode on the spectral responses from 420 to 670 nm at 2 V, and **(d)** responsivity-wavelength curve at 2 V.

4.10 Conclusions

2D nanosheets deficient in S showed a higher photon absorption in the near-infrared range with a photocurrent output of 3.06×10^{-8} A and a detectivity of 1.35×10^{8} cm Hz W^{-1} at 5.2 mW/cm^2, which is the acceptable value of a high-performance photodetector under zero bias. Similarly, the responsivity of the device reached a deal of ~0.12 mA/W, several orders of magnitude larger than photosensor devices based on few-layered WS_2 films grown by the CVD technique. These results suggest that the high degree of delamination of the bulk sample improves the light absorption in 2D WS_2 nanosheets in a wide range of the visible spectrum. In addition, the defect states induced by S vacancies in the quantum confinement process improve the mobility and photogenerated charge carriers. The direct optical transition of 1.95 eV, close to the band structure of monolayer transition, allows the exfoliated nanosheets along the (002) plane to be highly stable to light On/Off cycles, even more resistant to degradation in higher temperature environments.

At 2 V, the responsivity was 12.74 mA/W and a photocurrent of 2.6×10^{-6} A at 4.1 mW/cm^2, which is better electrical output per light input than flexible broadband photodetectors based on WS_2 nanosheets films obtained by the vacuum filtration method. This value was also larger than that of the growth of wafer-scale standing layers of WS_2 for self-biased high-speed UV–visible–NIR optoelectronic devices grown by the CVD technique, where the responsivity and intensity were 450 mW/ cm^2 and 5 mA/W at a bias voltage of 10 V. In addition, the detectivity of 1.2×10^{10} cm $Hz^{1/2}$ W^{-1} exhibited high sensitivity to the light intensity

than WS_2 photodetectors fabricated by sputtering with EBI treatment and CVD technique, where the values ranged from 10^7 to 10^9 cm $Hz^{1/2}$ W^{-1} at bias voltages of 10 and 5 V, respectively. Thus, nanosheets exhibit high sensitivity and enhanced photoresponse when the built-in electric field of the optical Au/WS_2/Au heterostructure is increased. The rapid recombination and separation of the photogenerated carriers significantly reduce charge traps in the Au/WS_2 interface; similarly, the depletion layer becomes narrower and allows the barrier to carrier injection in the forward bias direction to be reduced. Illumination at 670 nm also provides a higher density of carriers from the bandgap to the conduction band, thus showing a higher optical signal than the rest of the visible spectrum.

Our studies also showed that WS_2 thin film with inherent defects and transparent sample improves light absorption over a wide range of the optical spectrum. Hence, on a transparent substrate, it is possible to obtain a better photoresponse of the device with appropriate control in the growth of the layers since almost all light passes directly through them. Unlike the most expensive instruments, the liquid exfoliation method of 2D materials offers a facile and low-cost technique to produce mono- and few-layer 2D nanosheets in a commercially viable way.

4.11 References

[1] B.R. Huang, D. Kathiravan, A. Saravanan, E.W. Sung, Reducing noise current in exfoliated WS2 nanosheets using an ultra-nanocrystalline diamond substrate and their enhanced NIR photodetection properties, J Mater Chem C Mater. 10 (2022) 6061–6069. https://doi.org/10.1039/D2TC00127F.

[2] Y. Luo, H. Guan, W. Zhu, J. Yu, Z. Chen, J. Dong, G. Chen, J. Zhang, W. Qiu, H. Lu, Y. Zhong, M. Jiang, X. Wang, H. Li, Z. Zhang, Highly sensitive all-optical control of light in WS_2 coated microfiber knot resonator, Optics Express, Vol. 26, Issue 21, Pp. 27650-27658. 26 (2018) 27650–27658. https://doi.org/10.1364/OE.26.027650.

[3] S. Behura, K.-C. Chang, Y. Wen, R. Debbarma, S. Deng, M.R. Seacrist, V. Berry, A CVD process for the fabrication of WS 2 films on p-Si substrates for photovoltaic and spectral responses, (2017). https://doi.org/10.1109/MNANO.2017.2676184.

[4] Y. Shao, Y. Shao, C. Chen, J. Han, D. Kong, W. Wu, Y. Gao, Wavelength-dependent nonlinear absorption and ultrafast dynamics process of WS_2, OSA Continuum, Vol. 2, Issue 9, Pp. 2755-2763. 2 (2019) 2755–2763. https://doi.org/10.1364/OSAC.2.002755.

[5] B.H. Kim, H. Yoon, S.H. Kwon, D.W. Kim, Y.J. Yoon, Direct WS2 photodetector fabrication on a flexible substrate, Vacuum. 184 (2021). https://doi.org/10.1016/J.VACUUM.2020.109950.

[6] B.H. Kim, H.H. Gu, Y.J. Yoon, Large-area and low-temperature synthesis of few-layered WS2 films for photodetectors, 2D Materials. 5 (2018) 045030. https://doi.org/10.1088/2053-1583/AADEF8.

[7] J. Li, J. Han, H. Li, X. Fan, K. Huang, Large-area, flexible broadband photodetector based on WS2 nanosheets films, Materials Science in Semiconductor Processing. 107 (2020) 104804. https://doi.org/10.1016/J.MSSP.2019.104804.

[8] J. Xu, X. Cheng, T. Liu, Y. Yu, L. Song, Y. You, T. Wang, J. Zhang, Oxygen-incorporated and layer-by-layer stacked WS2 nanosheets for broadband, self-driven and fast-response photodetection, Nanoscale. 11 (2019) 6810–6816. https://doi.org/10.1039/C8NR10350J.

[9] X. Ren, B. Wang, Z. Huang, H. Qiao, C. Duan, Y. Zhou, J. Zhong, Z. Wang, X. Qi, Flexible self-powered photoelectrochemical-type photodetector based on 2D WS2-graphene heterojunction, FlatChem. 25 (2021) 100215. https://doi.org/10.1016/J.FLATC.2020.100215.

[10] Y. Shi, H. Li, L.J. Li, Recent advances in controlled synthesis of two-dimensional transition metal dichalcogenides via vapour deposition techniques, Chem Soc Rev. 44 (2015) 2744–2756. https://doi.org/10.1039/C4CS00256C.

[11] L. Zeng, L. Tao, C. Tang, B. Zhou, H. Long, Y. Chai, S.P. Lau, Y.H. Tsang, High-responsivity UV-Vis Photodetector Based on Transferable WS2 Film

Deposited by Magnetron Sputtering, Scientific Reports 2016 6:1. 6 (2016) 1–8. https://doi.org/10.1038/srep20343.

[12] T.A.J. Loh, D.H.C. Chua, A.T.S. Wee, One-step Synthesis of Few-layer WS2 by Pulsed Laser Deposition, Scientific Reports 2015 5:1. 5 (2015) 1–9. https://doi.org/10.1038/srep18116.

[13] C.M. Orofeo, S. Suzuki, Y. Sekine, H. Hibino, Scalable synthesis of layer-controlled WS2 and MoS2 sheets by sulfurization of thin metal films, Appl Phys Lett. 105 (2014) 083112. https://doi.org/10.1063/1.4893978.

[14] Y. Lee, J.W. Jung, J.S. Lee, Highly electroconductive and uniform WS2 film growth by sulfurization of W film using diethyl sulfide, Mater Chem Front. 5 (2021) 3692–3698. https://doi.org/10.1039/D1QM00173F.

[15] R. Lv, J.A. Robinson, R.E. Schaak, D. Sun, Y. Sun, T.E. Mallouk, M. Terrones, Transition Metal Dichalcogenides and Beyond: Synthesis, Properties, and Applications of Single- and Few-Layer Nanosheets, Acc Chem Res. 48 (2014) 56–64. https://doi.org/10.1021/AR5002846.

[16] B. Adilbekova, Y. Lin, E. Yengel, H. Faber, G. Harrison, Y. Firdaus, A. El-Labban, D.H. Anjum, V. Tung, T.D. Anthopoulos, Liquid phase exfoliation of MoS2 and WS2 in aqueous ammonia and their application in highly efficient organic solar cells, J Mater Chem C Mater. 8 (2020) 5259–5264. https://doi.org/10.1039/D0TC00659A.

[17] X. Zhang, H. Xu, J. Wang, X. Ye, W. Lei, M. Xue, H. Tang, C. Li, Synthesis of Ultrathin WS2 Nanosheets and Their Tribological Properties as Lubricant

Additives, Nanoscale Res Lett. 11 (2016). https://doi.org/10.1186/S11671-016-1659-3.

[18] M. Tayebi, Z. Masoumi, B.K. Lee, Ultrasonically prepared photocatalyst of W/WO3 nanoplates with WS2 nanosheets as 2D material for improving photoelectrochemical water splitting, Ultrason Sonochem. 70 (2021) 105339. https://doi.org/10.1016/J.ULTSONCH.2020.105339.

[19] I. Paradisanos, N. Pliatsikas, P. Patsalas, C. Fotakis, E. Kymakis, G. Kioseoglou, E. Stratakis, Spatial Non-Uniformity in Exfoliated WS 2 Single layers, (n.d.).

[20] S. Salehi, A. Saffarzadeh, Atomic defect states in monolayers of MoS2 and WS2, Surf Sci. 651 (2016) 215–221. https://doi.org/10.1016/J.SUSC.2016.05.003.

[21] G. Pradhan, A.K. Sharma, Linear and nonlinear optical response of sulfur-deficient nanocrystallite WS2 thin films, J Mater Sci. 54 (2019) 14809–14824. https://doi.org/10.1007/S10853-019-03986-8/FIGURES/13.

[22] C.J. Carmalt, I.P. Parkin, E.S. Peters, Atmospheric pressure chemical vapour deposition of WS2 thin films on glass, Polyhedron. 22 (2003) 1499–1505. https://doi.org/10.1016/S0277-5387(03)00194-3.

[23] J. Díaz-Reyes, J.A. Balderas-López, Obtaining of films of tungsten trioxide (WO 3) by resistive heating of a tungsten filament, 21 (2008) 12–17. http://www.redalyc.org/articulo.oa?id=94215160003 (accessed September 15, 2022).

[24] I. E. Wachs, C. C. Chersich, J. H. Iiardenbergh, Reduction of W03/A1203 and unsopported W03: A comparative ESCA study, Appl Catal. 13 (1985) 335–346. https://doi.org/10.1016/S0166-9834(00)81152-5.

[25] S. Duwal, M. Kim, C.S. Yoo, Seven-Coordinated “metallic” WO3at High Pressures, Journal of Physical Chemistry C. 124 (2020) 27040–27048. https://doi.org/10.1021/ACS.JPCC.0C09005/ASSET/IMAGES/LARGE/JP0C09005_0007.JPEG.

[26] Z. Li, S. Wu, Z. Wang, Y.Q. Fu, Doping induced structural transformation in tungsten trioxide, J Alloys Compd. 672 (2016) 155–160. https://doi.org/10.1016/J.JALLCOM.2016.02.082.

[27] J. Su, X. Feng, J.D. Sloppy, L. Guo, C.A. Grimes, Vertically aligned WO3 nanowire arrays grown directly on transparent conducting oxide coated glass: Synthesis and photoelectrochemical properties, Nano Lett. 11 (2011) 203–208. https://doi.org/10.1021/NL1034573/ASSET/IMAGES/LARGE/NL-2010-034573_0002.JPEG.

[28] B. Groven, Y. Shi, P. Morin, al -, E.E. Ifan L Stephens, C. Ducati, D.J. Fray -, D. Liu, Z. Tang -, F. Wang, S. Li, M.A. Bissett, I.A. Kinloch, Z. Li, R.J. Young, Strain engineering in monolayer WS2 and WS2 nanocomposites, 2d Mater. 7 (2020) 045022. https://doi.org/10.1088/2053-1583/ABABF1.

[29] S. Baroni, S. de Gironcoli, A. Dal Corso, P. Giannozzi, Phonons and related crystal properties from density-functional perturbation theory, Rev Mod Phys. 73 (2001) 515. https://doi.org/10.1103/RevModPhys.73.515.

[30] L. Zhang, A. Zunger, Evolution of electronic structure as a function of layer thickness in group-VIB transition metal dichalcogenides: Emergence of localization prototypes, Nano Lett. 15 (2015) 949–957. https://doi.org/10.1021/NL503717P/SUPPL_FILE/NL503717P_SI_001.PDF.

[31] H.R. Gutiérrez, N. Perea-López, A.L. Elías, A. Berkdemir, B. Wang, R. Lv, F. López-Urías, V.H. Crespi, H. Terrones, M. Terrones, Extraordinary room-temperature photoluminescence in triangular WS 2 monolayers, Nano Lett. 13 (2013) 3447–3454. https://doi.org/10.1021/NL3026357/SUPPL_FILE/NL3026357_SI_001.PDF.

[32] K.K. Kam, B.A. Parkinson, Detailed photocurrent spectroscopy of the semiconducting group VIB transition metal dichalcogenides, Journal of Physical Chemistry. 86 (2002) 463–467. https://doi.org/10.1021/J100393A010.

[33] J. Osvald, Back-to-back connected asymmetric Schottky diodes with series resistance as a single diode, Physica Status Solidi (a). 212 (2015) 2754–2758. https://doi.org/10.1002/PSSA.201532374.

[34] W. Ortiz, N.J. Ramirez, D. Barrionuevo, M.K. Bhattarai, P. Feng, Characterization of 2D boron nitride nanosheets with hysteresis effect in the

Schottky junctions, Nano Express. 2 (2021) 010020. https://doi.org/10.1088/2632-959X/ABDF6C.

[35] B.H. Kim, H.H. Gu, Y.J. Yoon, Large-area and low-temperature synthesis of few-layered WS2 films for photodetectors, 2D Materials. 5 (2018) 045030. https://doi.org/10.1088/2053-1583/AADEF8.

[36] B.H. Kim, H. Yoon, S.H. Kwon, D.W. Kim, Y.J. Yoon, Direct WS2 photodetector fabrication on a flexible substrate, Vacuum. 184 (2021). https://doi.org/10.1016/J.VACUUM.2020.109950.

[37] N. Perea-Lõpez, A.L. Elías, A. Berkdemir, A. Castro-Beltran, H.R. Gutiérrez, S. Feng, R. Lv, T. Hayashi, F. Lõpez-Urías, S. Ghosh, B. Muchharla, S. Talapatra, H. Terrones, M. Terrones, Photosensor Device Based on Few-Layered WS2 Films, Advanced Functional Materials. 23 (2013) 5511–5517. https://doi.org/10.1002/ADFM.201300760.

[38] A. Aldalbahi, T. Ahamad, S.M. Alshehri, Z.B. Wang, P.X. Feng, Three-dimensional architectures composed of two-dimensional atomic layer molybdenum disulphide for solar cell and self-powered photodetectors with improved performance:, Https://Doi.Org/10.1177/01445987211036828. (2021). https://doi.org/10.1177/01445987211036828.

[39] J.D. Yao, Z.Q. Zheng, J.M. Shao, G.W. Yang, Stable, highly-responsive and broadband photodetection based on large-area multilayered WS2 films grown by pulsed-laser deposition, Nanoscale. 7 (2015) 14974–14981. https://doi.org/10.1039/C5NR03361F.

[40] C. Lan, Z. Zhou, Z. Zhou, C. Li, L. Shu, L. Shen, D. Li, R. Dong, S. Yip, J.C. Ho, Wafer-scale synthesis of monolayer WS 2 for high-performance flexible photodetectors by enhanced chemical vapor deposition, Nano Research. 11 (2018) 3371–3384. https://doi.org/10.1007/s12274-017-1941-4.

[41] J. Li, J. Han, H. Li, X. Fan, K. Huang, Large-area, flexible broadband photodetector based on WS2 nanosheets films, Materials Science in Semiconductor Processing. 107 (2020) 104804. https://doi.org/10.1016/J.MSSP.2019.104804.

Chapter 5

Fabrication and application of 2D boron nitride nanosheets with hysteresis effect in the Schottky junctions

2D hexagonal boron nitride nanosheet (BNNS) exhibits a honeycomb structure analog of graphene. The spacing between 2-layers is about 0.332 nm, and the lattice distance between the B–B or N–N atom separations is 0.22 nm. It shows a strong (002) diffraction peak in the XRD spectrum [1, 2]. Moreover, BNNS presents good thermal conductivity and stability over a wide range of temperatures. BNNS bandwidth is in the range of 4–6 eV, by doping with enough carbon (C) [3, 4], the bandgap is minimized, and a set of discrete energy levels are formed in the gap of BNNS. Previous research has already shown that the electronic and electrical structures could be improved with the C content [5–8]. Furthermore, BNNS film appears to have stable features even at high temperatures, so it has a variety of applications in polymeric [9, 10], flexible electronics [11, 12], Junction Field Effect Transistor (JFET) [13, 14], magneto-optics [15], and optoelectronics based on 2D crystals [16], etc.

Based on the special properties of the BNNS film, we propose two models of back-to-back Schottky diodes with specific characteristics. First is an Au/BNNS/Au type model grown onto the SiO_2/Si substrate [17]. The second is Au/BNNS/Mo, where BNNS is deposited directly on the molybdenum substrate.

In the I–V representation, Au/BNNS/Au-based rectifiers exhibit symmetric characteristics, while Au/BNNS/Mo is asymmetric. When measured under low bias

voltage, both have their hysteresis switching characteristics. These are consistent with the analysis of the Poisson equation in the metal/semiconductor interface (n-type material) [18, 19]. This behavior of the 2D material offers a way to achieve a high hysterical switching quality in both the ‘set’ and ‘reset’ states at low power consumption, which may propose an improvement to recent studies carried out on memory devices with a thinner BNO_x layer [20], as well as in the Ni/n-type 4H-SiC Schottky structure [21, 22]. For example, BN monolayer-based resistance nonvolatile studied under different electrodes that showed stable bipolar and unipolar nonvolatile switching was studied [23–25]. In the same manner, in a multilayer structure, it is possible to grow the thickness of the h-BN film, which enhances the charge capture center to achieve better Poole-Frenkel conduction [26–28], comparable to the Schottky effect. This behavior of BNNS shows promise for several applications, such as non-volatile memory devices [29], pulse voltages, etc. In previous studies, hysteresis has only been tested in 2D materials with graphene oxide and molybdenum disulfide [30–32]. Although these showed charge traps in the oxide dielectric layer, these observations were limited to higher room temperature, so the BNNS film may be an ideal candidate to obtain a more stable hysteresis over a wide temperature range [33].

During the last several years, great progress has been made in resistance switching and electrical hysteresis investigations. This is partially attributed to newly developed nanotechnologies that were used to effectively control material nanostructures and MEMS (Micro-Electro-Mechanical Systems) fabrication [34, 35]. The BNNS samples used in the present work are very different from previous

work where a single atomic or multi-layer sheet was used. The present sample consists of a large number of super-thin BN nanosheets randomly distributed over the entire surface of the substrate [36, 37]. Fabrication is extremely simple and MEMS techniques are not necessary.

5.1 BNNS structure characterizations

SEM image of the BNNS film indicated that the obtained sample had a uniform and compact surface of round-shaped layers at the 10 μm scale, as shown in Figure 5.1(a). Following an increase at the 5 μm scale, several small sheets were exhibited, which is characteristic of multilayer films as shown in Figure 5.1(b). Instead, the Raman spectrum of the BNNS exhibits a peak around 1350 to 1360 cm^{-1} belonging to the Raman active vibrational mode (E_{2g}) [39, 40], as shown in Figure 5.1(c), which is compatible with measurements analogous to these and is directly related to a hexagonal phase of BNNS.

X-ray diffraction (XRD) about BNNS film has a highly crystalline structure with the most intense and sharp peak at 2θ = 26.77°, corresponding to the crystallographic plane (002), as shown in Figure 5.1(d) [41]. Using Bragg's law, we calculated the interlayer distance at BNNS film through relation.

$$d = \frac{n\lambda}{2sin\theta}, \tag{5.1}$$

where d is the interlayer distance of the crystalline plane measured in nm, λ is the wavelength of the X-ray source (λ = 1.54 Å), n is the order of reflection (n = 1), and θ is the angle of incidence in degrees of the plane. If analyzing the crystalline plane

(002), the interlayer distance is 0.332 nm, which is within the range of the values established previously [42].

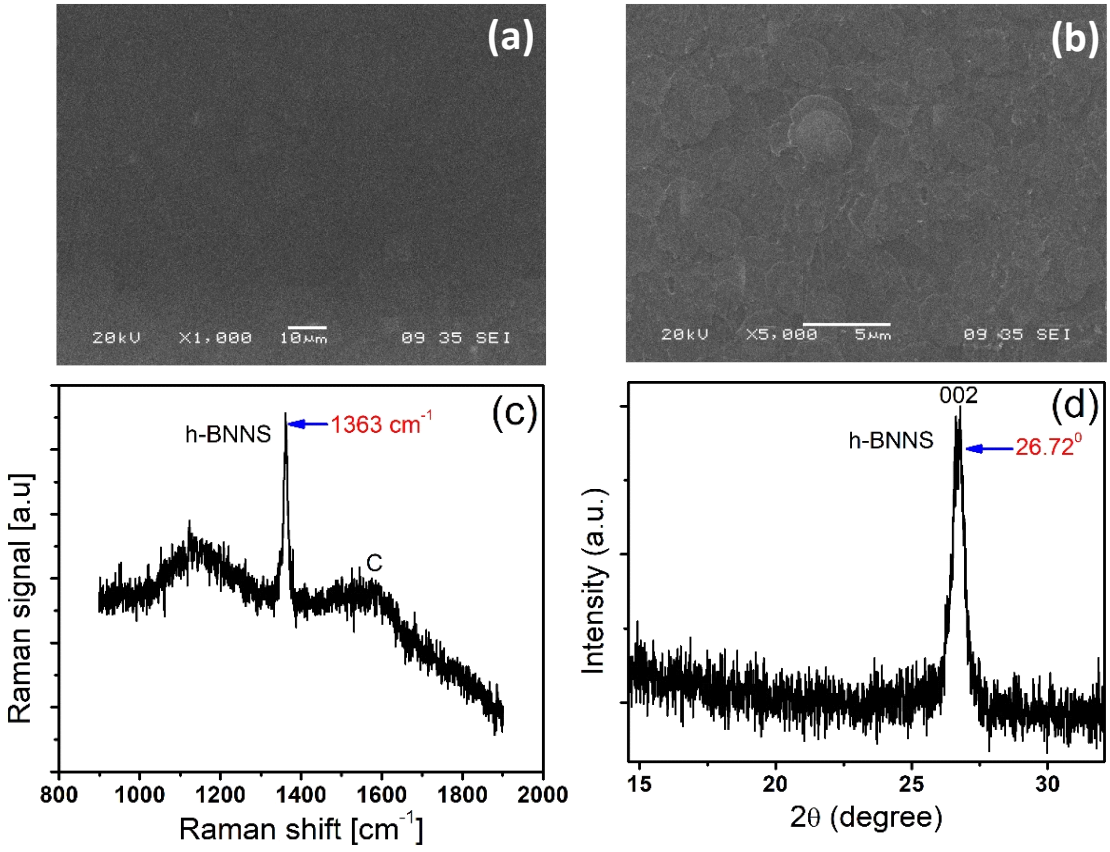

Figure 5. 1 The structure of the BNNS film is shown through **(a) - (b)** scanning electron microscopy (SEM) on the 10 um, 5 µm scale bar, **(c)** Raman scattering spectrum, **(d)** and X-ray diffraction.

Very detailed descriptions of measurements of sheet thicknesses can be found in our previous work [43, 44]. A high-resolution TEM (Transmission Electron Microscope) was used to estimate the thickness of the single sheet by measuring the fringe pattern at the sheet's edge. Each fringe is related to a single atomic layer

with a thickness of around 0.33 nm. Accordingly, the thickness of the obtained BNNS can be estimated at around 3-4 nm (8-11 layers).

5.2 Energy band diagram of back-to-back Schottky barriers

In this section, we propose a model based on energy band theory for the special case of two back-to-back Schottky diodes with two identical (Au-Au) and different contacts (Au-Mo). First, in the equilibrium state, Au/BNNS/Au contacts are a symmetric Schottky structure under the same vacuum level, as shown in Figure 5.2 (a). Alignment of Fermi energy leads to the formation of band diagrams and the barrier height in the metal/semiconductor interface states. These junctions produce different energy values in the Schottky barrier, where Φ_m is the work function of the gold (5.2 eV), Φ_s is the work function of the semiconductor, Φ_B is the barrier height ($\Phi_B = \Phi_m - q\chi_s$), $q\chi_s$ is the electron affinity of the semiconductor (the electron affinities of Au and Mo are 222.8 kJ/mol and 71.9 kJ/mol), E_{Fm} is the Fermi level of the gold (5.20 eV), E_F is the Fermi level of the semiconductor, E_V is the valence band edge, E_C is the conduction band edge, V_i is the built-in-voltage barrier ($qV_i = \Phi_m - \Phi_s = \Phi_B - (E_c - E_F)$), and W is the thickness of the depletion region, which depends on the concentration of ionized acceptor atoms. In contrast, Au/BNNS/Mo contacts have different barrier heights relative to the vacuum level in the equilibrium state, resulting in a symmetric structure, as shown in Figure 5.2 (b). Molybdenum band diagrams differ from gold at the metal/semiconductor interface, which is represented by prime values; where $\Phi_m{}'$ is the work function of the molybdenum (4.6 eV), $E_F{}'$is the Fermi level (4.20 eV), $\Phi_B{}'$ is the barrier height, etc.

Since the contact is metal and the semiconductor is n-type, the built-in-voltage barrier is expressed by

$$V_i = \frac{\Phi_B}{q} - \frac{kT}{q}\ln\left(\frac{N_C}{N_D}\right), \tag{5.2}$$

where q is the elementary charge, k is the Boltzmann constant, T is the absolute temperature, N_C is the effective state density in the conduction band that is constant for a given temperature, and N_D is the donor doping level. If we use moderate to lower doped semiconductors, we can reduce the Schottky barrier even further.

When an external voltage is applied to the back-to-back Schottky diodes, electron-hole pairs are generated, creating the charge flow and voltage drops on single diodes, as shown in Figure 5.2(c). Electrons tend to move toward a positive bias because the voltage drop from V_i to V_i-V_F on a 2D semiconductor induces a narrow depletion region (W). On the contrary, under negative bias, the voltage drop increases from V_i to $V_i + V_R$, which in turn causes a wide depletion region. This behavior of the back-to-back Schottky diodes is directly related to the concentration of dopants in the semiconductor material. In the case of BNNS, the carbon concentration also causes a narrow depletion region, allowing electrons to move above their thermal equilibrium value. Since a large amount of carriers are generated in the depletion region, not all valence electrons become free electrons, so some are trapped by the impurities in the sample, so these are also related to the hysteresis effect.

Au/BNNS/Mo Schottky barriers are analogous to those of Au/BNNS/Au. However, when interacting with two types of contacts, barrier heights are asymmetric. In other words, their values are not the same. This behavior could be observed from their I–V characteristic curves that would be discussed later.

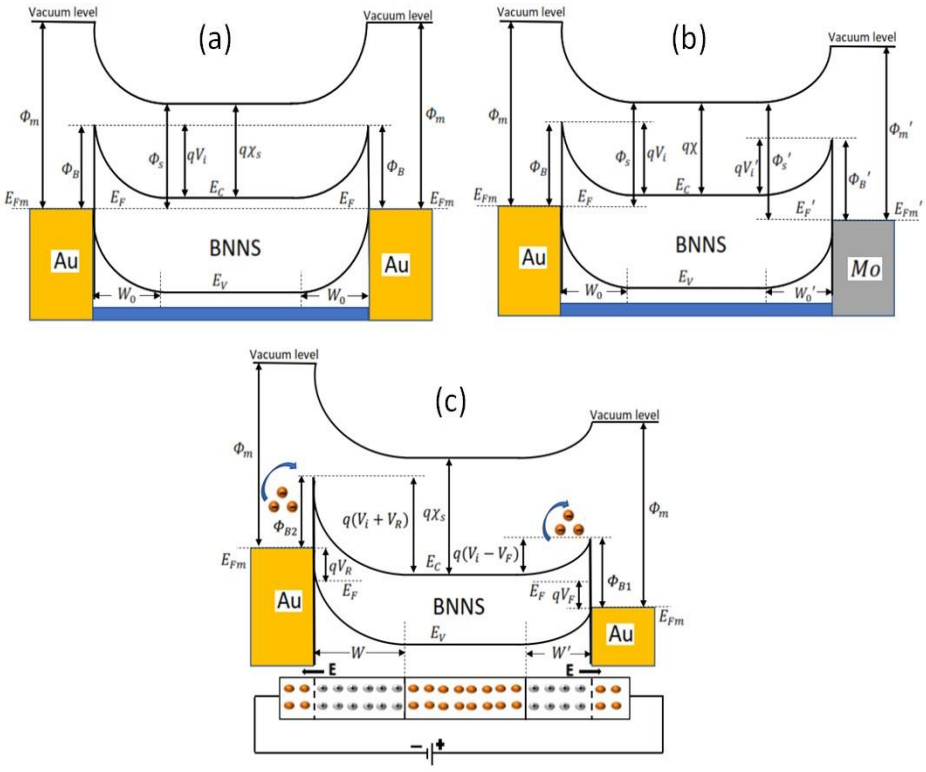

Figure 5. 2 Back-back Schottky barrier formed at metal-semiconductor-metal junctions. **(a)–(b)** Energy band diagrams of metal and semiconductor (n-type) after contacts, **(c)** energy band diagrams with external bias voltage.

5.3 Set up and operation of current-voltage measurement system

Two back-to-back Schottky barrier structures were fabricated in the present study to obtain different electrical properties. First were performed with Au/BNNS/Au junctions, as shown in Figure 5.3(a). According to the synthesis

method, BNNSs were deposited onto the SiO_2/Si substrates. Then, the gold electrode elements were deposited in an argon gas environment at a power level of 250 watts by a sputtering method. The sputtering rate was 10 seconds to produce the gold film of 80 nm on 1 μm thick BNNS film where the typical thickness of single sheet is around 3–4 nm. The separation between the gold electrodes was 1 mm to form the back-to-back Schottky diode. In the same way, for Au/BNNS/Mo junctions, BNNSs were grown on the Mo substrate using the same techniques as the first case, as shown in Figure 5.3(b). Each of the Schottky diodes was connected to an external power supply whose voltage variable (V) was 0 to 20 V, and fixed resistance (R_0) was 10 MΩ. Then, a heater was used to change the operating conditions of the Schottky structure on the I–V curve in the range of 0 to 170 °C.

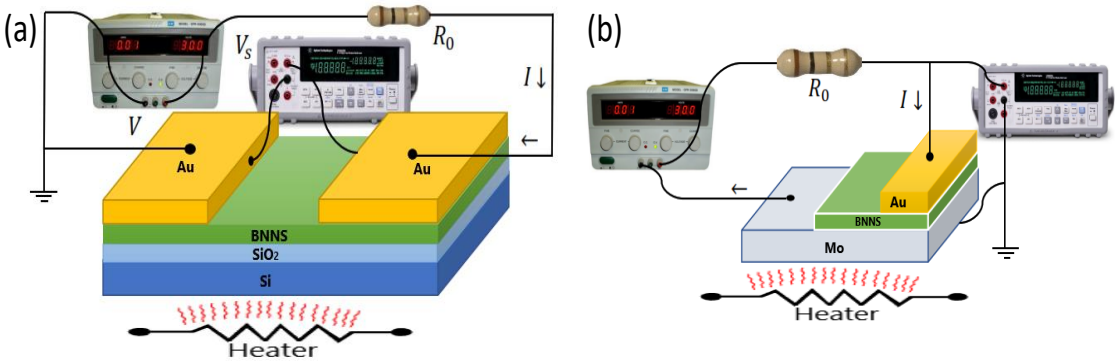

Figure 5. 3 Schematic representation of the I–V measurements setup in Au/BNNS/Au and Au/BNNS/Mo contacts. (a) and (b) illustrate the Schottky contacts deposited on SiO_2/Si and Mo substrates. Au and Mo are solid conductors while the BNNS film is a two-dimensional crystalline form of the h-BN.

5.4 Transport properties

Now, we focus on analyzing the electrical properties of BNNS films with two-dimensional features in Au/BNNS/Au and Au/BNNS/Mo Schottky contacts. Then, we will study the effect of temperature on the current voltage (I–V) characteristic curve.

BNNSs exhibit very promising electrical properties when a very small amount of current passes through them. Previous experiments have shown that C-doped BNNS could increase the adsorption energy of NO and NO_2 [45], thereby changing its electronic structure and band gap value. This change in settings makes it exhibit stable hysteresis characteristics, especially when analyzing under low voltage levels between terminals. Consequently, BNNS thin film shows a hysterical region close to the origin point when measured on scales from 0 to 3 V in steps of 0.01 V, both in forward and reverse bias voltages, as shown in Figures 5.4(a) and (b). When the temperature changes between 20 and 100 °C, a hysteresis symmetric structure in the range of ± 0.1 to ± 0.2 V can be seen, and high thermal stability is maintained. This makes it a promising candidate for a 2D material with the hysteresis characteristics of two back-to-back connected Schottky junctions. In addition, it is observed that the hysteresis at 100 °C is slightly higher than that at 20 °C, which may be due to the increase in electron tunneling oscillating near that interval and boron vacancies that act as trapping centers. These electrical changes can be seen in detail in the upper part of the I–V illustrations. Many factors will affect the hysteresis effect. Doping content and interface structure may play a dominant role in these phenomena. A high degree

of hysteresis stability over a wide range can be achieved in a heavily doped wide-bandgap material where charge trapping is justified and enhanced. This should be important for future memory devices or electronic systems.

A more in-depth study is essential if hysteresis is to be obtained over a wide range of voltage since until now the stability of the Schottky contact with hysteresis at low voltages has been demonstrated. One of the techniques to enhance the electrical properties of BNNS is to decrease the bandgap through doping; in this case, a small amount of carbon was added, which in turn created Boron vacancies, thus converting it into a material with n-type characteristics.

If the operating conditions of Au/BNNS/Au Schottky diodes are taken from 0 to ±20 V in steps of ±0.1 V, non-ohmic behavior is dominant, and the hysteresis of BNNS film is negligible at 25 and 100 °C, as shown in Figures 5.4(c) and (d). Previous studies have shown that charge trap states at the SiO_2/h-BN interface were not sufficiently changed in hysteresis because they were occupied by electron-hole pairs, which suggests the h-BN film is sufficiently thick and prevents electron tunneling, thus creating a clean and inert interface. Through carbon doping, h-BNNS layers show improved conductivity, generating a small amount of free charges on the SiO_2/BNNS interface by the action of a low voltage supply (0 to 3 V in steps of 0.01 V) through Au/BNNS/Au junctions. Conversely, if the voltage increases from 0 to 20 V in steps of 0.1 V, this effect is not appreciated. Therefore, the Schottky barrier potential acts as a high-speed current rectifier at the metal-semiconductor junction, where hysteresis is not appreciable due to its small interaction surface, thereby reducing charge traps in the junctions.

On the other hand, in Au/BNNS/Mo Schottky barrier diodes, hysteresis is dominated at small forward bias voltages taken from 0 to 3 V in steps of 0.01 V, forming various charge traps around 0.09 and 0.17 V, as shown in Figure 5.5(a).

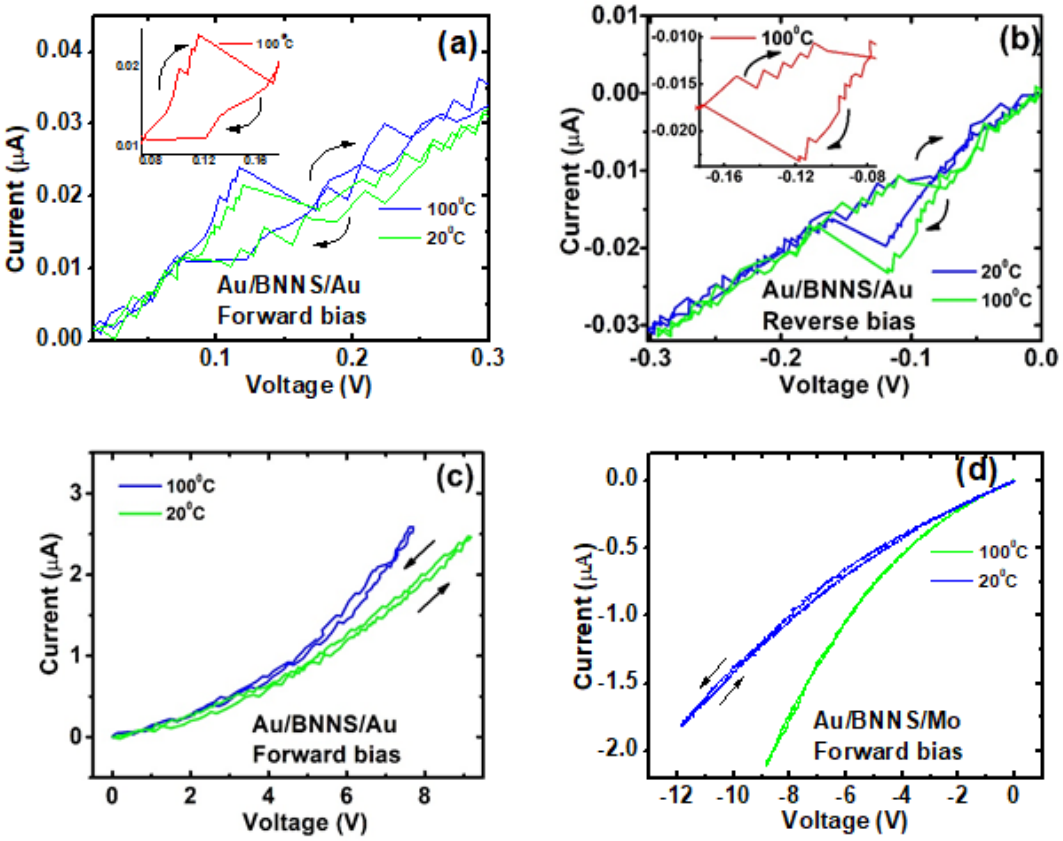

Figure 5. 4 Au/BNNS/Au Schottky contacts with and without hysteresis on Si/SiO_2 substrates taken in 0.01 V and 0.1 V steps at temperatures of 20 °C and 100 °C in the I–V curve. **(a)** At a low level of forward bias, **(b)** at a low level of reverse bias, **(c)** at a high level of forward bias, **(d)** at a high level of reverse bias.

The temperature change from 20 to 170 °C does not change its hysteresis characteristics thus ensuring the maximum stability in high-temperature environments. Instead, under the reverse bias voltage, the hysteresis becomes

unstable, and the change is not sufficiently visible, which may contradict the analyzed precondition, as shown in Figure 5.5(b). This effect may be due to the change of the Schottky barrier height by the junctions of two metals with different work functions and the semiconductor. In addition, the contact area between the junctions is not the same, so an asymmetric curve appears in the I–V curve. The obtained experimental data clearly indicated that the samples are very stable over a wide temperature range. Doping content and the interface structure may be a dominant factors in back-to-back contacts. Differences in symmetry and applied voltages due to the different structures of BNNS/Au or BNNS/Mo suggest that charge traps reduce its mobility at the metal/BNNS interface.

Au/BNNS/Mo Schottky contacts taken from 0 to ±20 V in steps of ±0.1 V have peculiar characteristics in the forward and reverse bias region with higher speeds at higher temperatures in the I–V curve, as shown in Figures 5.5(c) and (d). Increased tunnel current and thermal voltage affect the Schottky barrier heights, which depend on the work function of the metal and semiconductor [46, 47]. When characterizing the Au/BNNS/Mo junctions, we observed that the Au/BNNS contact gives faster recombination of the electrons and holes than that of the Molybdenum. These changes allow the behavior of the back-to-back Schottky contact to be asymmetric as discussed above. In addition, charge traps of the majority carriers (electrons) by sample impurities in the bandgap region are considerably reduced by the presence of a large electric field, without the need for so much thermal energy.

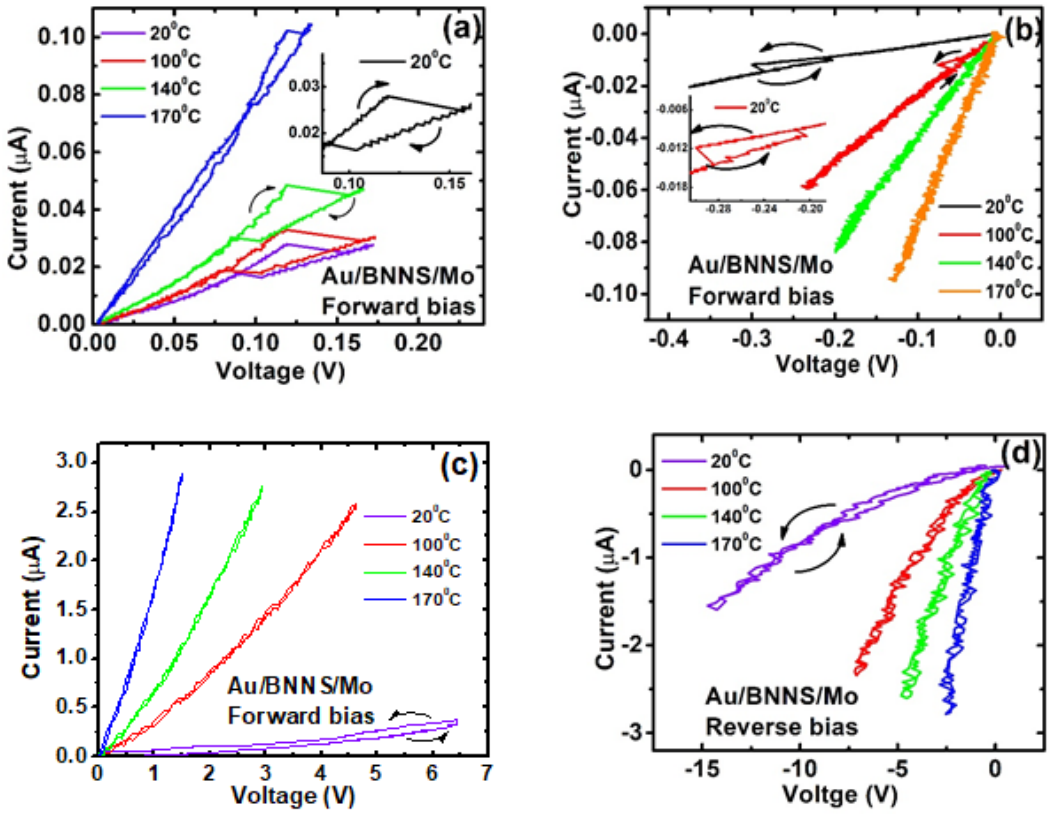

Figure 5. 5 Au/BNNS/Mo Schottky contacts **(a) – (b)** with and without hysteresis effect taken from 0 to ± 3 V in steps of 0.01 V in the I-V curve, **(c) – (d)** with and without hysteresis effect taken from 0 to ± 20 V in steps of 0.1 V.

As we have seen symmetric and asymmetric contacts, the electron tunneling mechanism and electron emission are universal. Because of the different methods that exist in the transfer of electrons; as for example, Poole-Frenkel emission, Schottky emission, Space-Charge-Limited-Conduction, trap-assisted tunneling, and hopping conduction are attributed to both tunneling and electron emission. However, these effects largely depend on the junction of the material and its characteristic electrical properties. In the case of two-dimensional

hexagonal boron nitride nanosheets, this is attributed to electron tunneling at the metal/semiconductor interface and electron emission caused by temperature changes.

The novelty of this material is that it can enhance the device's performance and data retention due to its functional properties, thermal-mechanical stability, and its relationship with resistive switching phenomena.

The current-voltage characteristic of a Schottky diode is described by the equation

$$I = I_s \left[exp\left(\frac{qV_D}{\eta kT}\right) - 1 \right], \tag{5.3}$$

where I_s is the saturation current ($I_s \approx 10^{-12}$ to 10^{-6} A) [48,49], η is the ideality factor (η typically varies from 1 to 2), k is the Boltzmann constant ($k = 1.38\text{x}10^{-23}$ $m^2kgs^{-2}K^{-1}$), T is the absolute temperature, and V_D is the bias voltage.

Equation (5.3) is a better approximation among experimental curves for voltages not including higher forward bias (positive voltage). If the ideality factor approaches unity, the current in the diode is not driven by the potential barrier height for voltages higher than the barrier, but by the series resistance that is always in the circuit.

$$I = I_s \left[exp\left(\frac{q(V - R_s I)}{\eta k_B T}\right) - 1 \right], \tag{5.4}$$

thus $V_D = V - R_s I$, where V is the applied voltage and R_s is the semiconductor resistance. I_s is given by

$$I_s = AA^* T^2 e^{-\frac{\Phi_B}{kT}}, \tag{5.5}$$

where A is the active Schottky diode area ($A_{Au/BNNS/Au} =$ 3x10^{-11} m^2, $A_{Au/BNNS/Mo} =$ 7.85x10^{-5} m^2), A^* is the Richardson constant (A^* = 3.12x10^5 Am^{-2}K^{-2}), and Φ_B is the barrier height. The barrier height is also given by

$$\Phi_B = k_B T ln\left[\frac{AA^*T^2}{I_s}\right]. \tag{5.6}$$

Just like there are two Schottky contacts connected back-to-back, equations (5.4) can be written as two different voltage drops on single diodes, one polarized in the forward and the other in the reverse direction. Since the charge flowing through them are the same, we may express the diode equations with ideality factors [50, 51].

$$I = I_{s1}\left[exp\left(\frac{qV_{D1}}{\eta kT}\right) - 1\right]\ Forward\,, \tag{5.7}$$

$$I = -I_{s2}\left[exp\left(-\frac{qV_{D2}}{\eta kT}\right) - 1\right]\ Reverse\,, \tag{5.8}$$

where V_{D1} and V_{D2} are the voltage drops on single diodes. The equations are then

$$V_{D1} = \frac{\eta kT}{q} ln\left(\frac{I}{I_{s1}} + 1\right), \tag{5.9}$$

$$V_{D2} = -\frac{\eta kT}{q} ln\left(-\frac{I}{I_{s2}} + 1\right), \tag{5.10}$$

and their sum is equal to the external voltage ($V_{D1} + V_{D2} = V$). By performing some mathematical techniques, we can express the current in the form of back-to-back Schottky diodes as

$$I = \frac{2\frac{I_{s1}}{A_1}\frac{I_{s2}}{A_2}\sinh\left(\frac{qV_D}{2\eta kT}\right)}{\frac{I_{s1}}{A_1}exp\left(-\frac{qV_D}{2\eta kT}\right)+\frac{I_{s2}}{A_2}exp\left(\frac{qV_D}{2\eta kT}\right)}\ , \tag{5.11}$$

where A_1 and A_2 are the contact areas of the single diodes.

In real asymmetric structures, the variation of barrier heights makes it unlikely that the ideality factors of the two contacts are the same. This type of contact cannot be described by simple analytical equations, and it is necessary to consider the series resistance, which allows better analysis of the experimental results. In this case, the current through the contacts is expressed for voltage drops on single diodes with their respective ideality factor.

$$V_1 = \frac{\eta_1 k_B T}{q} ln\left(\frac{I}{I_{s1}}+1\right), \tag{5.12}$$

$$V_2 = -\frac{\eta_2 k_B T}{q} ln\left(-\frac{I}{I_{s2}}+1\right). \tag{5.13}$$

The external voltage (V) between metal-semiconductor-metal is distributed into the voltage drops V_1 and V_2 on the series resistance

$$V = V_1 + V_2 + R_s I\ , \tag{5.14}$$

$$V = \frac{\eta_1 k_B T}{q} ln\left(\frac{I}{I_{s1}}+1\right) - \frac{\eta_2 k_B T}{q} ln\left(-\frac{I}{I_{s2}}+1\right) + R_s I\ . \tag{5.15}$$

Equation 5.15 is a general V-I expression for back-to-back Schottky diodes in devices containing an MSM, respectively.

The Schottky barrier plays a central role in lowering the metal work functions, whose values range from 4.6 (molybdenum) to 5.2 eV (gold). The barrier

heights of Au/BNNS/Au Schottky diodes range from 0.332 to 0.732 eV in the forward and from 0.326 to 0.723 eV in the reverse. These slight variations do not significantly modify the symmetry of the I–V curve shown in Figures 5.4(c) and (d). Instead, in Au/BNNS/Mo junctions, values range from 0.763 to 1.043 eV in the forward (BNNS/Mo) and from 0.570 to 0.976 eV in the reverse (BNNS/Au). In fact, results show that BNNS/Au junctions reduce Schottky barrier heights better than BNNS/Mo junctions, which also influence the asymmetry of the I–V curve presented in Figures 5.5(c) and (d). Also, when changing the environment conditions from 20 to 170 °C, the barrier heights increase, which may be to the current increase through the metal/semiconductor junction since more electrons have sufficient energy to surmount the higher barrier due to thermal voltage.

On the one hand, in the symmetrical structure, the leakage current decreases slightly with the increase in temperature, both in forward ($1.53x10^{-6}$ to $8.51x10^{-8}$ A) and reverse bias ($1.90x10^{-6}$ to $1.01x10^{-6}$ A). This abnormal behavior of the diode indicates that recombination of carriers is affected by thermal voltage as well as trap-assisted tunneling current. Instead, in the asymmetric structure is the opposite both forward ($1.57x10^{-7}$ to $6.38x10^{-6}$ A) and reverse bias ($1.13x10^{-6}$ to $5.03x10^{-6}$ A), which is typical of Schottky diodes when the absence of charge is higher in the junctions. This effect is also related to the contact area of the asymmetric junction ($3x10^{-11}$ m^2) is much larger than the symmetric contact ($7.85x10^{-5}$ m^2), which generates larger recombination of electron tunneling through the Schottky contact surface, thereby increasing the leakage current as of the temperature increases.

The parameter that allows specifying the metal-semiconductor junction is the ideality factor η. When Schottky diodes are dominated by ideal thermionic emission the ideality factor η has a range of 1. However, when other physical mechanisms are added to thermionic emissions, such as thermally assisted tunneling and field-enhanced tunneling, η becomes larger than 1. In the back-to-back Schottky diode, the calculation of the ideality factor is based on the mechanism of the voltage drop across the individual barriers. The values obtained in Au/BNNS/Au contacts are in the forward range from 2.50 to 1.22 and in the reverse range from 4.38 to 1.66. In this procedure, we observed that η decreases with increasing temperature from 20 to 100 °C. Likewise, in Au/BNNS/Mo contacts, η is in the range from 1.79 to 1.04 in the forward, and from 4.16 to 1.83 in the reverse, which is similar to the previous case, but this time the conditions were from 20 to 170 °C. This indicates that diffusion currents are increased due to the thermionic effect, and the thermal energy provided to the charge carriers is larger than the work function of the conductor material.

Since electrons pass through the BNNS film at a low energy level than the Schottky barrier height, the tunneling effect affects the hysteresis characteristics of the material. Solving the Schrodinger equation in one dimension allows us to understand these physical details through the transmission coefficient, which is proportional between the modules of the square wave function as

$$T = \frac{|\Psi_B|^2}{|\Psi_A|^2} = \left[1 + \frac{{U_0}^2 sinh^2(|k|d)}{4E(U_0 - E)}\right]^{-1}, \qquad (5.16)$$

$$T \sim \exp\left(-2\sqrt{\frac{2m(E-U_0)}{\hbar^2}}\,d\right), \tag{5.17}$$

where Ψ_A is the wave function in the conductor region, Ψ_B is the wave function in the semiconductor, U_0 is the barrier potential ($U_0 = \Phi_B$), d is the depletion zone width, E is the energy of the electron ($E < U_0$), m is the mass of the electron, and $k = \sqrt{\frac{2m(E-U_0)}{\hbar}}$. When the depletion zone is about 10 nm or less, it promotes electron tunneling, which is conducive to charge flow and reduces hysteresis. Since the thickness of BNNS is around 3-4 nm, the tunneling effect would affect the hysteresis characteristics, leading to a lowering of the energy barrier due to the interaction with the electric field in the metal-semiconductor interface.

5.5 Conclusions

Au/BNNS/Au Schottky contacts favor the reduction of the tunneling effects and carrier recombination, maintaining an almost constant flow of electrons through the BNNSs film. Under low bias voltage, it exhibits a stable symmetric hysteresis and improved adsorption energy by the concentration of a slight amount of carbon in the BNNS two-dimensional atomic layers.

On the other hand, Au/BNNS/Mo Schottky barrier exhibits stable hysteresis characteristics under low bias voltages in environments up to 170 °C. When electrons tunnel from the Mo-BNNS to the BNNS-Au interface, the hysteresis effect is reduced in the sequential I–V seeping. This suggests that in reverse bias there is little effect on the emission of the electron traps due to the action of a large electrical field at the junction, which is compatible with the Poole-Frenkel effect. When the charge switching speed increases rapidly with a slight increase in bias voltage and temperature, the hysteresis area becomes smaller and smaller, which makes it a rectifier with low energy loss.

It can be concluded that the hysteresis loops in Au/BNNS/Au and Au/BNNS/Mo Schottky diodes are directly affected by variable parameters of series resistance and barrier lowering. The mechanism of the charge traps could be attributed to the electrons directly tunneling on the interface, and the release of trapped electrons due to thermionic emission. This is convincing with observations made at the Schottky barrier when current- voltage (I–V) operating conditions change at the BNNS film.

5.6 References

[1] J. Jeevanandam, A. Barhoum, Y.S. Chan, A. Dufresne, M.K. Danquah, Review on nanoparticles and nanostructured materials: history, sources, toxicity and regulations, Beilstein Journal of Nanotechnology. 9 (2018) 1050–1074. https://doi.org/10.3762/bjnano.9.98.

[2] L.H. Li, J. Cervenka, K. Watanabe, T. Taniguchi, Y. Chen, Strong oxidation resistance of atomically thin boron nitride nanosheets, ACS Nano. 8 (2014) 1457–1462. https://doi.org/10.1021/NN500059S/SUPPL_FILE/NN500059S_SI_001.PDF.

[3] N. Berseneva, A. Gulans, A. v. Krasheninnikov, R.M. Nieminen, Electronic structure of boron nitride sheets doped with carbon from first-principles calculations, Phys Rev B. 87 (2013) 035404. https://doi.org/10.1103/PhysRevB.87.035404.

[4] H. Park, A. Wadehra, J.W. Wilkins, A.H. Castro Neto, Magnetic states and optical properties of single-layer carbon-doped hexagonal boron nitride, Appl Phys Lett. 100 (2012). https://doi.org/10.1063/1.4730392.

[5] J. Zhao, Z. Chen, Carbon-Doped Boron Nitride Nanosheet: An Efficient Metal-Free Electrocatalyst for the Oxygen Reduction Reaction, Journal of Physical Chemistry C. 119 (2015) 26348–26354. https://doi.org/10.1021/ACS.JPCC.5B09037/ASSET/IMAGES/LARGE/JP-2015-090378_0007.JPEG.

[6] C. Zhao, Z. Xu, H. Wang, J. Wei, W. Wang, X. Bai, E. Wang, Carbon-Doped Boron Nitride Nanosheets with Ferromagnetism above Room Temperature, Adv Funct Mater. 24 (2014) 5985–5992. https://doi.org/10.1002/ADFM.201401149.

[7] M.D. Esrafili, N. Saeidi, Carbon-doped boron nitride nanosheet as a promising catalyst for N2O reduction by CO or SO2 molecule: A comparative DFT study, Appl Surf Sci. 444 (2018) 584–589. https://doi.org/10.1016/J.APSUSC.2018.03.107.

[8] C. Huang, C. Chen, M. Zhang, L. Lin, X. Ye, S. Lin, M. Antonietti, X. Wang, Carbon-doped BN nanosheets for metal-free photoredox catalysis, Nat Commun. 6 (2015) 1–7. https://doi.org/10.1038/ncomms8698.

[9] V. Guerra, C. Wan, T. McNally, Thermal conductivity of 2D nano-structured boron nitride (BN) and its composites with polymers, Prog Mater Sci. 100 (2019) 170–186. https://doi.org/10.1016/j.pmatsci.2018.10.002.

[10] X. Wang, A. Pakdel, C. Zhi, K. Watanabe, T. Sekiguchi, D. Golberg, Y. Bando, High-yield boron nitride nanosheets from “chemical blowing”: Towards practical applications in polymer composites, Journal of Physics Condensed Matter. 24 (2012). https://doi.org/10.1088/0953-8984/24/31/314205.

[11] Y.J. Min, K.H. Kang, D.E. Kim, Development of polyimide films reinforced with boron nitride and boron nitride nanosheets for transparent flexible

device applications, Nano Research 2017 11:5. 11 (2018) 2366–2378. https://doi.org/10.1007/S12274-017-1856-0.

[12] C. Teng, L. Su, J. Chen, J. Wang, Flexible, thermally conductive layered composite films from massively exfoliated boron nitride nanosheets, Compos Part A Appl Sci Manuf. 124 (2019) 105498. https://doi.org/10.1016/J.COMPOSITESA.2019.105498.

[13] X. Zou, C.-W. Huang, L. Wang, L.-J. Yin, W. Li, J. Wang, B. Wu, Y. Liu, Q. Yao, C. Jiang, W.-W. Wu, L. He, S. Chen, J.C. Ho, L. Liao, X. Zou, W. Li, J. Wang, C. Jiang, L. Liao, C.-W. Huang, -W W Wu, L. Wang, B. Wu, Y. Liu, L.-J. Yin, L. He, Q. Yao, S. Chen, C. Ho, Dielectric Engineering of a Boron Nitride/Hafnium Oxide Heterostructure for High-Performance 2D Field Effect Transistors, Advanced Materials. 28 (2016) 2062–2069. https://doi.org/10.1002/ADMA.201505205.

[14] K. Zhang, Y. Feng, F. Wang, Z. Yang, J. Wang, Two dimensional hexagonal boron nitride (2D-hBN): synthesis, properties and applications, J Mater Chem C Mater. 5 (2017) 11992–12022. https://doi.org/10.1039/C7TC04300G.

[15] L. Wirtz, A. Marini, A. Rubio, Optical absorption of hexagonal Boron nitride and BN nanotubes, in: AIP Conf Proc, 2005: pp. 391–395. https://doi.org/10.1063/1.2103894.

[16] R. Basu, L.J. Atwood, Two-dimensional hexagonal boron nitride nanosheet as the planar-alignment agent in a liquid crystal-based electro-optic device, Opt Express. 27 (2019) 282. https://doi.org/10.1364/oe.27.000282.

[17] A. Slaoui, E. Fogarassy, C. Fuchs, P. Siffert, Properties of silicon dioxide films prepared by pulsed-laser ablation, J Appl Phys. 71 (1998) 590. https://doi.org/10.1063/1.350411.

[18] G.D.J. Smit, S. Rogge, T.M. Klapwijk, Scaling of nano-Schottky-diodes, Appl Phys Lett. 81 (2002) 3852–3854. https://doi.org/10.1063/1.1521251.

[19] M. Rezeq, K. Eledlebi, M. Ismail, R.K. Dey, B. Cui, Theoretical and experimental investigations of nano-Schottky contacts, J Appl Phys. 120 (2016) 044302. https://doi.org/10.1063/1.4959090.

[20] H. Zhao, Z. Dong, H. Tian, D. DiMarzi, M.G. Han, L. Zhang, X. Yan, F. Liu, L. Shen, S.J. Han, S. Cronin, W. Wu, J. Tice, J. Guo, H. Wang, Atomically Thin Femtojoule Memristive Device, Advanced Materials. 29 (2017). https://doi.org/10.1002/adma.201703232.

[21] G. Choi, H.H. Yoon, S. Jung, Y. Jeon, J.Y. Lee, W. Bahng, K. Park, Schottky barrier modulation of metal/4H-SiC junction with thin interface spacer driven by surface polarization charge on 4H-SiC substrate, Appl Phys Lett. 107 (2015). https://doi.org/10.1063/1.4938070.

[22] H. Yuan, Q.W. Song, C. Han, X.Y. Tang, X.N. He, Y.M. Zhang, Y.M. Zhang, Hysteresis effect in current-voltage characteristics of Ni/n-type 4H-SiC

Schottky structure, Chinese Physics B. 28 (2019) 117303–117303. https://doi.org/10.1088/1674-1056/ab470f.

[23] X. Wu, R. Ge, P.A. Chen, H. Chou, Z. Zhang, Y. Zhang, S. Banerjee, M.H. Chiang, J.C. Lee, D. Akinwande, Thinnest Nonvolatile Memory Based on Monolayer h-BN, Advanced Materials. 31 (2019). https://doi.org/10.1002/adma.201806790.

[24] I. Sanchez Esqueda, H. Zhao, H. Wang, Efficient learning and crossbar operations with atomically-thin 2-D material compound synapses, J Appl Phys. 124 (2018). https://doi.org/10.1063/1.5042468.

[25] Y.S. Zhi, P.G. Li, P.C. Wang, D.Y. Guo, Y.H. An, Z.P. Wu, X.L. Chu, J.Q. Shen, W.H. Tang, C.R. Li, Reversible transition between bipolar and unipolar resistive switching in Cu2O/Ga2O3 binary oxide stacked layer, AIP Adv. 6 (2016). https://doi.org/10.1063/1.4941061.

[26] D.S. Jeong, C.S. Hwang, Tunneling-assisted Poole-Frenkel conduction mechanism in Hf O2 thin films, J Appl Phys. 98 (2005). https://doi.org/10.1063/1.2135895.

[27] J.R. Yeargan, H.L. Taylor, The Poole-Frenkel effect with compensation present, J Appl Phys. 39 (1968) 5600–5604. https://doi.org/10.1063/1.1656022.

[28] M.J. Hanna, H. Zhao, J.C. Lee, Poole Frenkel current and Schottky emission in SiN gate dielectric in AlGaN/GaN metal insulator semiconductor

heterostructure field effect transistors, Appl Phys Lett. 101 (2012). https://doi.org/10.1063/1.4758995.

[29] C. Xiong, Z. Lu, S. Yin, H. Mou, X. Zhang, Magnetic field controlled hybrid semiconductor and resistive switching device for non-volatile memory applications, AIP Adv. 9 (2019). https://doi.org/10.1063/1.5063734.

[30] T. Li, G. Du, B. Zhang, Z. Zeng, Scaling behavior of hysteresis in multilayer MoS2 field effect transistors, Appl Phys Lett. 105 (2014) 093107. https://doi.org/10.1063/1.4894865.

[31] N. Kaushik, D.M.A. Mackenzie, K. Thakar, N. Goyal, B. Mukherjee, P. Boggild, D.H. Petersen, S. Lodha, Reversible hysteresis inversion in MoS2 field effect transistors, NPJ 2D Mater Appl. 1 (2017). https://doi.org/10.1038/s41699-017-0038-y.

[32] Design and installation of a CO2-pulsed laser plasma deposition system for the growth of mass product nanostructures - Google Search, (n.d.). https://www.google.com/search?rlz=1C1CHBD_esPE882PE882&ei=4CAjXuUowq-CB_TEt6AD&q=Design+and+installation+of+a+CO2-pulsed+laser+plasma+deposition+system+for+the+growth+of+mass+product+nanostructures&oq=Design+and+installation+of+a+CO2-pulsed+laser+plasma+deposition+system+for+the+growth+of+mass+product+nanostructures&gs_l=psy-ab.3..0l3j0i22i30l2.52472.52472..53956...0.0..0.147.267.0j2.....1....2j1..gw

s-wiz.....0i30.-RU-WaXF-Qw&ved=0ahUKEwjlmIijuI3nAhXCl-AKHXTiDTQQ4dUDCAs&uact=5 (accessed January 17, 2020).

[33] Q. Cai, D. Scullion, A. Falin, K. Watanabe, T. Taniguchi, Y. Chen, E.J.G. Santos, L.H. Li, Raman signature and phonon dispersion of atomically thin boron nitride, Nanoscale. 9 (2017) 3059–3067. https://doi.org/10.1039/c6nr09312d.

[34] S. Wan, Y. Yu, J. Pu, Z. Lu, Facile fabrication of boron nitride nanosheets–amorphous carbon hybrid film for optoelectronic applications, RSC Adv. 5 (2015) 19236–19240. https://doi.org/10.1039/C4RA13268H.

[35] P. Ahmad, M.U. Khandaker, N. Muhammad, G. Khan, F. Rehman, A.S. Khan, Z. Ullah, A. Khan, H. Ali, S.M. Ahmed, M.A. Rauf Khan, J. Iqbal, A.A. Khan, M.I. Irshad, Fabrication of hexagonal boron nitride quantum dots via a facile bottom-up technique, Ceram Int. 45 (2019) 22765–22768. https://doi.org/10.1016/j.ceramint.2019.07.316.

[36] A. Falin, Q. Cai, E.J.G. Santos, D. Scullion, D. Qian, R. Zhang, Z. Yang, S. Huang, K. Watanabe, T. Taniguchi, M.R. Barnett, Y. Chen, R.S. Ruoff, L.H. Li, Mechanical properties of atomically thin boron nitride and the role of interlayer interactions, Nat Commun. 8 (2017) 1–9. https://doi.org/10.1038/ncomms15815.

[37] L.H. Li, Y. Chen, Atomically Thin Boron Nitride: Unique Properties and Applications, Adv Funct Mater. 26 (2016) 2594–2608. https://doi.org/10.1002/adfm.201504606.

[38] M. Chubarov, H. Högberg, A. Henry, H. Pedersen, Review Article: Challenge in determining the crystal structure of epitaxial 0001 oriented sp2-BN films, Journal of Vacuum Science & Technology A: Vacuum, Surfaces, and Films. 36 (2018) 030801. https://doi.org/10.1116/1.5024314.

[39] V. Guerra, C. Wan, V. Degirmenci, J. Sloan, D. Presvytis, T. McNally, 2D boron nitride nanosheets (BNNS) prepared by high-pressure homogenisation: Structure and morphology, Nanoscale. 10 (2018) 19469–19477. https://doi.org/10.1039/c8nr06429f.

[40] S. Maghsoudy-Louyeh, M. Kropf, B.R. Tittmann, Review of Progress in Atomic Force Microscopy, Open Neuroimag J. 12 (2019) 86–104. https://doi.org/10.2174/1874440001812010086.

[41] Y. Li, V. Garnier, P. Steyer, C. Journet, B. Bérangè Re Toury, Millimeter-Scale Hexagonal Boron Nitride Single Crystals for Nanosheet Generation, (2020). https://doi.org/10.1021/acsanm.9b02315.

[42] M.D. Esrafili, F. Arjomandi Rad, Carbon-doped boron nitride nanosheets as highly sensitive materials for detection of toxic NO and NO2 gases: A DFT study, Vacuum. 166 (2019) 127–134. https://doi.org/10.1016/j.vacuum.2019.04.065.

[43] P.X. Feng, M. Sajjad, Few-atomic-layer boron nitride sheets syntheses and applications for semiconductor diodes, Mater Lett. 89 (2012) 206–208. https://doi.org/10.1016/j.matlet.2012.08.053.

[44] M. Sajjad, M. Ahmadi, M.J.F. Guinel, Y. Lin, P. Feng, Large scale synthesis of single-crystal and polycrystalline boron nitride nanosheets, J Mater Sci. 48 (2013) 2543–2549. https://doi.org/10.1007/s10853-012-7044-4.

[45] I. Dökme, The analysis of I–V characteristics of Schottky diodes by thermionic emission with a Gaussian distribution of barrier height, Microelectronics Reliability. 51 (2011) 360–364. https://doi.org/10.1016/J.MICROREL.2010.08.017.

[46] A. Latreche, Combined thermionic emission and tunneling mechanisms for the analysis of the leakage current for Ga2O3 Schottky barrier diodes, SN Appl Sci. 1 (2019). https://doi.org/10.1007/s42452-019-0192-2.

[47] Z. Yuan, A. Nainani, Y. Sun, J.-Y.J. Lin, P. Pianetta, K.C. Saraswat, Schottky barrier height reduction for metal/n-GaSb contact by inserting TiO2 interfacial layer with low tunneling resistance, Appl Phys Lett. 98 (2011) 172106. https://doi.org/10.1063/1.3584862.

[48] V.M. Sklyarchuk, V.A. Gnatyuk, V.G. Pylypko, T. Aoki, Schottky Diode Detectors with Low Leakage Current at High Operating Voltage, in: Lecture Notes in Networks and Systems, Springer, 2020: pp. 159–167. https://doi.org/10.1007/978-3-030-36841-8_16.

[49] K.R. Peta, M.D. Kim, Leakage current transport mechanism under reverse bias in Au/Ni/GaN Schottky barrier diode, Superlattices Microstruct. 113 (2018) 678–683. https://doi.org/10.1016/j.spmi.2017.11.056.

[50] J. Osvald, Back-to-back connected asymmetric Schottky diodes with series resistance as a single diode, Physica Status Solidi (a). 212 (2015) 2754–2758. https://doi.org/10.1002/PSSA.201532374.

[51] R. Nouchi, Extraction of the Schottky parameters in metal-semiconductor-metal diodes from a single current-voltage measurement, J Appl Phys. 116 (2014) 184505. https://doi.org/10.1063/1.4901467.

Chapter 6

Summary and Future Work

The research performed in this thesis has contributed significantly to recent advances and important new developments in 2D materials “beyond graphene”, providing details on the dynamics of synthesis, atomic scale nanosheet characterization, crystal structure evolution between adjacent layers, and their applications in photodetectors and non-volatile memory. We also review new challenges in the 2D family, especially in TMDs and BNNS, as they cover a wide range of electrical, optical, thermal, mechanical, and chemical properties, respectively. The important advancements are briefly described in this section.

In chapter 2, we used WS_2 nanopowder at a concentration of 1 mg/ml in a mixture of ethanol 90%, methanol 5%, and isopropanol 5% to produce 2D WS_2 nanosheets. Obtaining micron-layered materials for few-layered nanosheets remains a challenge even with the most sophisticated techniques. However, mechanical exfoliation is the most straightforward and universal method for 2D materials due to the weak Van der Waals' force between the adjacent layers. We also demonstrated that it was possible to obtain high-quality nanosheets for thin films on SiO_2/Si substrates using the spin coating method. In comparison to different fabrication techniques, the apparatus is widely used by the microelectronics industry, research, and technology sectors due to its weight, size, space, simplicity, easy transportation, and low cost, which makes them the most widely used in several scientific applications. Instead, CO_2-PLD proved to be one

of the most attractive methods for synthesizing BNNS thin films on SiO_2 and Mo substrates with a hBN sputtering target of 99.9% pure, preventing post-deposition contamination and changes to its high purity. Due to the CH_4 environment in the vacuum chamber, BNNS thin films with carbon atom concentrations were achieved when the deposition was kept at 300 °C for 20 min. SEM analysis revealed that the entire surface of the substrate was covered with disk shape BN nanostructures, which indicated a relatively short time to grow large-scale materials. Finally, to fabricate lateral and vertical structures, gold atoms were deposited by sputtering technique to obtain prototypes of the Au/WS_2/Au, Au/BNNS/Au, and Au/BNNS/Mo shapes, designed to measure optical responses, and the current-voltage effects.

In chapter 3, the main characterization techniques were briefly described, outlining their theoretical working principles and their relation to the studies carried out in this thesis. In this sense, the SEM analysis mechanism can reproduce a variety of two-dimensional images, scanning the surface of a sample, and revealing information about the surface topography, orientation, and crystalline structure. But EDS or EDAX is an X-ray technique used to identify the chemical compositions of materials. Instead, Raman spectroscopy is based on the inelastic scattering of incident light through the excitation of vibrational modes of solids or molecules and provides detailed information about phase, chemical structure, crystallinity, and molecular interactions. While, X-ray diffraction (XRD) allows for determining the positions of the atoms, chemical bonds, crystallographic disorder, and molecular structure of a crystal when an incident X-ray beam is diffracted into many specific directions. The scattering of the atoms is elastic, and the scattered

beams maintain the same wavelength as the incoming beams. Finally, UV/Vis measures light absorbance based on frequencies or wavelengths in the ultraviolet and visible regions. This process depends on the number of excited electrons in the ground state, as well as on the concentration of molecules in the sample. The absorbance (A) versus wavelength (λ) produces the spectrum, which is helpful for identifying an unknown compound.

In chapter 4, we studied 2D WS_2 nanosheets for self-powered photodetectors on Au/WS_2/Au junctions under the visible spectrum. Our device presented an excellent photoresponse to the mere action of light without the addition of an external power supply. This behavior was related to structural defects and strongly influenced their optical properties. For example, If the WS_2 sample is pure, the ratio of S and W must be 2 to 1, which is difficult under ambient conditions and even in vacuum environments due to the interstitial defects of the lattice in the film growth process. In our bulk material (nanopowder), energy-dispersive X-ray analysis showed an S/W ratio of 1.70 while exfoliated nanosheets were around 1.2 to 1.34, which indicated certain deficiencies in the S atoms. These changes induced localized states within the bandgap of pristine WS_2, resulting in a higher conductivity in photoelectric conversion. In addition, S vacancies were substituted by oxygen atoms so as not to create defect states in space or an optically accessible subgap state. On the other hand, the UV–visible absorption spectra of the WS_2 nanosheets exhibited a prominent peak at 634 nm and a small peak at 528 nm corresponding to the characteristic excitonic A band and indirect B excitonic transition. The first peak corresponds to an optical bandgap of 1.95 eV,

higher than the bulk sample value of about 1.35 eV. An increase in bandgap is a clear indication of quantum confinement among the stacked few layered. These changes have given rise to a self-powered photodetector, with the ability to detect light across the entire visible spectrum, thus revealing a strong photoresponse at 670 nm. The responsivity of the device reached 0.12 mA/W at 5.2 mW/cm^2 with a bias of 0 V., while at 2.0 V was 12.74 mA/W and detectivity of 1.2 × 10^{10} cm Hz$^{1/2}$ W^{-1} at 4.1 mW/cm^2.

In future research, we believe that 2D WS_2 nanosheets will have a wide range of applications due to their semi-conducting properties, large absorption coefficient, sensitivity to inter-layer interactions, and tunable bandgaps ranging from 1.2 to 2.05 eV according to the layer structure. Z. Huang et al. [1] reported a novel flexible self-powered PEC-type photodetector based on 2D tungsten sulfide (WS_2)-graphene heterojunction, fabricated on indium-tin-oxide (ITO) substrate. S. C. Zhao [2] fabricated a photodetector based on 2D-WS_2/organic semiconductor materials, where the application of Poly-TPD/PCBM organic blend film enhanced light absorption. T. D. Anthopoulos et al. [3] also showed that the hole transport layers comprising WS_2 exhibited higher uniformity on indium tin oxide than those of MoS_2, and consistently yield solar cells. Recently, we discovered that our material can also measure UV light in the range of 200 to 370 nanometers. These are some of the many applications being realized in the field of photodetectors, and more are likely to be discovered as the properties of the material are explored. However, for future work it is proposed to fabricate an asymmetric lateral junction photodetector to improve the response time to illumination, since in a symmetric

M-S-M device, the Schottky barrier heights (hole and electron) are restricted by the bandgap of the semiconductor [4]. Thus, photocurrent direction depends on the concentration of carriers in the metal-semiconductor junction, which sometimes generates hole current and sometimes electron current due to the low Schottky height. The rationality of this project will be based on the fact the device will be made of different metal elements with optimal Schottky barrier heights at the M-S and S-M interfaces, which will allow better optimization of each barrier and will reduce charge buildup at the heterointerface. This will result in a low signal-to-noise ratio, reduce leakage current, facilitate electron transfer, provide abundant free electrons, and improve sensing capabilities.

In Chapter 5, we investigated carbon-doped BNNS on SiO_2/Si and Mo substrates by the CO_2-PLD technique. The studies were performed in the form of back-to-back Schottky diodes on Au/BNNS/Au and Au/BNNS/Mo junctions. Our device presented a stable hysteresis over a wide range of temperatures, which makes them a promising candidate for materials based on non-volatile memory devices. BNNS bandwidth was in the range of 4–6 eV, and by doping with enough carbon (C), the bandgap was minimized, such that the material exhibited the electrical properties of a semiconductor. The carbon concentration also created a narrow depletion region that enabled electrons to move above their thermal equilibrium value. Due to the large amount of carriers generated in the depletion region, not all valence electrons become free electrons, some are still trapped by impurities in the sample, so these are also related to the hysteresis effect. The carbon addition also created boron vacancies, thus becoming a partially ionic

material with n-type electrical properties. In addition, the band-gap reduction of BNNS lead to measurements of current-voltage (I–V) curves that showed symmetrical and non-symmetrical characteristics at low and high bias voltages.

BNNS thin film exhibited hysterical regions close to the origin (± 0.1 to ± 0.2 V) when measured at forward and reverse bias voltages on scales from 0 a 3 V in steps of 0.01 V. This effect was observed between 20 and 170 °C, which indicated high thermal stability, while non-ohmic behavior was dominant when the operating conditions were from 0 to ±20 V in steps of ±0.1 V, and the hysteresis of BNNS film was negligible. However, we observed that the leakage current was higher for symmetric lateral contacts than for asymmetric vertical contacts. This indicated that characteristics of the contacts, such as the Schottky barrier heights are very important parameters that determine the electrical behavior of both ohmic and rectifying contacts to avoid further leakage current due to the low Schottky height.

Our contribution to this topic may lead to practical application in the future. This work provides an avenue for understanding the interaction of two-dimensional nanomaterials in applications of non-volatile memory devices and highly stable back-to-back Schottky diodes. E. Wang et al. [5] observed the disappearance of the ferromagnetic response upon removal of the carbon from the BN lattice, suggesting that the observed magnetism originated from doping. These changes in their electrical properties could be used to extract the uranium by the photocatalytic reduction technique [6]. We extend the application of carbon-doped BNNSs as a new alternative for high-stability photodetectors from UV to visible light in lateral and vertical asymmetric contact. In a study conducted by M. Sajjad

[7], BNNS photodetector was shown to be highly sensitive to deep UV light sources but did not show any results in the visible spectrum (400–700 nm), which would be a new opportunity to test the prototype. Due to their variable band energy, C-doped BNNS could be a highly sensitive material for the detection of toxic gases for both reducing and oxidizing elements. F. A. Rad et al. [8] showed that C-doped BNNS enhanced the adsorption energy of NO and NO_2 and was able to significantly alter the electronic structure of nanosheets, which can be evidenced by the variation of the band-gap value. In addition, our recent discoveries reported that BNNSs decorated with silver nanoparticles (AgNPs) could be on their potential application for high-performance photodetectors, from the UV (200 to 370 nm) to the visible spectra. Therefore, incorporating AgNPs on BNNSs provided a molecular platform for developing new 2D BNNS-based hybrid nanomaterials.

6.1 References

[1] X. Ren, B. Wang, Z. Huang, H. Qiao, C. Duan, Y. Zhou, J. Zhong, Z. Wang, X. Qi, Flexible self-powered photoelectrochemical-type photodetector based on 2D WS2-graphene heterojunction, FlatChem. 25 (2021) 100215. https://doi.org/10.1016/J.FLATC.2020.100215.

[2] F. Huang, J. Li, Z. Xu, Y. Liu, R. Luo, S.W. Zhang, P. Nie, Y. Lv, S. Zhao, W. Su, W. Di Li, S. Zhao, G. Wei, H.C. Kuo, F. Kang, A Bilayer 2D-WS2/Organic-Based Heterojunction for High-Performance Photodetectors, Nanomaterials (Basel). 9 (2019). https://doi.org/10.3390/NANO9091312.

[3] Y. Lin, B. Adilbekova, Y. Firdaus, E. Yengel, H. Faber, M. Sajjad, X. Zheng, E. Yarali, A. Seitkhan, O.M. Bakr, A. El-Labban, U. Schwingenschlögl, V. Tung, I. McCulloch, F. Laquai, T.D. Anthopoulos, 17% Efficient Organic Solar Cells Based on Liquid Exfoliated WS2 as a Replacement for PEDOT:PSS, Advanced Materials. 31 (2019) 1902965. https://doi.org/10.1002/ADMA.201902965.

[4] D.Z. Chi, R.T.P. Lee, S.J. Chua, S.J. Lee, S. Ashok, D.L. Kwong, Current–voltage characteristics of Schottky barriers with barrier heights larger than the semiconductor band gap: The case of NiGe/n-(001)Ge contact, J Appl Phys. 97 (2005) 113706. https://doi.org/10.1063/1.1923162.

[5] C. Zhao, Z. Xu, H. Wang, J. Wei, W. Wang, X. Bai, E. Wang, Carbon-Doped Boron Nitride Nanosheets with Ferromagnetism above Room Temperature,

Adv Funct Mater. 24 (2014) 5985–5992. https://doi.org/10.1002/ADFM.201401149.

[6] Y. Wang, G. Chen, H. Weng, L. Wang, J. Chen, S. Cheng, P. Zhang, M. Wang, X. Ge, H. Chen, W. Huang, M. Lin, Carbon-doped boron nitride nanosheets with adjustable band structure for efficient photocatalytic U(VI) reduction under visible light, Chemical Engineering Journal. 410 (2021) 128280. https://doi.org/10.1016/J.CEJ.2020.128280.

[7] Synthesis and Functionalization of Atomic Layer Boron Nitride Nanosheets for Advanced Material Applications, (n.d.). https://apps.dtic.mil/sti/citations/ADA616649 (accessed March 31, 2023).

[8] M.D. Esrafili, F. Arjomandi Rad, Carbon-doped boron nitride nanosheets as highly sensitive materials for detection of toxic NO and NO2 gases: A DFT study, Vacuum. 166 (2019) 127–134. https://doi.org/10.1016/J.VACUUM.2019.04.065.

List of Publications

1. **Wilber Ortiz**, Carlos Malca, Danilo Barrionuevo, Ali Aldalbahi, Elluz Pacheco, Nischal Oli, Peter Feng. Two-dimensional tungsten disulfide nanosheets and their application in self-powered photodetectors with ultra-high sensitivity and stability. *Vacuum 201, 111092 (2022).*

2. **Wilber Ortiz**, Nereida J Ramirez, Danilo Barrionuevo, Mohan K Bhattarai, and Peter Feng. Characterization of 2D boron nitride nanosheets with hysteresis effect in the Schottky junctions. *Nano Express 2, 010020 (2021).*